

MEASUREMENTS OF STANDARD MODEL HEAVY PARTICLE  
PRODUCTION IN ASSOCIATION WITH JETS USING PROTON-PROTON  
COLLISION DATA AT 8 AND 13 TEV WITH THE CMS EXPERIMENT AT THE  
LHC

A THESIS SUBMITTED TO  
THE GRADUATE SCHOOL OF NATURAL AND APPLIED SCIENCES  
OF  
MIDDLE EAST TECHNICAL UNIVERSITY

BUĞRA BİLİN

IN PARTIAL FULFILLMENT OF THE REQUIREMENTS  
FOR  
THE DEGREE OF DOCTOR OF PHILOSOPHY  
IN  
PHYSICS

JUNE 2017



Approval of the thesis:

**MEASUREMENTS OF STANDARD MODEL HEAVY PARTICLE  
PRODUCTION IN ASSOCIATION WITH JETS USING PROTON-PROTON  
COLLISION DATA AT 8 AND 13 TEV WITH THE CMS EXPERIMENT AT THE  
LHC**

submitted by **BUĞRA BİLİN** in partial fulfillment of the requirements for the degree  
of **Doctor of Philosophy in Physics Department, Middle East Technical Univer-**  
**sity** by,

Prof. Dr. Gülbin Dural Ünver

Dean, Graduate School of **Natural and Applied Sciences**

Prof. Dr. Altuğ Özpineci

Head of Department, **Physics**

Prof. Dr. Mehmet T. Zeyrek

Supervisor, **Physics Dept., METU**

**Examining Committee Members:**

Prof. Dr. Laurent Favart

Physics Dept., Université Libre de Bruxelles, Belgium

Prof. Dr. Mehmet T. Zeyrek

Physics Dept., METU

Prof. Dr. Altuğ Özpineci

Physics Dept., METU

Assoc. Prof. Dr. İsmail Turan

Physics Dept., METU

Prof. Dr. Müge Boz Evinay

Physics Engineering Dept., Hacettepe University

**Date:**

**I hereby declare that all information in this document has been obtained and presented in accordance with academic rules and ethical conduct. I also declare that, as required by these rules and conduct, I have fully cited and referenced all material and results that are not original to this work.**

Name, Last Name: BUĞRA BİLİN

Signature :



# ABSTRACT

## **MEASUREMENTS OF STANDARD MODEL HEAVY PARTICLE PRODUCTION IN ASSOCIATION WITH JETS USING PROTON-PROTON COLLISION DATA AT 8 AND 13 TEV WITH THE CMS EXPERIMENT AT THE LHC**

Bilin, Buğra

Ph.D., Department of Physics

Supervisor : Prof. Dr. Mehmet T. Zeyrek

June 2017, 150 pages

Standard Model (SM) of particle physics is the theory describing the main building blocks of matter and their interactions. In this thesis, two different measurements are carried out adding confidence to SM using proton proton collision data collected by the CMS experiment at the LHC .

Within the first study, multi-dimensional differential cross section measurements are carried out with respect to several kinematic variables of Z bosons and jets, where the Z bosons are reconstructed from opposite sign lepton (electron or muon) pairs. This measurement using 8 TeV data is the most precise Z + jet cross section measurement among other hadron collision measurements up to now. Theoretical calculations using state-of-the-art techniques are compared with the CMS measurements obtained in this measurement, and therefore provided a stringent test of those calculations. It is proven here that calculations involving higher orders in QCD describe the CMS results better.

Within the second study, measurement of Underlying Event (UE) activity accompanying top quark pair events is carried out using 13 TeV data. UE here corresponds to other parton collisions and remnants of protons accompanying the collision of physical interest. Since UE includes non-perturbative QCD effects, it can not be exactly calculated, hence it is included parametrically into Monte-Carlo simulations. These parameters are "tuned" using existing experimental results. The validity of these tunes is proven in the highest known mass scale of particle physics, namely the top scale, in this study.

Keywords: LHC, CMS, Standard Model, Z boson, jets, top quark, Underlying Event

# ÖZ

## **LHC CMS DENEYİNDE 8 VE 13 TEV PROTON-PROTON ÇARPIŞMA VERİSİ KULLANILARAK JETLERLE BİRLİKTE STANDART MODEL AĞIR PARÇACIK ÜRETİMİ ÖLÇÜMLERİ**

Bilin, Buğra

Doktora, Fizik Bölümü

Tez Yöneticisi : Prof. Dr. Mehmet T. Zeyrek

Haziran 2017 , 150 sayfa

Parçacık Fiziğinde Standart Model (SM), maddenin temel yapı taşlarını ve etkileşimlerini açıklayan teoridir. Bu tez kapsamında, LHC’de CMS deneyi tarafından toplanan proton proton çarpışma verisi kullanılarak iki farklı SM ölçümü gerçekleştirilmiştir.

İlk ölçüm kapsamında, zıt yüklü lepton çiftlerinden (elektron veya müon) geri oluşturulan Z bozonu ve jet kinematik değişkenlerine bağlı, çoklu-değişkenli tesir kesiti ölçümleri gerçekleştirilmiştir. 8 TeV’lik veri kullanılarak gerçekleştirilen Z+jet ölçümleri, bugüne kadar hadron çarpışma verisi kullanılarak yapılan ölçümlere nazaran hassaslık seviyesi en yüksek ölçüm olmuştur. Bu ölçümle birlikte, literatürdeki en üst teknikler (state-of-the-art) kullanılarak yapılmış teorik hesaplamalar, elde edilen deneysel sonuçlar karşısında daha hassas bir biçimde test edilmiştir. Bu çalışma sonu-

cunda ileri QCD orderlarındaki hesaplamaların LHC verisini daha iyi açıklayabildiği kanıtlanmıştır.

İkinci ölçüm kapsamında, 13 TeV'lik veri kullanılarak, top kuark çiftine eşlik eden Underlying Event (UE) ölçümü gerçekleştirilmiştir. Burada UE ile kast edilen, proton-proton çarpışmasında, fiziki olarak önem arz eden parton çarpışması haricinde gerçekleşen, diğer çarpışmalar ve proton kalıntılarıdır. UE, MC hesaplamalarında perturbatif olmayan QCD etkileri içerdiğinden, kesin olarak hesaplanamamakta, ve parametrik olarak Monte Carlo hesaplarına dahil edilmektedir. Bu parametreler önceki deneysel sonuçları kullanarak "ayar" edilmektedir. Bu çalışmada, ayarların top kuark skalasına da geçerliliği, 13 TeV'de ilk kez test edilmiştir. Bu şekilde, parçacık fiziğinde bilinen en yüksek skala olan top kuark kütle skalasında da geçerli olduğu gösterilmiştir.

Anahtar Kelimeler: LHC, CMS, Standart Model, Z bozonu, jetler, top kuark, Underlying Event

*to my great family*

## ACKNOWLEDGMENTS

This thesis was written in the great environment at CERN and the CMS experiment, where I have had the inspiration for my research. Firstly, I would like to express my sincere gratitude to Prof. Dr. Mehmet Zeyrek who encouraged me all the time for my studies since ten years and for giving me the opportunity to carry out my research at CERN. It has been an honour to be a student of him.

I am grateful to Dr. Efe Yazgan, without whom neither my research career within CMS would not have been started, nor this thesis would have been possible. Also I am grateful to his family for their friendship.

Many thanks to TexasTech group, namely Prof. Dr. Nural Akchurin, Prof. Dr. Sung-Won Lee, and Dr. Kittikul Kovitanggoon for the collaboration starting with my M.Sc. thesis. I would like to thank to Dr. Philippe Gras, for his heroic efforts in guiding all of us in the group and having the publication of the article just in time. I wish to also thank ULB group; Prof. Dr. Laurent Favart, Dr. Tomislav Ševa, and Dr. Alexandre Léonard with whom we spent many hours to get the final results, after many hours of code debugging sessions. It was a great pleasure to work with you all.

I would like to thank to the convenors of Standard Model and top quark physics analysis groups of CMS, for the continuous work of organisation and guidance of many analyses, including the ones presented in this thesis.

Special thanks to dearest friends at CERN, Dr. Sezen Sekmen, Dr. Sami Kama, Özgür Sahin, Özgün Kara, Aydın Özbey (...), for their friendship. Special thanks to Hüseyin Yıldız for encouraging me for table tennis. Thanks to my dearest compatriots, Dr. Giannis Flouris, Dr. Halil Saka and Savvas Kyriakou for the good times we shared together at CERN, unfortunately at different times.

To be the members of METU High Energy Physics research team and being at METU have contributed significantly to my personal and professional life, that I will never

forget.

Many thanks for my office-mates, Gamze Sökmen and Dilek Kızılören for the discussions and good memories. Thanks to my dearest friend Nuhcan Akçit for the endless discussions about politics and life.

Many thanks to the Thesis Investigation Committee (TIK) members, Prof. Dr. Mehmet Zeyrek, Prof. Dr. Müge Boz Evinay and Assoc. Prof. Dr. İsmail Turan, for following the research carefully from day one till the end.

I gratefully acknowledge Turkish Atomic Energy Authority (TAEK) for the funding sources that made my Ph.D. work possible, to carry out my research at CERN. The research was funded by two METU-TAEK projects.

Lastly, I would like to thank to my family, to whom this thesis is dedicated, for all their motivation and love. I owe my deepest gratitude to my loving and inspiring wife Göksu who believed in me when I was at the start of this road ten years ago.

## TABLE OF CONTENTS

ABSTRACT . . . . .	v
ÖZ . . . . .	vii
ACKNOWLEDGMENTS . . . . .	x
TABLE OF CONTENTS . . . . .	xii
LIST OF TABLES . . . . .	xvii
LIST OF FIGURES . . . . .	xx
CHAPTERS	
1 INTRODUCTION . . . . .	1
2 THEORETICAL BACKGROUND . . . . .	7
2.1 The Standard Model . . . . .	7
2.1.1 The ElectroWeak (EW) Theory . . . . .	9
2.1.1.1 The EW Symmetry Breaking . . . . .	9
2.1.2 Quantum ChromoDynamics (QCD) . . . . .	10
2.1.2.1 Jets . . . . .	11
2.2 Cross Section Calculation . . . . .	11
2.2.1 Z + Jet Production . . . . .	12



2.2.2	Top Quark Production . . . . .	12
2.3	Cross Section in Hadron Collisions . . . . .	13
2.4	Monte Carlo Technique . . . . .	15
2.4.1	MC Configurations Used . . . . .	17
2.4.1.1	Z + jet Samples . . . . .	18
2.4.1.2	$t\bar{t}$ Samples . . . . .	19
3	EXPERIMENTAL SETUP . . . . .	21
3.1	The LHC Machine . . . . .	21
3.1.1	Luminosity . . . . .	22
3.1.2	LHC Timeline . . . . .	24
3.2	The CMS Detector . . . . .	25
3.2.1	Coordinate System of CMS . . . . .	27
3.2.2	Tracking System . . . . .	28
3.2.3	Calorimeters . . . . .	29
3.2.3.1	Electromagnetic Calorimeter . . . . .	29
3.2.3.2	Hadron Calorimeter . . . . .	30
3.2.4	The Magnet . . . . .	31
3.2.5	The Muon System . . . . .	32
3.2.6	CMS Trigger and Data Acquisition . . . . .	33
3.2.6.1	L1 Trigger . . . . .	34
3.2.6.2	High Level Trigger . . . . .	35

3.2.7	CMS Software Framework . . . . .	35
3.2.7.1	CMS Data Structure: Event Data Model	36
4	DATA ANALYSIS . . . . .	39
4.1	Analysis Outline . . . . .	39
4.2	Object Definitions and Selection Criteria . . . . .	40
4.2.1	Leptons . . . . .	40
4.2.1.1	Trigger . . . . .	41
4.2.1.2	Electron Reconstruction and Selection	41
4.2.1.3	Muon Reconstruction and Selection .	43
4.2.2	Particle Flow . . . . .	44
4.2.2.1	Vertex and Track Reconstruction . . .	45
4.2.2.2	PF Object Reconstruction . . . . .	46
4.2.2.3	Charged Particle Selection Criteria . .	46
4.2.3	Jet Reconstruction and Selection . . . . .	47
4.2.3.1	b-tagging . . . . .	49
4.2.4	$E_T^{\text{miss}}$ Reconstruction and Selection . . . . .	50
4.3	Pile-Up Reweighting Technique . . . . .	50
4.4	Efficiency Corrections . . . . .	51
4.5	Background Determination and Subtraction . . . . .	52
4.6	Correction for Detector Effects . . . . .	53
4.7	Z + jet Study . . . . .	54

4.7.1	Z Boson Reconstruction . . . . .	55
4.7.2	Unfolding Details . . . . .	58
4.7.2.1	Generator Level Phase-space . . . . .	58
4.7.2.2	Response Matrices . . . . .	59
4.7.3	Residual PU removal in the forward region . . . . .	61
4.7.4	Systematic Uncertainties . . . . .	67
4.7.5	Combination of Electron and Muon Channels . . . . .	69
4.7.6	Results . . . . .	70
4.7.6.1	$d^2\sigma/dp_T(j_1)dy(j_1)$ . . . . .	70
4.7.6.2	$d^2\sigma/dy(Z)dy(j_1)$ . . . . .	74
4.7.6.3	$d^3\sigma/dp_T(j_1)dy(j_1)dy(Z)$ . . . . .	79
4.8	Underlying Event Study with $t\bar{t}$ . . . . .	87
4.8.1	Kinematic Reconstruction . . . . .	87
4.8.2	Categorization of the Events . . . . .	91
4.8.3	Results . . . . .	92
4.8.4	Charged Particle Activity: Inclusive . . . . .	92
4.8.5	Charged Particle Activity: Profile Against $t\bar{t}$ Kinematical Variables . . . . .	94
5	CONCLUSIONS . . . . .	101
5.1	Discussion of Physics Results . . . . .	101
5.2	Summary . . . . .	102
	REFERENCES . . . . .	103

## APPENDICES

A	TRIGGER DETAILS FOR BOTH ANALYSES . . . . .	111
B	UNFOLDING CHECK FOR Z + JET ANALYSIS . . . . .	113
B.1	Pull Test for Unfolding . . . . .	113
B.2	Response Matrices of Z + jet Analysis . . . . .	117
C	CONTROL OF PU CONTAMINATION IN CENTRAL REGION FOR Z + JET ANALYSIS . . . . .	125
D	RESULTS OF Z+JET MEASUREMENTS . . . . .	131
E	SHERPA 2.0.0 DATACARD USED TO GENERATE Z + JET EVENTS	141
	CURRICULUM VITAE . . . . .	145

# LIST OF TABLES

## TABLES

Table 2.1	$pp \rightarrow \ell^+ \ell^-$ total inclusive cross section values used in the predictions in data-theory comparison plots for Z+jet analysis. The cross section used for the plots together with the "native" cross section of the generator and their ratio ( $k$ ) are provided corresponding the di-lepton mass window used in the calculation. . . . .	19
Table 4.1	Electron selections used in this analysis. More details can be found in [1]. . . . .	43
Table 4.2	Muon selections used in this analysis. . . . .	45
Table 4.3	Jet selection criteria used in this analysis. . . . .	49
Table 4.4	Monte Carlo Samples. . . . .	53
Table 4.5	Number of events reconstructed in data and Monte-Carlo in each $N_{jet}$ bin in muon channel. . . . .	55
Table 4.6	Leading jet $p_T$ ( $2.5 <  y(j_1)  < 3.2$ ) . . . . .	67
Table 4.7	Definition of the soft event regions. . . . .	91
Table A.1	Di-lepton and single-muon triggers used in the analyses. . . . .	111
Table A.2	Identification and isolation criteria using calorimetry and tracker at trigger level for the leading (second leading) electron. . . . .	111
Table D.1	Z rapidity $\times \text{sign}(y(j_1))$ ( $0 < y(j_1) < 0.5$ ) . . . . .	131

Table D.2	Z rapidity $\times \text{sign}(y(j_1))$ ( $0.5 < y(j_1) < 1$ ) . . . . .	132
Table D.3	Z rapidity $\times \text{sign}(y(j_1))$ ( $1 < y(j_1) < 1.5$ ) . . . . .	132
Table D.4	Z rapidity $\times \text{sign}(y(j_1))$ ( $1.5 < y(j_1) < 2$ ) . . . . .	132
Table D.5	Leading jet $p_T$ ( $0 < y(j_1) < 0.5$ ) . . . . .	133
Table D.6	Leading jet $p_T$ ( $0.5 < y(j_1) < 1$ ) . . . . .	133
Table D.7	Leading jet $p_T$ ( $1 < y(j_1) < 1.5$ ) . . . . .	133
Table D.8	Leading jet $p_T$ ( $1.5 < y(j_1) < 2$ ) . . . . .	134
Table D.9	Leading jet $p_T$ ( $2 < y(j_1) < 2.5$ ) . . . . .	134
Table D.10	Leading jet $p_T$ ( $2.5 < y(j_1) < 3.2$ ) . . . . .	134
Table D.11	Leading jet $p_T$ ( $3.2 < y(j_1) < 4.7$ ) . . . . .	135
Table D.12	Leading jet $p_T$ ( $0 < y(j_1) < 1.5, y(Z) < 1.0, y(Z) \times y(j_1) < 0$ ) . .	135
Table D.13	Leading jet $p_T$ ( $1.5 < y(j_1) < 2.5, y(Z) < 1.0, y(Z) \times y(j_1) < 0$ ) .	135
Table D.14	Leading jet $p_T$ ( $2.5 < y(j_1) < 4.7, y(Z) < 1.0, y(Z) \times y(j_1) < 0$ ) .	136
Table D.15	Leading jet $p_T$ ( $0 < y(j_1) < 1.5, 1.0 < y(Z) < 2.5, y(Z) \times y(j_1) < 0$ )	136
Table D.16	Leading jet $p_T$ ( $1.5 < y(j_1) < 2.5, 1.0 < y(Z) < 2.5, y(Z) \times$ $y(j_1) < 0$ ) . . . . .	136
Table D.17	Leading jet $p_T$ ( $2.5 < y(j_1) < 4.7, 1.0 < y(Z) < 2.5, y(Z) \times$ $y(j_1) < 0$ ) . . . . .	137
Table D.18	Leading jet $p_T$ ( $0 < y(j_1) < 1.5, y(Z) < 1.0, y(Z) \times y(j_1) > 0$ ) . .	137
Table D.19	Leading jet $p_T$ ( $1.5 < y(j_1) < 2.5, y(Z) < 1.0, y(Z) \times y(j_1) > 0$ ) .	138
Table D.20	Leading jet $p_T$ ( $2.5 < y(j_1) < 4.7, y(Z) < 1.0, y(Z) \times y(j_1) > 0$ ) .	138
Table D.21	Leading jet $p_T$ ( $0 < y(j_1) < 1.5, 1.0 < y(Z) < 2.5, y(Z) \times y(j_1) > 0$ )	138

Table D.22	Leading jet $p_T$ ( $1.5 < y(j_1) < 2.5$ , $1.0 < y(Z) < 2.5$ , $y(Z) \times$ $y(j_1) > 0$ ) . . . . .	139
------------	---	-----

Table D.23	Leading jet $p_T$ ( $2.5 < y(j_1) < 4.7$ , $1.0 < y(Z) < 2.5$ , $y(Z) \times$ $y(j_1) > 0$ ) . . . . .	139
------------	---	-----

# LIST OF FIGURES

## FIGURES

Figure 1.1	The summary of CMS measurements of SM cross sections. . . . .	2
Figure 1.2	An illustration of an example pp collision. Illustration shows the parton interaction of interest (red), and multi parton interactions accompanying the interaction of interest(purple). . . . .	5
Figure 2.1	The Standard Model periodic table. . . . .	8
Figure 2.2	Evolution of $\alpha_s$ with respect to Q . . . . .	10
Figure 2.3	Fragmentation of quarks moving away from each other, and forming jets of particles. . . . .	11
Figure 2.4	Drell Yan process for $Z/\gamma^*$ production at hadron colliders. . . . .	12
Figure 2.5	Example Feynman diagrams of tree level Z+jet productions. . . . .	13
Figure 2.6	Example Feynman diagrams of tree level $t\bar{t}$ production and decay. . . . .	13
Figure 2.7	Illustration of QCD factorization theorem. . . . .	14
Figure 2.8	The hadronization of quarks and gluons into hadrons via the Lund String model. . . . .	17
Figure 3.1	The position of LHC tunnel and the experiments. . . . .	21
Figure 3.2	The Layout of LHC and the experiments. . . . .	23



Figure 3.3 Total integrated luminosity of p-p collisions delivered by LHC to the CMS experiment. . . . .	24
Figure 3.4 The proposed schedule of the LHC until 2035 . . . . .	25
Figure 3.5 General Layout of the CMS experiment and the picture showing the barrel and the endcap parts well separated. . . . .	26
Figure 3.6 Transverse View of the CMS detector. . . . .	27
Figure 3.7 Illustration of $\eta$ versus $\theta$ conversion, and CMS coordinate system .	28
Figure 3.8 Schematic cross section through the CMS tracker in the $r - z$ plane	29
Figure 3.9 Schematic view of one quadrant of the calorimetry and tracking system. . . . .	30
Figure 3.10 The HF Calorimeter. . . . .	32
Figure 3.11 CMS Muon system showing the layout of RPC's, DT's and the CSC's. . . . .	33
Figure 3.12 CMS Data Acquisition before LS1. . . . .	34
Figure 3.13 L1 trigger schema. . . . .	35
Figure 3.14 CMSSW modular structure. . . . .	36
Figure 3.15 Content of different Data Tier files for some objects. . . . .	38
Figure 4.1 Number of charged particles versus number of vertices in data and simulation. . . . .	47
Figure 4.2 Illustration of Secondary Vertex and variables used to identify them	50
Figure 4.3 Number of vertex distribution in data and simulation sets, compared after pile-up reweighting technique is performed. . . . .	51
Figure 4.4 Detector level di-lepton invariant mass, from di-muon and di-electron channels, compared with simulation sets. . . . .	56

Figure 4.5 Detector level jet multiplicity, from di-muon and di-electron channels, compared with simulation sets. . . . .	56
Figure 4.6 Detector level rapidity of the jet with highest transverse momentum, from di-muon and di-electron channels, compared with simulation sets. . . . .	57
Figure 4.7 Detector level rapidity of the Z boson reconstructed from di-muon and di-electron pairs, compared with simulation sets. . . . .	57
Figure 4.8 Detector level transverse momentum of the leading jets, from di-muon and di-electron channels, compared with simulation sets. . . . .	58
Figure 4.9 Response matrices for $d^2\sigma/dp_T(j_1)dy(j_1)$ , $d^3\sigma/dp_T(j_1)dy(j_1)dy(Z)$ , and $d^2\sigma/dy(Z)dy(j_1)$ in di-muon channel. . . . .	60
Figure 4.10 The azimuthal angle difference distributions between the Z boson and the jet ( $\Delta\phi(Z,j)$ ) for jets with $y$ [2.5,3.2] for Z+1j exclusive events. The green (red) lines represent the jets that are matched (not-matched) to a gen jet. . . . .	64
Figure 4.11 The azimuthal angle difference distributions between the Z boson and the jet ( $\Delta\phi(Z,j)$ ) for jets with $y$ [3.2,4.7] for Z+1j exclusive events. The green (red) lines represent the jets that are matched (not-matched) to a gen jet. . . . .	65
Figure 4.12 Obtained factors on Data and MC with the ratio MC/Data . . . . .	66
Figure 4.13 The leading jet $p_T$ distributions on MC. The green (red) lines represent the jets that are matched (not-matched) to a gen jet. . . . .	66
Figure 4.14 The differential cross section for Z + jets production as a function of the leading jet transverse momentum and rapidity. . . . .	70
Figure 4.15 Ratio to the measurement of $d^2\sigma/dp_T(j_1)dy(j_1)$ obtained with MADGRAPH 5 + PYTHIA 6. . . . .	71

Figure 4.16 Ratio to the measurement of $d^2\sigma/dp_T(j_1)dy(j_1)$ obtained with SHERPA 2. .....	72
Figure 4.17 Ratio to the measurement of $d^2\sigma/dp_T(j_1)dy(j_1)$ obtained with MG5_aMC + PYTHIA 8. ....	73
Figure 4.18 The differential cross section for Z + jetsproduction as a function of the Z boson and leading jet rapidity. ....	75
Figure 4.19 Ratio to the measurement of $d^2\sigma/dy(Z)dy(j_1)$ obtained with MAD- GRAPH 5 + PYTHIA 6. ....	76
Figure 4.20 Ratio to the measurement of $d^2\sigma/dy(Z)dy(j_1)$ obtained with SHERPA 2. .....	77
Figure 4.21 Ratio to the measurement of $d^2\sigma/dy(Z)dy(j_1)$ obtained with MG5_aMC + PYTHIA 8. ....	78
Figure 4.22 The differential cross section for Z + jetsproduction as a function of the rapidities of the Z boson and leading jet, and of the transverse mo- mentum of the jet for the configuration. ....	80
Figure 4.23 Ratio to the measurement of $d^3\sigma/dp_T(j_1)dy(j_1)dy(Z)$ obtained with MADGRAPH 5 + PYTHIA 6. ....	81
Figure 4.24 Ratio to the measurement of $d^3\sigma/dp_T(j_1)dy(j_1)dy(Z)$ obtained with MADGRAPH 5 + PYTHIA 6. ....	82
Figure 4.25 Ratio to the measurement of $d^3\sigma/dp_T(j_1)dy(j_1)dy(Z)$ obtained with SHERPA 2. ....	83
Figure 4.26 Ratio to the measurement of $d^3\sigma/dp_T(j_1)dy(j_1)dy(Z)$ obtained with SHERPA 2. ....	84
Figure 4.27 Ratio to the measurement of $d^3\sigma/dp_T(j_1)dy(j_1)dy(Z)$ obtained with MG5_aMC + PYTHIA 8. ....	85
Figure 4.28 Ratio to the measurement of $d^3\sigma/dp_T(j_1)dy(j_1)dy(Z)$ obtained with MG5_aMC + PYTHIA 8. ....	86

Figure 4.29 Event display of a top-quark pair candidate produced in association with a jet in $x - y$ (left) and $r - z$ (right) views. . . . .	89
Figure 4.30 The obtained invariant mass of top quarks after kinematic reconstruction . . . . .	90
Figure 4.31 Schematic view of the UE regions defined with respect to the azimuthal angle difference between the charged particle candidate and the axis of the $t\bar{t}$ system with a schematic diagram of $t\bar{t}$ decay chain. . . . .	91
Figure 4.32 The charged PF candidate multiplicity distributions for the away, transverse and toward regions as well as for the overall sample. . . . .	93
Figure 4.33 The transverse momentum sum distributions of the charged PF candidates for the away, transverse and toward regions as well as for the overall sample. . . . .	93
Figure 4.34 The average transverse momentum distributions of the charged PF candidates for the away, transverse and toward regions as well as for the overall sample. . . . .	93
Figure 4.35 The number of charged particles vs the angle with respect to the event-by-event axis defined using $p_T^{t\bar{t}}$ for the inclusive and no extra jet events (top), and for the events with one and at least two extra jets (bottom). . . . .	95
Figure 4.36 Sum of the charged $p_T$ vs the angle with respect to the event-by-event axis defined using $p_T^{t\bar{t}}$ for the inclusive and no extra jet events (top), and for the events with one and at least two extra jets (bottom). . . . .	96
Figure 4.37 The average $p_T$ per charged particle vs the angle with respect to the event-by-event axis defined using $p_T^{t\bar{t}}$ for the inclusive and no extra jet events (top), and for the events with one and at least two extra jets (bottom). . . . .	97

Figure 4.38 The number of charged particles vs $p_T^{\bar{t}t}$ for the overall sample and the away (top), transverse and toward regions (bottom) defined with respect to $\Delta\phi$ . . . . .	98
Figure 4.39 Sum of charged $p_T$ vs $p_T^{\bar{t}t}$ for the overall sample and the away (top), transverse and toward regions (bottom) defined with respect to $\Delta\phi$ . . . . .	99
Figure 4.40 The average $p_T$ per charged particle vs $p_T^{\bar{t}t}$ for the overall sample and the away (top), transverse and toward regions (bottom) defined with respect to $\Delta\phi$ . . . . .	100
Figure B.1 Pull test for different jet $y$ ranges. . . . .	114
Figure B.2 Pull test for different jet $y$ ranges. . . . .	115
Figure B.3 Pull test for all jet $y$ ranges combined. . . . .	116
Figure B.4 Response matrices for $d^2\sigma/dp_T(j_1)dy(j_1)$ in di-electron channel. . .	117
Figure B.5 Response matrices for $d^2\sigma/dp_T(j_1)dy(j_1)$ in di-muon channel. . . .	118
Figure B.6 Response matrices for $d^2\sigma/dy(Z)dy(j_1)$ in di-electron channel. . .	119
Figure B.7 Response matrices for $d^2\sigma/dy(Z)dy(j_1)$ in di-muon channel. . . .	120
Figure B.8 Response matrices for $d^3\sigma/dp_T(j_1)dy(j_1)dy(Z)$ in di-electron channel. . . . .	121
Figure B.9 Response matrices for $d^3\sigma/dp_T(j_1)dy(j_1)dy(Z)$ in di-electron channel. . . . .	122
Figure B.10 Response matrices for $d^3\sigma/dp_T(j_1)dy(j_1)dy(Z)$ in di-muon channel.	123
Figure B.11 Response matrices for $d^3\sigma/dp_T(j_1)dy(j_1)dy(Z)$ in di-muon channel.	124
Figure C.1 The azimuthal angle difference distributions between the Z boson and the jet ( $\Delta\phi(Z, j)$ ) for jets with $p_T[24,30]$ GeV for Z+1j exclusive events. The green (red) lines represent the jets that are matched (not-matched) to a gen jet. . . . .	126

Figure C.2 The azimuthal angle difference distributions between the Z boson and the jet ( $\Delta\phi(Z, j)$ ) for jets with  $p_T[30,40]$  GeV for Z+1j exclusive events. The green (red) lines represent the jets that are matched (not-matched) to a gen jet. . . . . 127

Figure C.3 The azimuthal angle difference distributions between the Z boson and the jet ( $\Delta\phi(Z, j)$ ) for jets with  $p_T[40,50]$  GeV for Z+1j exclusive events. The green (red) lines represent the jets that are matched (not-matched) to a gen jet. . . . . 128

Figure C.4 The azimuthal angle difference distributions between the Z boson and the jet ( $\Delta\phi(Z, j)$ ) for jets with  $p_T[50,68]$  GeV for Z+1j exclusive events. The green (red) lines represent the jets that are matched (not-matched) to a gen jet. . . . . 129

# CHAPTER 1

## INTRODUCTION

Particle physics is the quest to understand the main building blocks of matter, and to describe their interactions.

Starting from the discovery of the electrons, we have built our knowledge based on discoveries of the last century. The need to build bigger machines; accelerators of particles became necessary to be able to go deeper into "smaller" sizes. Large Hadron Collider (LHC), is the biggest accelerator ever built which serves the highest energy hadron collisions since its first operation in 2009, aiming to reach the borders of the Standard Model of particle physics and to search for hints beyond that.

The Standard Model of particle physics is the theory which explains the interactions of sub-atomic world describing the discoveries of the last century. It is verified by the previous experiments and at the LHC experiments at a higher energy scale, and it gives a complete explanation to three of the four known forces; weak force, electromagnetic force and the strong force; the only missing piece is the gravitational force, which is out of scope of this thesis.

Particles predicted by the SM were observed previously except the Higgs boson, which is the manifestation of the Higgs mechanism; the mechanism by which the elementary particles gain mass. The last missing piece of SM was discovered by ATLAS and CMS collaborations [2, 3], which makes SM periodic table complete.

Measurements of SM at the LHC plays an important role in testing the theory itself at the frontier energy scales. They also serve as valuable inputs for developing our modelling of the particle physics, mainly via Monte-Carlo simulations as discussed

later. In Figure 1.1 the summary of CMS measurements of SM cross sections is given. Production cross section, which is a measure of "area", is a measure of the "probability" of the given process to happen. As seen in Figure 1.1 the difference between the highest and the lowest "probes" is of  $10^9$ .

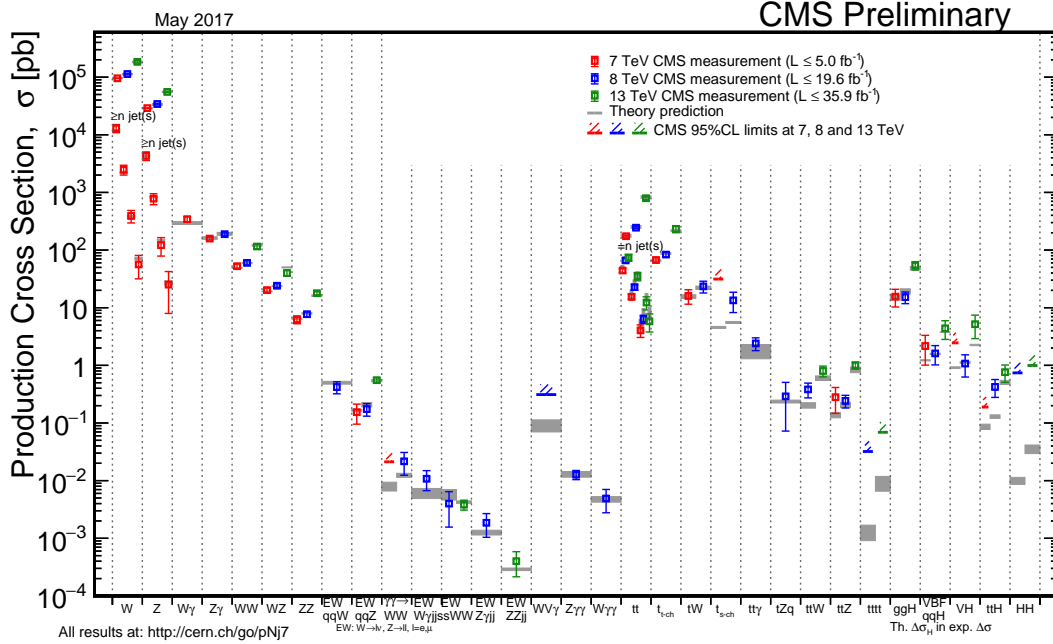


Figure 1.1: The summary of CMS measurements of SM cross sections [4].

This thesis covers two measurements including production of two of the heaviest particles of SM, top quark and the Z boson, in association with jets. In the first measurement, production cross section of Z bosons with jets is measured using 8 TeV data. Second study covers the measurement of Underlying Event variables produced in association with top quark pairs ( $t\bar{t}$ ).

The production of  $Z^0$  bosons in association with jets, or  $Z + \text{jets}$ , plays a crucial role at the LHC. The understanding of jets associated with a Z boson is not only important as a test of perturbative QCD, but also as a significant background in standard model measurements as well as searches for Beyond the Standard Model physics (e.g. SUSY) (eg. associated Higgs Boson production). The precise measurement of the cross section is needed to improve the sensitivity of new physics searches. Measurements of the  $Z + \text{jets}$  cross section were previously reported by the CDF and D0 Collaborations at the Tevatron, and by CMS and ATLAS collaborations at the



LHC. CDF and D0 measurements were carried out using proton-antiproton ( $p\bar{p}$ ) collisions at a centre-of-mass energy  $\sqrt{s} = 1.96$  TeV [5, 6], whereas ATLAS [7, 8] and CMS [9, 10] Collaborations presented results using proton-proton (pp) collisions at  $\sqrt{s} = 7$  TeV. The measurement presented in this thesis is published by the CMS Collaboration [11], which is using proton-proton (pp) collisions at  $\sqrt{s} = 8$  TeV. Afterwards, Z + jet measurements have been presented by ATLAS [12] and CMS collaborations [13] using 13 TeV data.

LHC Run-II measurements at ultimate precision require improved modeling and dedicated measurements of top quark events. One of the important ingredients in simulations is the description of the underlying event (UE). Over the last several years our understanding and modeling of the UE in a hard-scattering process has improved greatly. The UE consists of the beam-beam remnants and the multiple parton interactions that accompany the hard scattering. In Figure 1.2 an illustration of modelling of an example pp collision is shown.

The observables used to study the UE also receive contributions from initial and final state radiation, as illustrated in Figure 1.2, making it difficult to identify the various components of the scattering uniquely. The topological structure of hard hadron-hadron collisions is used to probe the UE experimentally. On an event-by-event basis, the direction of a "leading object" is used to define measurement regions of  $\eta$ - $\phi$  space. One then examines the number of charged particles and the scalar transverse momentum ( $p_T$ ) sum of the charged particles in the those regions with enhanced sensitivity to the UE.

At the LHC, the UE has been measured using minimum bias events [14, 15, 16, 17, 18], Drell-Yan events [19], and  $t\bar{t}$  events [20]. These studies have used the highest transverse momentum charged particle, the highest transverse momentum charged-particle jet, the highest transverse energy calorimeter jet, and the lepton-pair in Z-boson production as the "leading object". In the following analysis using 13 TeV data, which is presented by CMS collaboration in a Physics Analysis Summary (PAS) [21], the UE in top-quark production is studied using the  $t\bar{t}$  pair as the "leading object" as in the earlier CMS measurement at 8 TeV [20].

The thesis is presented in five chapters. First chapter is giving an introduction. In the

second chapter, a brief theoretical outlook is given with emphasis to SM. Chapter 3 gives a description of the experimental setup; the LHC and the CMS experiment. In Chapter 4 the analyses are described in detail and finally in Chapter 5 a summary of the thesis is given.

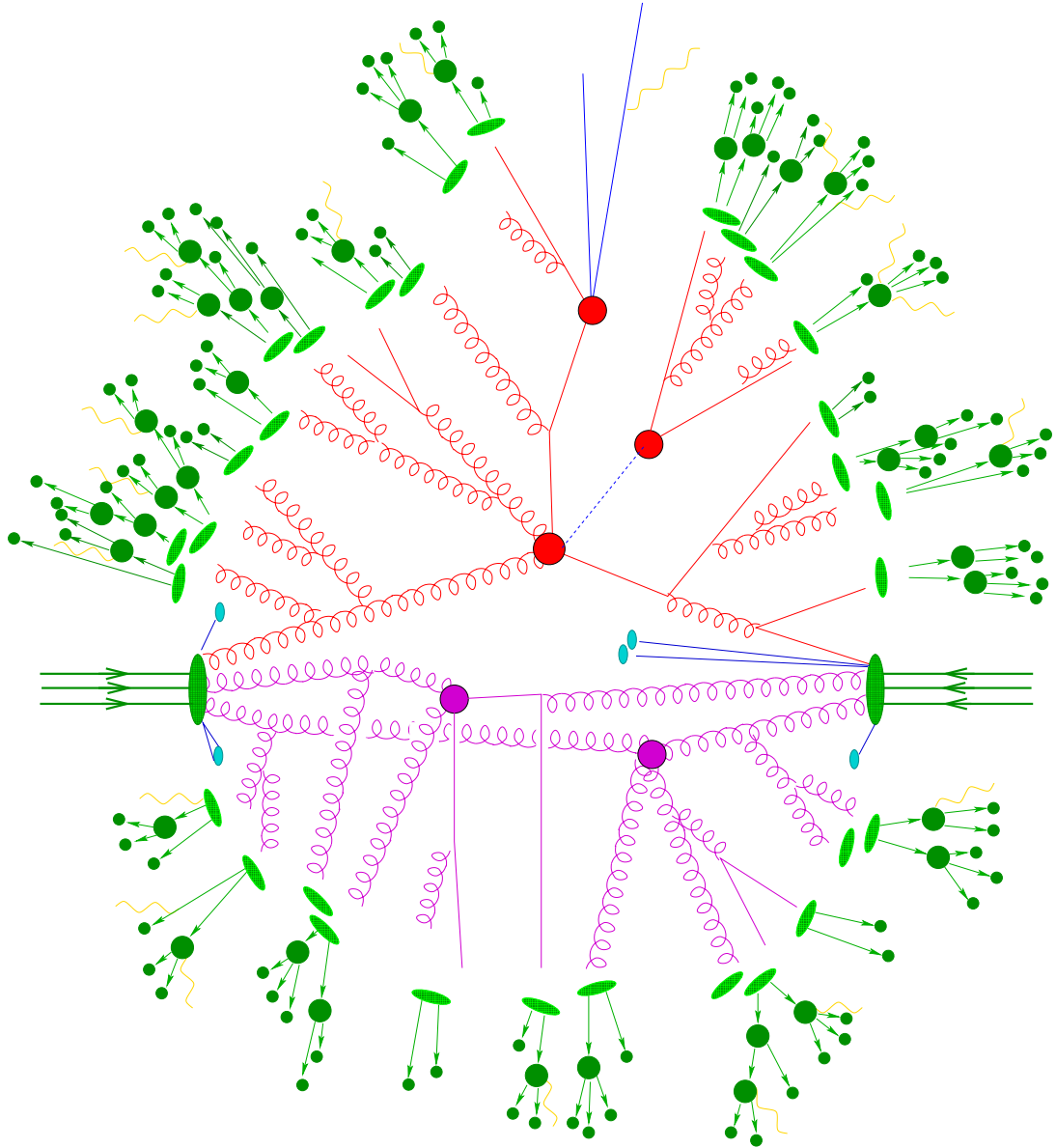


Figure 1.2: An illustration of an example pp collision [22]. Illustration shows the parton interaction of interest (red), and multi parton interactions accompanying the interaction of interest (purple).



## CHAPTER 2

### THEORETICAL BACKGROUND

#### 2.1 The Standard Model

The Standard Model (SM) of particle physics is the theory explaining the physics of sub-atomic world. The theory, formulated in the 1970s, describes the particles, how they interact, and gain mass. The SM gives description to three of the four known forces; electromagnetic, weak, and strong forces. According to SM, each force is mediated by force-carrying bosons. In this section a brief description of SM and its history is given, where the main references are two fundamental textbooks of particle physics [23, 24].

The periodic table of the SM is given in Figure 2.1. The particles are grouped according to their spin; fermions with half integer spin and bosons with integer. Fermions obey Fermi-Dirac statistics and bosons obey Bose-Einstein statistics. Fermions are further divided into two major groups, quarks and leptons, and are grouped into three "families" with increasing mass.

The particles listed in Figure 2.1 gives a complete list of building blocks of matter. Fermions consist of leptons, with integer electric charge, and quarks with fractional charges. Each family of leptons are also denoted as "flavors". Muons and  $\tau$  leptons are heavier versions of electrons, which are "unstable", with lifetimes of  $2.2 \times 10^{-6}$  and  $2.96 \times 10^{-13}$  s respectively. Once produced in collisions, lifetime of muon is long enough to reach the detector and makes it "stable" for colliders, where  $\tau$  leptons decay before reaching the detector.

# Standard Model of Elementary Particles

three generations of matter (fermions)					
	I	II	III		
mass	$\approx 2.4 \text{ MeV}/c^2$	$\approx 1.275 \text{ GeV}/c^2$	$\approx 172.44 \text{ GeV}/c^2$	0	$\approx 125.09 \text{ GeV}/c^2$
charge	$2/3$	$2/3$	$2/3$	0	0
spin	$1/2$	$1/2$	$1/2$	1	0
QUARKS	<b>u</b> up	<b>c</b> charm	<b>t</b> top	<b>g</b> gluon	<b>H</b> Higgs
	$\approx 4.8 \text{ MeV}/c^2$ $-1/3$ $1/2$ <b>d</b> down	$\approx 95 \text{ MeV}/c^2$ $-1/3$ $1/2$ <b>s</b> strange	$\approx 4.18 \text{ GeV}/c^2$ $-1/3$ $1/2$ <b>b</b> bottom	0 0 1 <b>γ</b> photon	
	$\approx 0.511 \text{ MeV}/c^2$ -1 $1/2$ <b>e</b> electron	$\approx 105.67 \text{ MeV}/c^2$ -1 $1/2$ <b>μ</b> muon	$\approx 1.7768 \text{ GeV}/c^2$ -1 $1/2$ <b>τ</b> tau	$\approx 91.19 \text{ GeV}/c^2$ 0 1 <b>Z</b> Z boson	
LEPTONS	$< 2.2 \text{ eV}/c^2$ 0 $1/2$ <b>ν<sub>e</sub></b> electron neutrino	$< 1.7 \text{ MeV}/c^2$ 0 $1/2$ <b>ν<sub>μ</sub></b> muon neutrino	$< 15.5 \text{ MeV}/c^2$ 0 $1/2$ <b>ν<sub>τ</sub></b> tau neutrino	$\approx 80.39 \text{ GeV}/c^2$ $\pm 1$ 1 <b>W</b> W boson	
					GAUGE BOSONS
					SCALAR BOSONS

Figure 2.1: The Standard Model periodic table.

For each charged lepton family corresponds a neutral partner, called the neutrinos ( $\nu$ ), which were first theoretically postulated by Pauli to describe the observed spectrum of nuclear  $\beta$ -decay and they were experimentally proven 26 years later [25].

Quarks, on the other hand, carry fractional charges and are also grouped into three families as leptons. In contrary to leptons, the quarks are not present as single particles; they can only exist in groups of particles.

Antiparticles, which are objects with same properties as of particles except having opposite charge and magnetic moments, were first predicted by Dirac in 1931. The positron, antiparticle of electron was discovered one year later.

The bosons listed in Figure 2.1 are the mediators of forces; photon mediates electro-

magnetic force, gluon is the mediator of the strong force, and W and Z bosons are carriers of the weak force.

As stated before, quarks are not present as single particles but as groups of particles. The quark model, proposed by Gell-Mann and Zweig in 1964 in efforts to describe the patterns of already discovered hadrons, suggests that the hadrons are composed of quarks. The hadrons are grouped into two, baryons and mesons; baryons, having the quantum numbers of an odd number of quarks, and mesons having the quantum numbers of an even number of quarks. The "color" charge, which is an outcome of Pauli's exclusion principle, is postulated. The observed particles, mesons and baryons, have to be "colorless", in other words in certain combinations of the color charges.

Overall, the Standard Model can be written in terms of unitary groups as;

$$SU(3)_{color} \otimes SU(2)_L \otimes U(1)_Y \quad (2.1)$$

Where  $SU(3)_{color}$  corresponds to Quantum Chromodynamics (QCD), whereas  $SU(2)_L \otimes U(1)_Y$  represents the electro-weak interactions,  $Y$  being hypercharge.

### 2.1.1 The ElectroWeak (EW) Theory

ElectroWeak theory is the theory combining two forces of nature, the electromagnetic and the weak forces. The EW theory is represented by  $SU(2)_L \otimes U(1)_Y$  symmetry group mathematically.

#### 2.1.1.1 The EW Symmetry Breaking

Before the spontaneous symmetry breaking, there are three W bosons rising from  $SU(2)$  ( $W^+$   $W^-$   $W^0$ ) and one boson from the  $U(1)$  ( $B^0$ ). The spontaneously broken  $SU(2)_L \otimes U(1)_Y$  symmetry leads to the production of W and Z bosons. After symmetry breaking, the  $W^0$  and  $B^0$  mix and form the massive Z and the massless photon.

$$\begin{pmatrix} \gamma^0 \\ Z \end{pmatrix} = \begin{pmatrix} \cos\theta_W & \sin\theta_W \\ -\sin\theta_W & \cos\theta_W \end{pmatrix} \begin{pmatrix} B^0 \\ W^0 \end{pmatrix} \quad (2.2)$$

Where  $\theta_W$  is the Weinberg mixing angle determined by the gauge couplings of  $SU(2)_L$  and  $U(1)_Y$  symmetries. The W and Z bosons get mass after this breaking, whereas the photon remains massless.

### 2.1.2 Quantum ChromoDynamics (QCD)

QCD is a theory which explains namely the strong interactions; the interactions of the color-charge carrying particles, quarks and gluons. QCD is based on  $SU(3)_{color}$  symmetry. The symmetry has 8-generators, which corresponds to eight types of gluons, which themselves carry color-charges in order to conserve the color charge in strong interactions. Since the gluons carry color-charge, they can self interact strongly. The leptons, not carrying color-charge, do not interact strongly.

The strong coupling constant,  $\alpha_s$ , is the coupling strength parameter of QCD. The evolution of  $\alpha_s$  with respect to the energy scale is given in Figure 2.2. As seen in the figure, at low energy scales  $\alpha_s$  is high, making perturbative calculations in higher orders of it impossible. Perturbative QCD calculations of the differential cross sections include different powers of  $\alpha_s$  at various scales, making the calculation challenging.

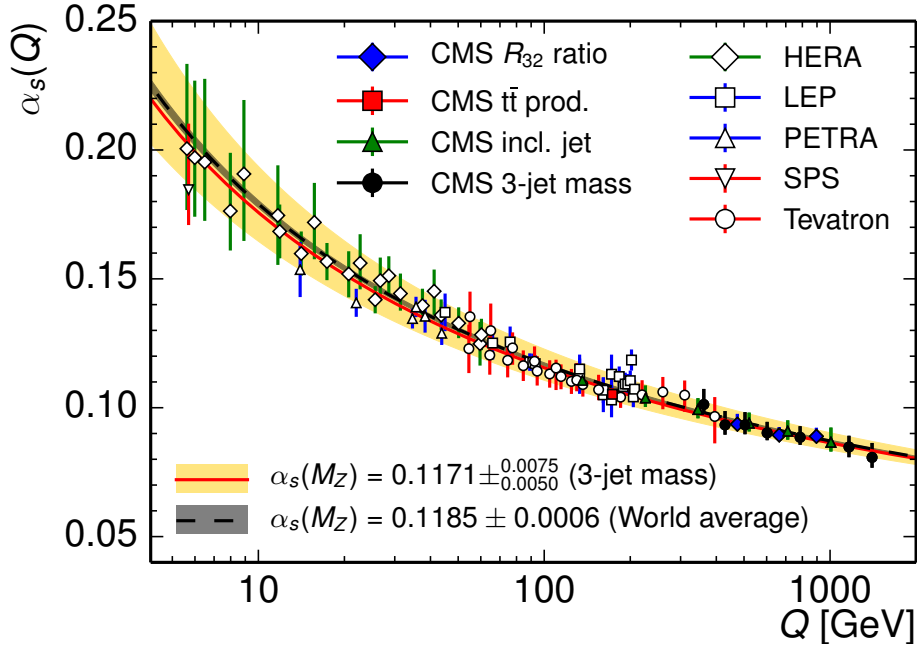


Figure 2.2: Evolution of  $\alpha_s$  with respect to  $Q$  [26].



### 2.1.2.1 Jets

After quarks (or gluons) are created in a collision, it quickly fragments into other particles as illustrated in Figure 2.3. This creates a burst of particles moving in a direction, the jets. What we observe in collisions is not the "bare quarks (or gluons)" but the spray of particles emerging from them. Here the top quark is an exception, as it decays before hadronization starts.

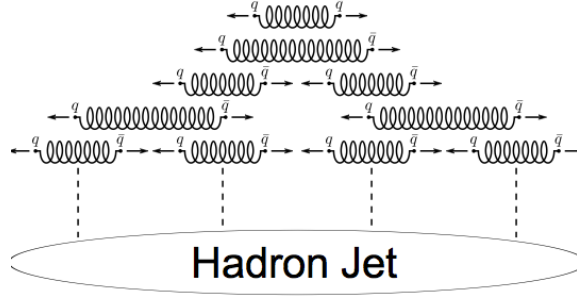


Figure 2.3: Fragmentation of quarks moving away from each other, and forming jets of particles.

## 2.2 Cross Section Calculation

In order to measure the cross section, the "area" representing the probability of a process to happen, the amplitude of the process ( $\mathcal{M}$ ) and the phase space available to it shall be calculated. The amplitude refers to the dynamics of the process calculated from feynman diagrams, where the phase space contains restrictions due to kinematics of incoming and outgoing particles.

From Golden Rule for scattering, once solving for the kinematical phase space restrictions, the cross section of two-body scattering, defined in Center of mass (CM) frame is found to be;

$$\frac{d\sigma}{d\Omega} = \left( \frac{S|\mathcal{M}|^2}{(E_1 + E_2)^2} \right) \frac{|\vec{p}_f|}{|\vec{p}_i|} \quad (2.3)$$

where  $|\vec{p}_f|$  and  $|\vec{p}_i|$  are the magnitudes of incoming and outgoing particle momenta,  $E_1$  and  $E_2$  are the incoming particle energies, and  $S$  is the statistical factor to account

for double counting in case of identical particles.  $|\mathcal{M}|^2$  represents the amplitude square, which gives the probability of the process to occur at "Matrix Element" (ME), calculated using Feynman Rules.

### 2.2.1 Z + Jet Production

The leading order process for the Z production at LHC is the Drell-Yan process, in which a quark and anti-quark from the colliding baryons combine to form the Z boson. The Feynman diagram for the leading order  $Z/\gamma^*$  production is shown in Figure 2.4.

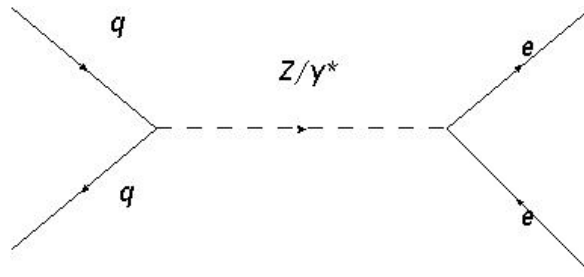


Figure 2.4: Drell Yan process for  $Z/\gamma^*$  production at hadron colliders.

In higher order processes, Z is accompanied by either a gluon or a quark, which then forms the jets. Some of the Feynman diagrams for the  $Z + N$  jet processes are shown in Figure 2.5.

The Z boson, after being produced decays into a pair of fermions. Due to the high mass of the top quark, the decay of Z to top pairs is kinematically forbidden.

### 2.2.2 Top Quark Production

The top quark is the heaviest known particle of the standard model. Unlike other quarks, which form hadrons via hadronisation process after being produced in collisions, the top quark decays through weak interaction before hadronisation can occur. The top quarks decay into a W boson and a b quark, which allows experimentally studying the bare quark properties of top.

The top quarks are produced in top antitop pairs ( $t\bar{t}$ ) as well as single tops. Figure 2.6 shows the Feynman diagram of  $t\bar{t}$  production, and the decay process into so called

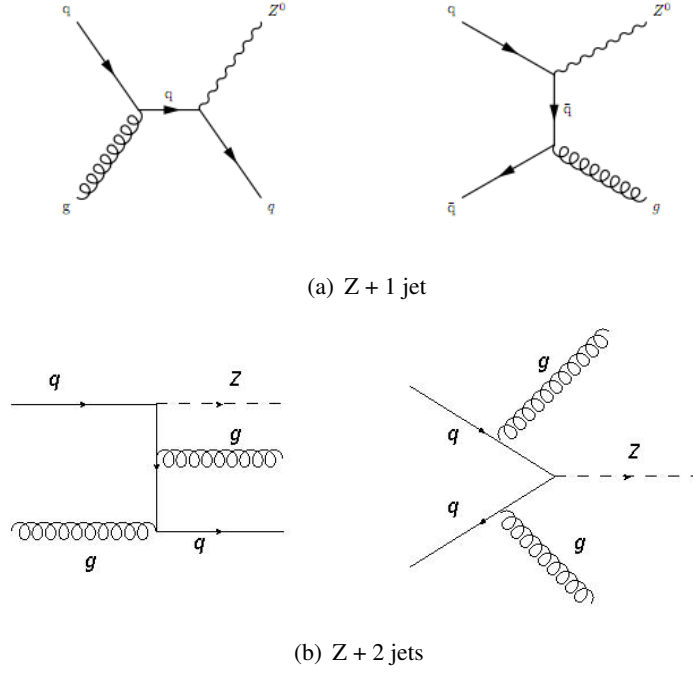


Figure 2.5: Example Feynman diagrams of tree level Z+jet productions.

semi-leptonical channel, where one of the W bosons is decaying into lepton and a neutrino, and the other into quark pairs.

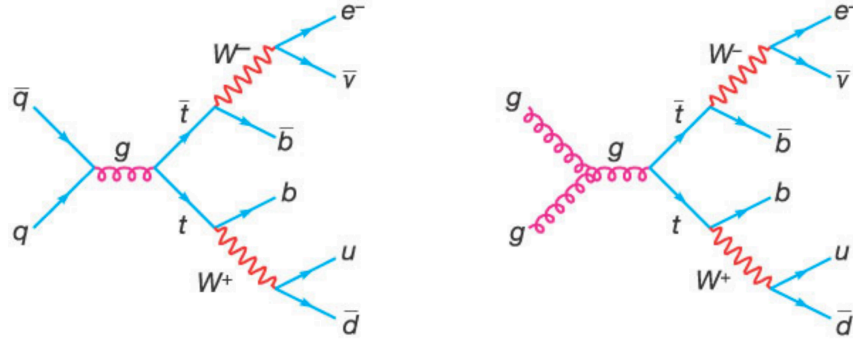


Figure 2.6: Example Feynman diagrams of tree level  $t\bar{t}$  production and decay.

## 2.3 Cross Section in Hadron Collisions

Up to now cross section of processes with partons (quarks or gluons) as the initial state is discussed. On top of this, the cross section of  $pp \rightarrow X$  has to be discussed as follows.

We know from the quark model and from Rutherford like experiments that protons

are not elementary particles, but rather composite particles of partons. Therefore, for the partonic process, the incoming parton shares a fraction of the proton, denoted by Bjorken  $x$  variable.

The probability of having that parton with given momentum fraction and at the given scale is given by the Parton Distribution Functions (PDFs). The PDFs are sets extracted from fixed target and collider experiments and whose scale dependence is described by DGLAP QCD evolution equations [27]. Several collaborations, such as NNPDF [28], CT10 [29], HERAPDF [30] are focusing on improving the PDF knowledge. New measurements from colliders which are sensitive to PDF effects can be used to further constrain the PDF's.

The concept of factorization allows the systematic separation of partonic interactions from physics world of hadrons (color confinement and hadronization). As illustrated in Figure 2.7, the process of  $pp \rightarrow l^+l^-$  as seen on the left diagram is factorised to the illustration on the right, separating the two effects.

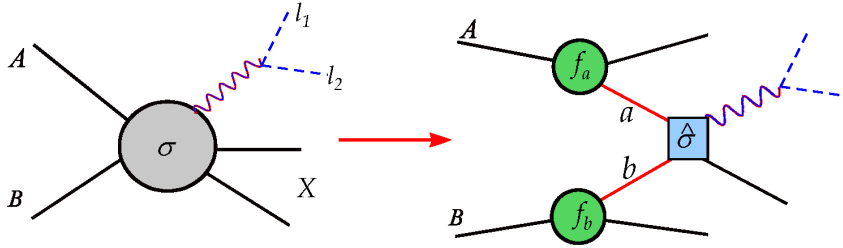


Figure 2.7: Illustration of QCD factorization theorem.[31]

The complete production cross section is separated as the following;

$$\sigma(A, B) = \sum_{a,b} \int dx_1 dx_2 \left[ f_a(x_1, \mu_F^2) f_b(x_2, \mu_F^2) \times \hat{\sigma}_{ab} \left( p_1, p_2, \alpha_s(\mu_R^2), \frac{Q^2}{\mu_R^2} \right) \right] \quad (2.4)$$

Where  $Q^2$  is the physical scale of the parton scattering process.  $\mu_R$  and  $\mu_F$  are arbitrary choices of renormalisation and factorisation scales.  $\hat{\sigma}_{ij}$  is the parton scattering cross section which is calculated using the methods described in the previous section.

Looking back to Figure 1.2, the hard scattering, shown by red blob, is followed by remnants of the protons (cyan blob) and other parton interactions (purple blob). The

detector signal includes all these contributions and it is hard to distinguish them from the physics of interest. There are several methods to clean those effects experimentally and have a "clean" measurement of the process of interest, as discussed in Chapter 4.

## 2.4 Monte Carlo Technique

The integration of Equation 2.4 is mostly analytically impossible for several processes, thus requires numerical computation. Adding higher order corrections to QCD such as including loop contributions make the computation even harder. Monte-Carlo (MC) technique [32] provides the numerical methods to carry out the integration and having samples of processes to be compared directly with the measurements.

There are several MC generators in the market providing those estimations. Some generators estimate Matrix-Element amplitudes separately from parton-shower (PS) and hadronisation step regarding outgoing partons, whereas some gives a complete framework involving that. It is also important to note that the PDF functions are also given as input to MC generators, using LHAPDF [33] for the PDF sets previously described. In this section, the methods used to carry out the integrations with different precisions and the algorithms to link the two are described. A brief outline of the generator set-ups used for the two measurements covered in this thesis is also given.

MADGRAPH:

MADGRAPH 5 [34] is a generator that provides matrix element calculations for High Energy Physics processes such as particle decays and  $2 \rightarrow n$  scatterings. Firstly, a reaction is given with expected initial and final states, with possibility of including/excluding specific resonances in diagrams, decay channels. Then, the Feynman Diagrams for the process with given restrictions are generated. MADGRAPH 5 implements a more efficient tool to generate the Feynman Diagrams than older MADGRAPH versions, which is based on recursively creating sub-diagrams from the diagrams by merging legs. Once the diagrams are generated, the next step is to calculate the ME amplitude for the processes, which is done using HELAS [35] libraries for wave-functions. The amplitude calculation takes care of fermion number conserva-

tion and colour algebra of QCD. Finally, the event generation is done using MADEVENT package [36].

Recently, MADGRAPH 5 generator combined with aMC@NLO under the new MADGRAPH 5\_aMC@NLO [37], which includes NLO precision to the ME calculations, which is a non-trivial problem for QCD calculations; one needs to take into account several problems, such as divergences, and problems with matching with PS as discussed later.

POWHEG:

Positive Weight Hardest Emission Generator (POWHEGv2) [38, 39, 40] is an event generator which aims to generate positive weight events. Within the POWHEG method, unlike MADGRAPH 5, firstly the hardest radiation is generated by using the exact LO matrix elements, then virtual corrections are added for loop diagrams. The obtained calculations can be linked to any of the PS programs.

SHERPA:

"Simulation of High-Energy Reactions of PArticles" (SHERPA) [41] is a Monte Carlo event generator that provides complete hadronic final states without need of other PS programs. Sherpa can carry out calculations for particle production at tree level. Sherpa program has a modular structure, structuring different libraries for different steps of event generation.

On top of tree level calculations, (SHERPA) version 2 allows for NLO ME calculations as well. Sherpa includes a limited number of processes with one-loop corrections. For other processes, it can benefit from libraries of other generators. In the samples used in this thesis, SHERPA 2 (2.0.0) is interfaced with BLACKHAT [42, 43] for NLO calculations. BLACKHAT uses the traditional approach for this one-loop computations, which uses Feynman diagrams.

PYTHIA:

PYTHIA is another generator program being developed for more than 30 years. The program was based on Fortran (PYTHIA 6 [44] ), but it is migrated to C++ (PYTHIA 8 [45]) which is commonly used in High Energy Physics community. PYTHIA is capa-

ble of simulating hard and soft interactions, PDF's, initial and final state PS, Multiple interactions (MPI), and fragmentation and decay of particles. Regarding the content of this thesis, PYTHIA is used for PS simulation and simulation of the Underlying-Event (UE) which consists of Beam Remnants and the MPI.

Lund-string model [46] is used for the fragmentation of quarks and gluons. The gluons in the model are treated as fields forming a "string" of strong color field. Figure 2.8 shows the illustration of formation of strings according to the model.

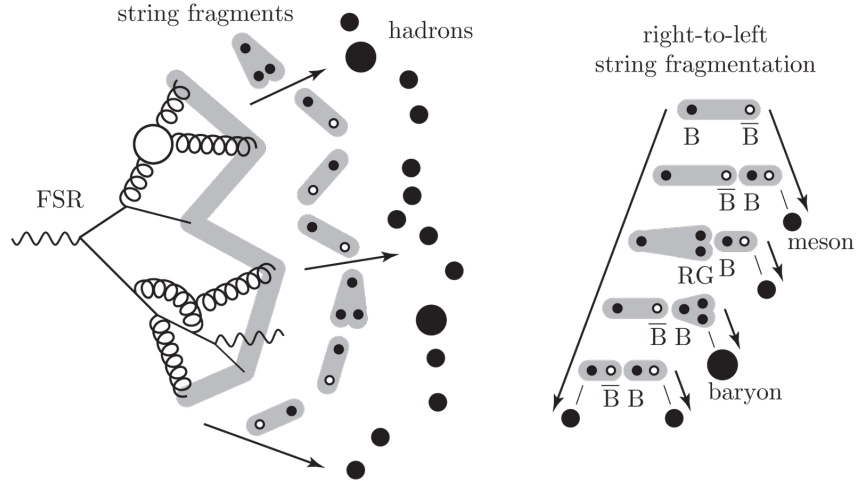


Figure 2.8: The hadronization of quarks and gluons into hadrons via the Lund String model [47].

HERWIG:

HERWIG++ [48] is a general-purpose Monte Carlo event generator that is the C++ version of the HERWIG program which was based on Fortran. Like PYTHIA, the HERWIG generator is used for PS simulation and simulation of the UE. HERWIG provides jet evolution with soft gluon interference via angular ordering. HERWIG++ uses the coherent branching algorithm for PS simulation.

#### 2.4.1 MC Configurations Used

In this section, the configurations based on the MC programs described in the previous section, which are used to generate samples for both analyses, are given with the important technical details.

### 2.4.1.1 Z + jet Samples

The Z + jet measurements are compared to a tree level calculation, and two multileg QCD NLO predictions.

The tree level calculation is done by MADGRAPH v5.1.3.30. The ME calculation is done at tree level for processes with up to four partons accompanying the Z boson in the final state. For the ME calculations, strong coupling constant  $\alpha_s$  is set to 0.130 at the Z boson mass scale. The generator is interfaced with PYTHIA 6.4.26 for parton showering and hadronisation. The PDF set provided by CTEQ6L1 [49] is used. For the UE tune, the Z2\* PYTHIA 6 tune [18, 50] is used. To match the parton showering (PS) with the ME calculations the  $k_t$ -MLM scheme is used and the merging scale is set to 20 GeV.

Two multileg NLO predictions are used, which are including parton showers using the MC@NLO and MEPS@NLO methods.

The first multileg NLO prediction with parton shower is computed with SHERPA 2 (2.0.0) and BLACKHAT for the one-loop corrections. The ME calculation involves  $pp \rightarrow Z + N_{\text{jets}}$  jets with N ranging from zero to four. The calculation provides NLO accuracy in QCD for processes up to two jets, and LO accuracy for jet multiplicities of three and four. The CT10 PDF [29] is used for both the ME calculations and showering description. The merging of PS and ME calculations is done using the MEPS@NLO method and the merging scale is set to 20 GeV.

The second multileg NLO prediction is computed with MadGraph5\_aMC@NLO generator, which provides ME calculation of Z bosons with zero, one and two partons, at NLO accuracy in QCD. The generator is interfaced with PYTHIA 8 which uses the CUETP8M1 tune [50, 51] for parton showering, UE, and hadronisation. The NNPDF 3.0 NLO PDF [28] is used for the ME calculations while the NNPDF 2.3 QCD + QED LO [52, 53] is used for the backward evolution of the showering. The FxFx merging scheme is used to match ME to PS, with a merging scale parameter set to 30 GeV. For the ME calculations, the current PDG world average [54] of  $\alpha_s$  is rounded to  $\alpha_s(m_Z) = 0.118$ . For the showering and underlying events the value of the CUETP8M1 tune,  $\alpha_s(m_Z) = 0.130$ , is used.



Table 2.1:  $pp \rightarrow \ell^+ \ell^-$  total inclusive cross section values used in the predictions in data-theory comparison plots for Z+jet analysis. The cross section used for the plots together with the "native" cross section of the generator and their ratio ( $k$ ) are provided corresponding the di-lepton mass window used in the calculation.

Prediction	Dilepton mass window [GeV]	Native cross section [pb]	Calculation	Used cross section [pb]	$k$
MADGRAPH 5 + PYTHIA 6, $\leq 4$ j LO+PS	$>50$	983	FEWZ NNLO	1177	1.197
SHERPA 2, $\leq 2$ j NLO, 3, 4 j LO+PS	[66, 116]	1059	native	1059	1
MG5_aMC + PYTHIA 8, $\leq 2$ j NLO	$>50$	1160	native	1160	1

For the multileg NLO predictions the normalisation is done to the native cross sections of the generators, whereas the tree level prediction is normalised to the inclusive cross section calculated at next-to-next-to-leading order (NNLO) with FEWZ 2.0 [55] program which uses the CTEQ6M PDF set. The cross section values are shown in Table 2.1.

#### 2.4.1.2 $t\bar{t}$ Samples

The  $t\bar{t}$  signal process have been simulated using the the POWHEGv2 generator which provides NLO accuracy in QCD. The assumed top quark mass in the simulations is 172.5 GeV. The generator is linked with two generators for parton showering and hadronization, PYTHIA8 and HERWIG++. The underlying event tunes used in these simulations are CUETP8M1 and EE5C [56] with PYTHIA8 and HERWIG++, respectively. For both samples NNPDF3.0 PDF set is used.



## CHAPTER 3

### EXPERIMENTAL SETUP

#### 3.1 The LHC Machine

The Large Hadron Collider (LHC) [57] is the largest hadron collider ever built. Clearly LHC is mainly colliding hadrons; namely protons and heavy ions. Apart from ion-ion and proton-ion collisions, it has served proton-proton collisions at a center of mass energy of 7,8 and 13 TeV in different run periods but the design collision energy is 14 TeV.

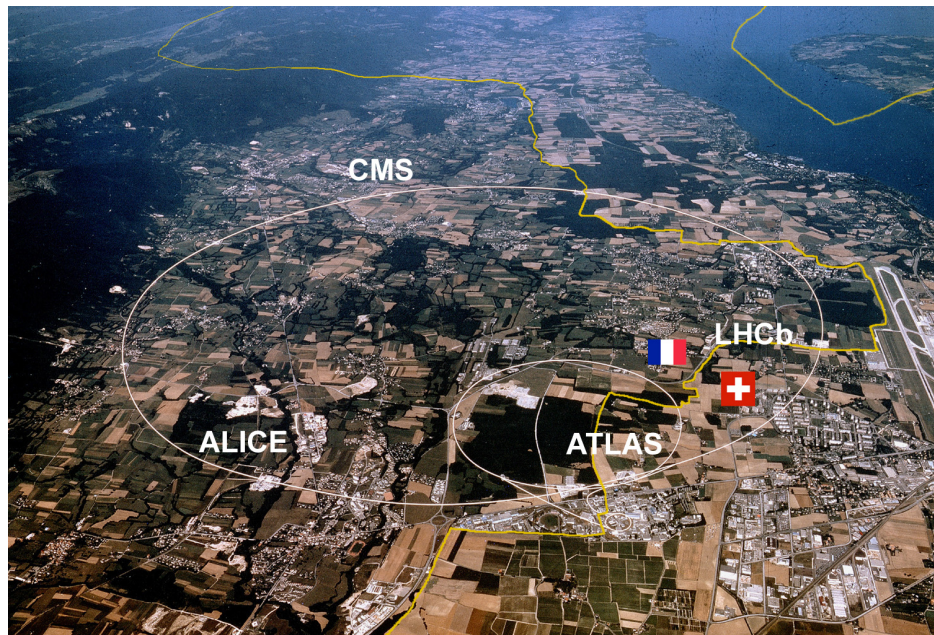


Figure 3.1: The position of LHC tunnel and the experiments [58].

LHC is built in the tunnel of previous accelerator of CERN, the Large Electron Positron Collider (LEP). The tunnel of 27 km in circumference runs between Switzer-

land and France between Lake Lemman and Jura mountains, lying underground at a depth of 50-175 m. LHC is serving collisions at four interaction points, each of which hosts a detector. There are two "general purpose" detectors, ATLAS [59] and CMS [60] covering wide range of physics goals. Two other experiments, designed for specific physics goals are LHCb [61] and ALICE [62] experiments, focusing on b-physics and heavy ion physics respectively. Figure 3.1 shows the position of the LHC and its experiments. Smaller collaborations focusing on forward physics are LHCf [63] and TOTEM [64] experiments. Finally, MoEDAL [65] experiment aims to find magnetic monopoles at the LHC.

As seen in Figure 3.2, the sequence of proton/heavy ion acceleration happens in sequences up to LHC. Firstly, the protons are pushed into the Linear Accelerator 2 (LINAC 2). The source of protons is hydrogen atoms, from which the electrons are separated by applying electric field. Then, being accelerated through BOOSTER, Proton Synchrotron (PS) and Super Proton Synchrotron (SPS), they reach an energy of 450 GeV and are injected into the LHC. The protons are not flowing continuously, but in "bunches" of particles, each of which consist of  $\sim 10^{11}$  particles. These bunches of protons are accelerated to 3.5, 4, and 6.5 TeV of energy per beam particle during different run periods. For the heavy ions the first steps start with LINAC 3, and they reach Low Energy Ion Ring (LEIR). Then, they are injected into PS and follow the same way as protons.

LHC has  $\sim 1600$  superconducting magnets. The dipole magnets are used to keep the proton beams in circular orbit, and the quadrupole magnets squeeze the beam in transverse. The magnets operate at a temperature of about 1.9 K, and the temperature is maintained by sophisticated cryogenics systems using liquid helium.

### 3.1.1 Luminosity

The concept of luminosity [67] at particle colliders is a measure of the rate of collisions that occur. The so called instantaneous luminosity ( $\mathcal{L}_{inst}$ ) is defined as follows:

$$\mathcal{L}_{inst} = \frac{dN}{dt} / \sigma_p \quad (3.1)$$

## CERN's Accelerator Complex

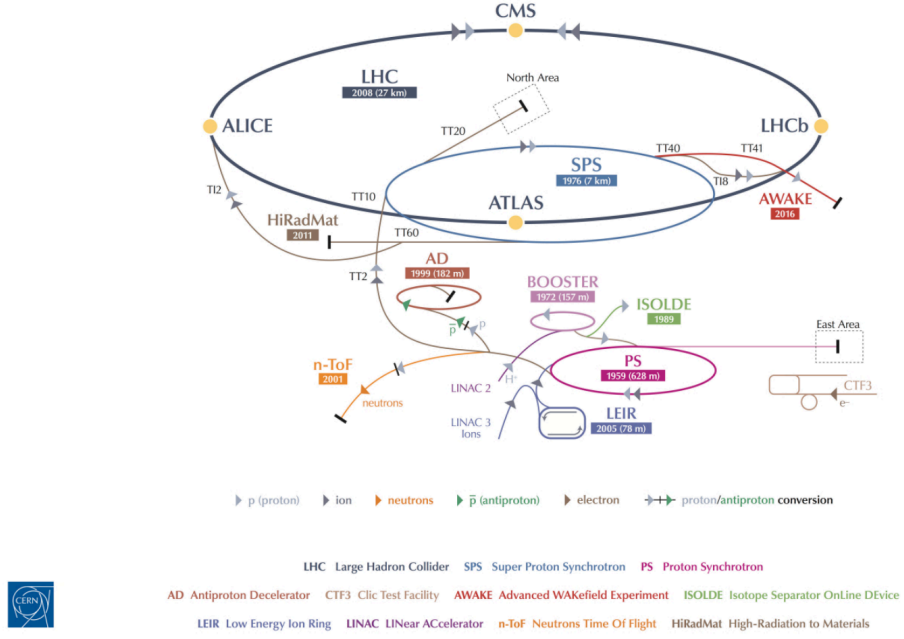


Figure 3.2: The Layout of LHC and the experiments [66].

where  $\frac{dN}{dt}$  is the number of events per time of a given process with cross section  $\sigma_p$ , hence has the unit  $\frac{1}{\text{area} \times s}$ .

For a head-on collision of two gaussian beams,  $(\mathcal{L}_{inst})$  is described as;

$$\mathcal{L}_{inst} = \frac{N_1 N_2 f N_b}{4\pi \sigma_x \sigma_y} \quad (3.2)$$

where  $N_1$  and  $N_2$  are number of bunches in the two beams,  $N_b$  is the number of particles in each bunch,  $\sigma_x$  and  $\sigma_y$  ..... and  $f$  is the frequency of bunches.

The integrated luminosity  $(\mathcal{L}_{int})$  is the measure of total collisions accumulated. It is defined as;

$$\mathcal{L}_{int} = \int_{t_0}^{t_1} \mathcal{L}_{inst} dt \quad (3.3)$$

and has dimension  $\frac{1}{\text{area}}$ . For a process of  $\sigma_p$  the total number of events  $N$  delivered is expected to be;

$$N = \mathcal{L}_{int} \times \sigma_p \quad (3.4)$$

The observed number of events is reduced by reconstruction efficiencies as discussed in Chapter 4. Figure 3.3 shows the total integrated luminosities delivered by the LHC to the CMS experiment. For the studies in this thesis, two datasets collected in 2012 and 2015 are used, at 8 and 13 TeV energies. The datasets correspond to  $19.6 \text{ fb}^{-1}$  and  $2.2 \text{ fb}^{-1}$  respectively.

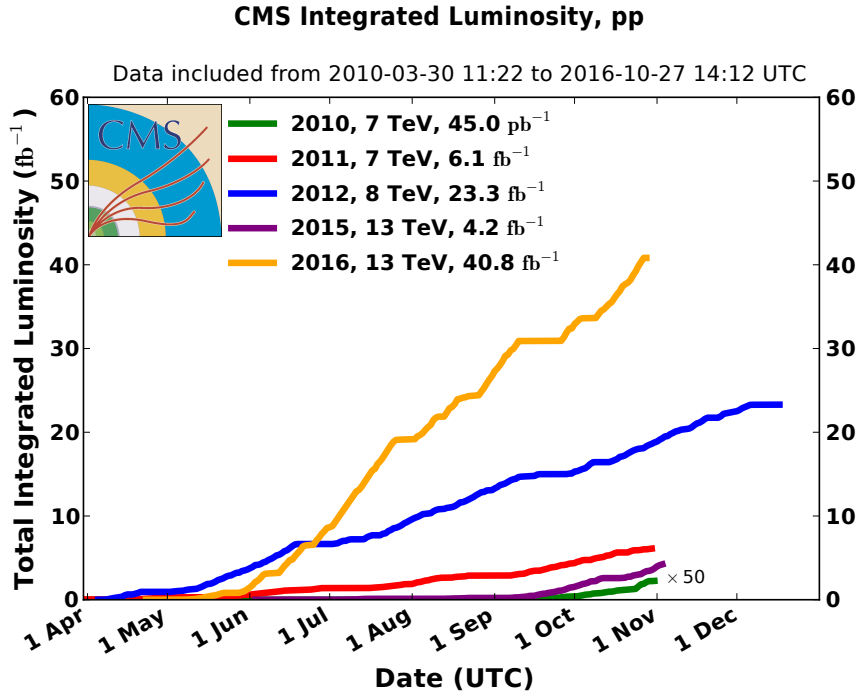


Figure 3.3: Total integrated luminosity of p-p collisions delivered by LHC to the CMS experiment [68].

### 3.1.2 LHC Timeline

LHC has undergone series of upgrades between Run I and II, and is planned to be further upgraded to achieve further goals [69]. So called Phase II is named as High-Luminosity LHC (HL-LHC) which aims to deliver more luminosity. To cope with this development, the experiments are planned to undergo various upgrades. The proposed calendar of LHC run periods can be seen in Fig. 3.4 where LS stands for Long Shutdown. LHC has served collisions until 2012 summing up to  $25 \text{ fb}^{-1}$  for pp,

and has undergone a LS period in 2013 and 2014. After this, RunII period started and LHC already served  $30 \text{ fb}^{-1}$  pp collision data. In Run II the total amount of collisions to be delivered by the LHC is planned to be  $100 \text{ fb}^{-1}$ .

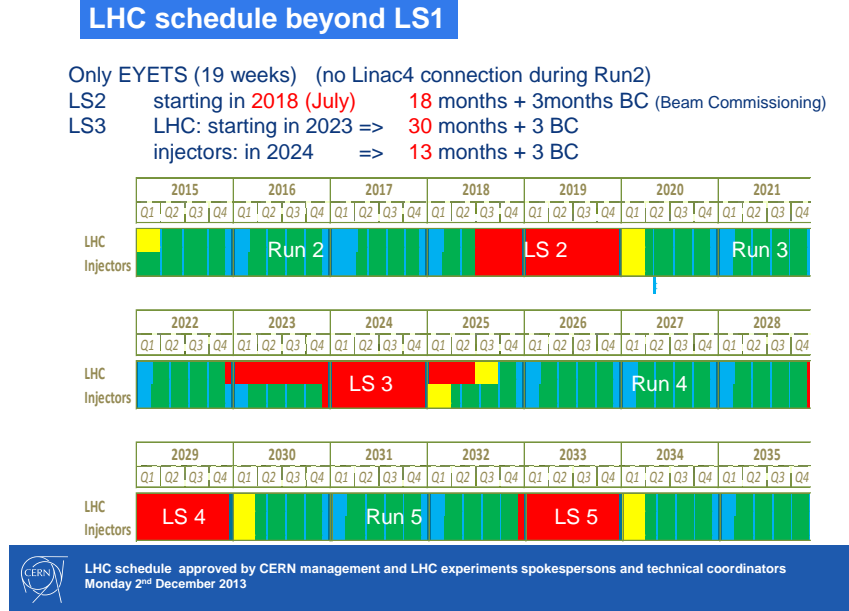


Figure 3.4: The proposed schedule of the LHC until 2035

### 3.2 The CMS Detector

The Compact Muon Solenoid detector (CMS) is a general-purpose detector on the LHC to detect particles coming from collisions. The experiment sits in the cavern at P-5 of the LHC, situated near Cessy, France as seen on the map shown in Figure 3.1. CMS, like its other collision experiments, consists of many sub-detectors built like a "cylindrical onion" as layers in sequence, each of which aims to measure the properties of different particles emerging from the interactions. General layout of the experiment and a picture showing the barrel and the endcap parts well separated are shown in Figure 3.5.

The transverse view of the CMS detector showing the different layers of sub-detectors is shown in Figure 3.6, showing how different particles leave signal in the CMS detector.

CMS detector is planned to undergo series of upgrades [71] to cope with updating



# CMS Detector

Pixels  
 Tracker  
 ECAL  
 HCAL  
 Solenoid  
 Steel Yoke  
 Muons

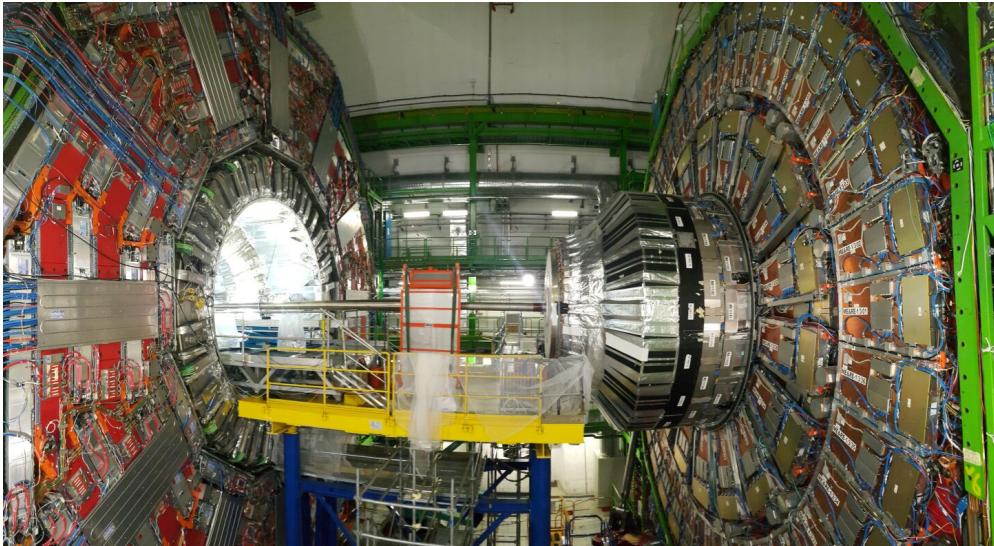
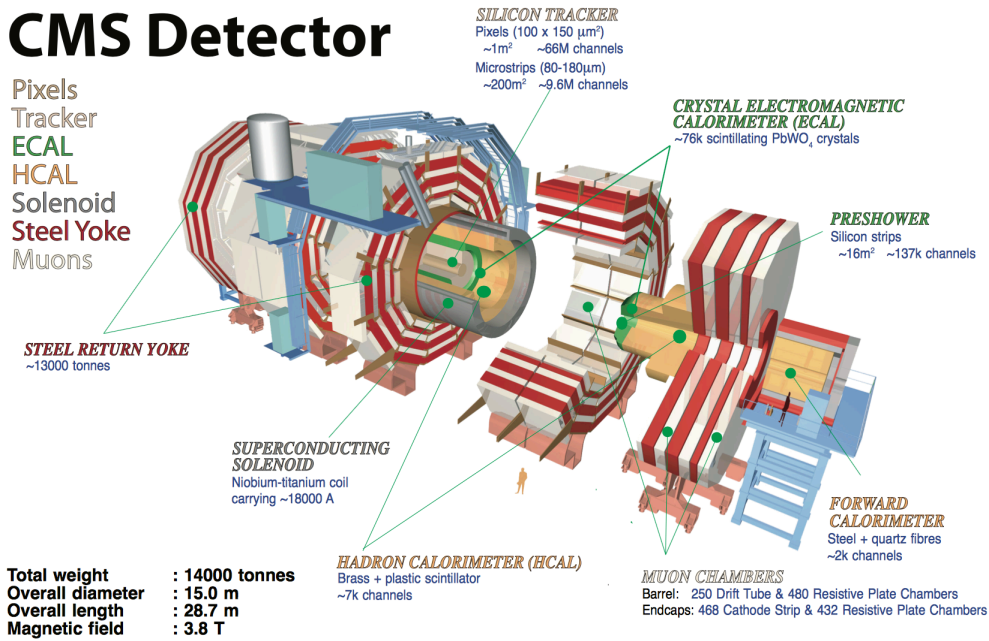


Figure 3.5: General Layout of the CMS experiment [70] and the picture (©B. Bilin, March 2017) showing the barrel and the endcap parts well separated.

LHC conditions and the aging of the existing detector materials, as well as benefit from developing technologies. The upgrades are planned to happen in two steps, one of which already happened during LS1 between Run I and Run II periods of LHC data taking. The second step will be happening in the next LS of the LHC. The upgrades already done includes several parts of the detector, such as change of the beam-pipe within the detector, changes on the tracker, repairs of electromagnetic calorimeter



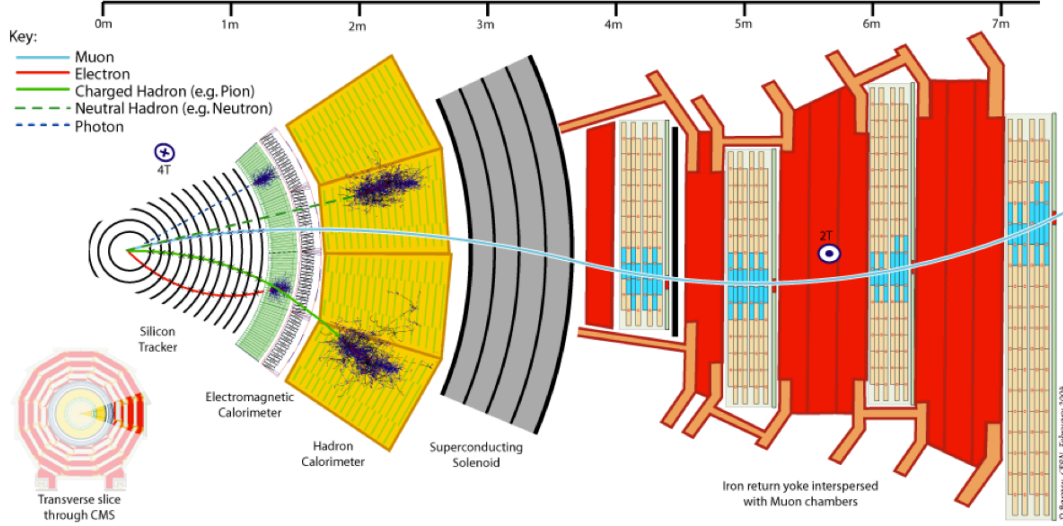


Figure 3.6: Transverse View of the CMS detector [70].

preshower, changes in hadronic calorimeter forward detector, upgrade of the Data Acquisition system, and improvements to the CMS muon system.

### 3.2.1 Coordinate System of CMS

CMS uses right-handed coordinate system with x-axis pointing towards the centre of LHC, y pointing upwards to the sky and z pointing in anti-clockwise direction of the LHC. The polar angle,  $\theta$  is defined relative to positive z-axis, where the azimuthal angle,  $\phi$  is defined relative to the x-axis.

In collider physics, pseudorapidity,  $\eta$  is used to physically describe the angular position of the particles. The pseudorapidity is defined as  $-\ln(\tan(\theta/2))$ . So,  $\theta$  interval  $[0^\circ, 180^\circ]$ , corresponds to  $\eta$  in  $[\infty, -\infty]$ .  $\eta = 0$  corresponds to  $90^\circ$ , as illustrated in Figure 3.7, along with CMS coordinate system.

The pseudorapidity can be expressed in terms of particle momentum as follows:

$$\eta = \frac{1}{2} \ln \left( \frac{|\vec{p}| + p_L}{|\vec{p}| - p_L} \right) \quad (3.5)$$

For massless particles, or particles with  $m \ll p$ ,  $\eta$  is equivalent to the relativistically

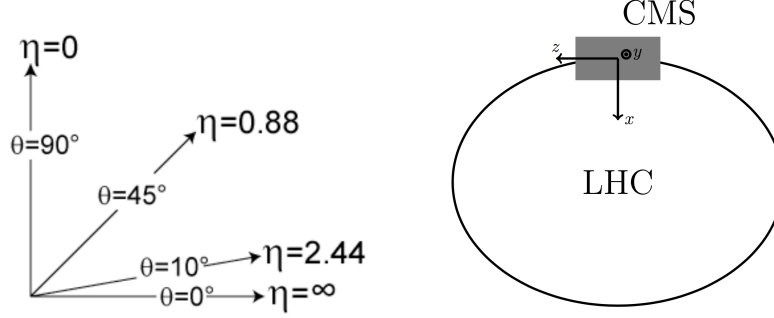


Figure 3.7: Illustration of  $\eta$  versus  $\theta$  conversion, and CMS coordinate system

invariant quantity, rapidity ( $y$ ) expressed as;

$$y = \frac{1}{2} \ln \left( \frac{E + p_L}{E - p_L} \right) \quad (3.6)$$

In the following chapters,  $\eta$  is used to define detector boundaries and lepton selections. The measurements are done with respect to  $y$ , since measurements involve heavy particles for which  $\eta$  is not invariant in boosts, hence physically not useful. As discussed later,  $y$  can be a direct measure of boost between frames.

### 3.2.2 Tracking System

The tracking system [72] is the first sub-detector after the collision point, and aims to measure the momentum and trajectory of the charged particles. The CMS tracking system consists of two systems, the pixel detector and the silicon strip detectors. The schematic cross section of CMS tracking system is shown in Figure 3.8. The tracker consists of 1440 pixel and 15148 strip detector modules covering pseudorapidity range of  $|\eta| < 2.5$ . As a charged particle moves through those modules, it creates electric signals which are then amplified and detected, which are called "hits". The tracks of the charged particles are then reconstructed from these "hits". CMS tracker reconstruct charged particle trajectories with high resolution.

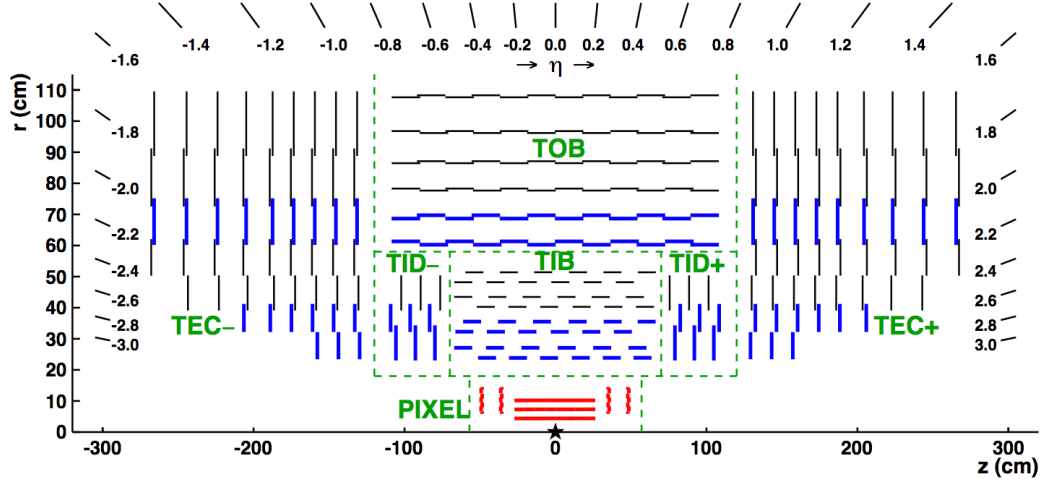


Figure 3.8: Schematic cross section through the CMS tracker in the  $r - z$  plane

### 3.2.3 Calorimeters

The electromagnetic and hadron calorimeters of CMS, which are the next layers after the tracker, form a complete calorimetry system. This is important for the measurement of leptons, jets and missing transverse energy. The calorimeters are briefly described here. Schematic view of one quadrant of the calorimeters is shown in Figure 3.9.

#### 3.2.3.1 Electromagnetic Calorimeter

The Electromagnetic Calorimeter (ECAL) [73] surrounds the Tracker, aiming to measure the energies of the particles interacting electromagnetically. It spans over a pseudorapidity region of  $|\eta| < 3.0$  and has two parts, the Barrel (EB) and the Endcap (EE); both in the solenoid magnet volume. EB covers the central region of  $|\eta| < 1.479$  and consists of 61200 lead tungstate ( $\text{PbWO}_4$ ) crystals, which are transparent to light as a glass, but heavy. EE covers the region of  $1.479 < |\eta| < 3$  and has 7324 crystals on each side.

When the particles fly through the crystals, they leave some part of their energy by scintillation. The ECAL measures the amount of energy that the particles leave in the crystals by measuring light produced by scintillation which is detected by photodetec-

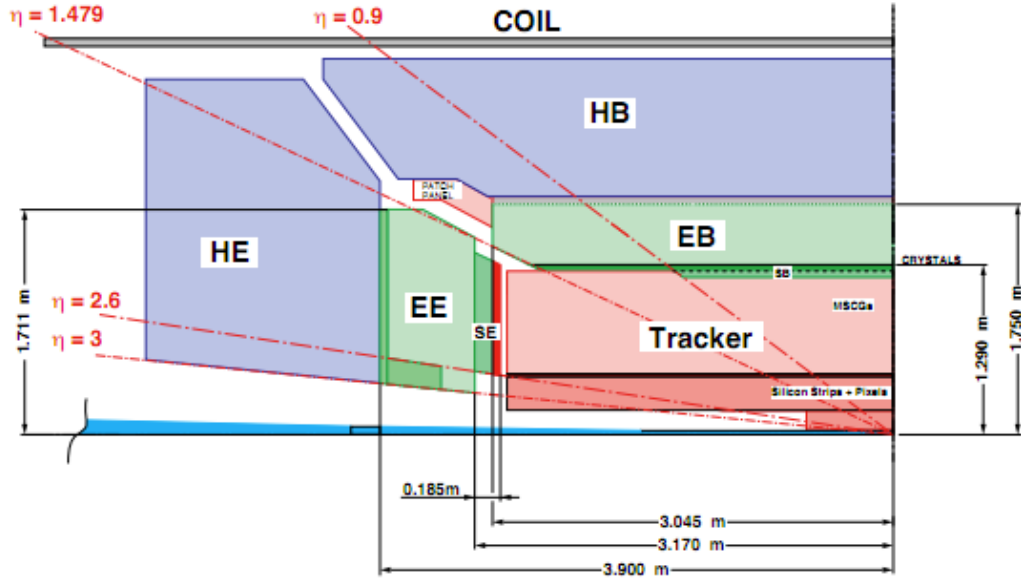


Figure 3.9: Schematic view of one quadrant of the calorimetry and tracking system [73].

tors and converted to electronic signals, and to energy. To capture the light efficiently the crystals have to be transparent to light. The correspondence of the signal to the energy is calibrated using the signal created by particles and light of known energies in wide range. Due to the radiation conditions the crystals are losing their transparency, hence becoming darker. This has to be taken into account during data-taking with special calibration of the ECAL.

### Preshower

The Preshower (ES) is composed of two thin lead converters which lies in front of EE in interval  $1.653 < |\eta| < 2.6$  as seen in Figure 3.5. The aim of the ES is to distinguish single high-energy photons from close pair of low-energy photons. It has a total thickness of 20 cm.

#### 3.2.3.2 Hadron Calorimeter

The next layer of the CMS detector after ECAL is the Hadron Calorimeter (HCAL) [74] aiming to measure energies of particles interacting hadronically. It consists of

central calorimeters (Barrel and Endcap) which sit inside the solenoid magnet within  $|\eta| < 3$ , and forward calorimeters lying outside the magnet.

### **HCAL Barrel (HB) and HCAL Endcap (HE) Calorimeters**

The central hadron calorimeter is made of active material of 4mm thick plastic scintillator tiles; and absorber plates of thickness of 5 cm in HB and 8 cm in HE. The absorber plates are composed of copper. A hadron is stopped by the absorbers and creates showers of charged particles, which then create scintillation in the scintillator tiles. The amount of scintillation is combined and converted to the particles energy. The same procedure of calibration as of ECAL is applied to convert the signals to energy of the particles.

### **HCAL Forward Calorimeter (HF)**

The Forward Calorimeter (HF) [75] covers a range of  $2.853 < |\eta| < 5.191$  and unlike the central HB and HE, HF has absorber plates that are composed of steel and the active material is made of quartz fibers. The choice of quartz is to stand the harsh radiation conditions in the forward region.

The structure of HF is shown in Figure 3.10. As seen in the figure, the HF consists of the absorber structure that is composed of 5 mm thick grooved plates, and the quartz fibers are inserted into these grooves. There are two types of fibers independently measured, with different lengths, namely *long* and *short* fibers. The long fibers run through the whole absorber material of 165 cm in depth, where the short fibers edges stand behind 22 cm of steel. The HF sits beyond the tracker acceptance, making long and short fibers important to distinguish electrons and photons from the hadrons. Electrons and photons deposits its energy mostly on the long fibers and mostly they can not reach the short fibers lying behind 22 cm of steel material. On the contrary, the showers generated by hadrons create signals in both long and short fibers.

### **3.2.4 The Magnet**

The CMS detector [76] has a superconductor solenoid magnet of 6 m of diameter, providing 3.8 T of magnetic field with a current of 18,160 A. The magnet encloses

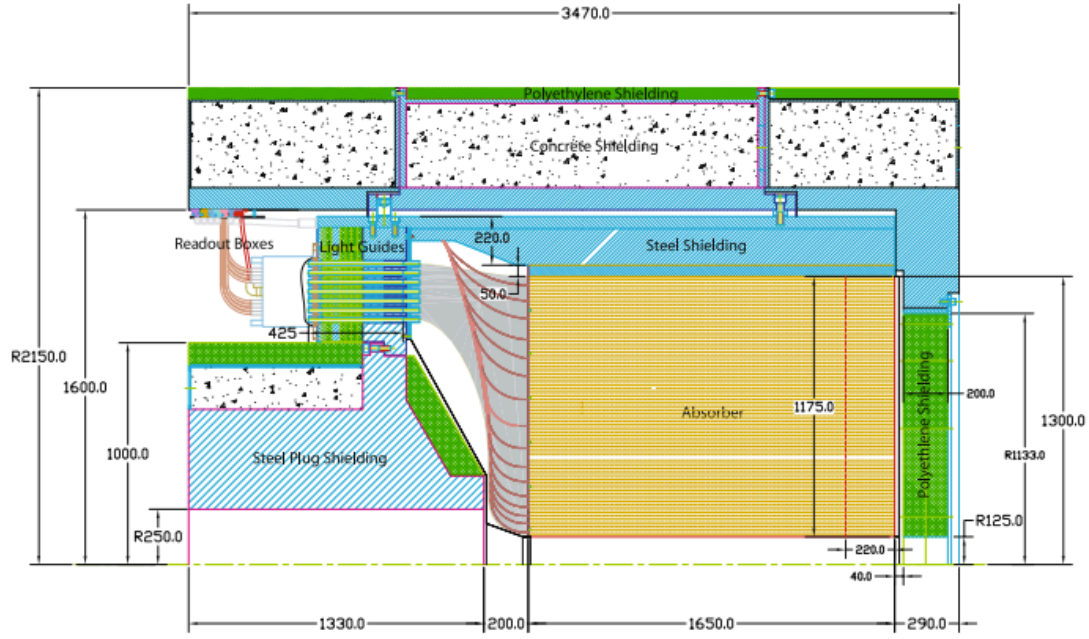


Figure 3.10: The HF Calorimeter [75].

the tracker and the calorimeters, except HF. The energy stored in the magnet is 2.3 GJ. The magnetic field is crucial in detecting particles; in order to bend the paths of the charged particles throughout the detector, hence to be able to measure the charge/mass ratio and the momentum of those particles and to determine the charge.

### 3.2.5 The Muon System

The muon system of the CMS detector [77] aims to identify the muons precisely. The muon system consists of three different kinds of detectors; Drift Tubes (DT), Cathode Strip Chambers (CSC), and Resistive Plate Chambers (RPC). DT's are located at the central barrel region ( $|\eta| < 1.2$ ) and the CSC's are at the endcap region ( $1.2 < |\eta| < 2.4$ ). The RPC's are located at both barrel and endcap. Layout of the CMS Muon system is shown in Figure 3.11.

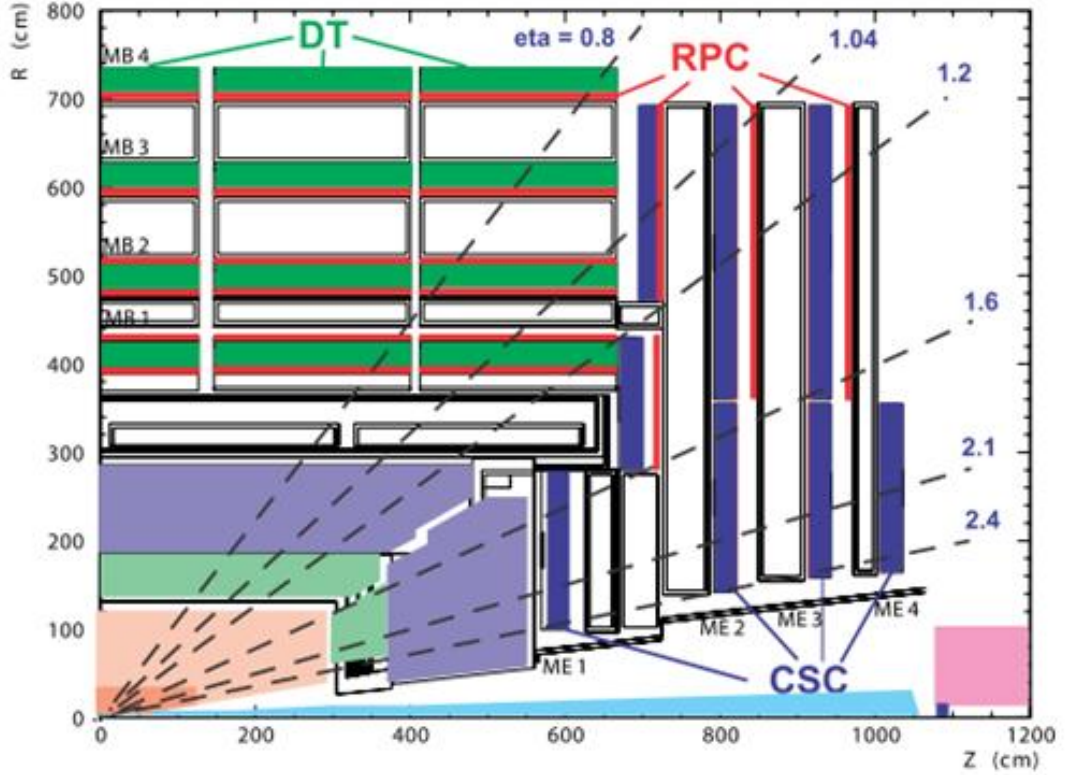


Figure 3.11: CMS Muon system showing the layout of RPC's, DT's and the CSC's [77].

### 3.2.6 CMS Trigger and Data Acquisition

The main goal of the trigger and data acquisition systems [78] is to provide fast and reliable decisions. Out of 20(40) million interactions occurring every second, the output rate should be reduced to order of few 100 events per second. The CMS trigger system is designed in two steps in order to achieve this goal. All of the collected data can be kept for  $3.2 \mu s$  in the buffers before being triggered. Hardware based Level-1 trigger reduces this to 100 kHz, and these events are passed to the High Level Trigger algorithms, eventually reducing to few 100 Hz. The CMS data taking procedure starting from the detector signals is illustrated in Figure 3.12.

There are two levels of triggers as mentioned. The first one, the Level-1, is purely hardware based, and uses the information from calorimeters and the muon systems. The High-Level trigger (HLT) is software based, and contains various algorithms for



different physics purposes. For example, for the Z+jet analysis, the events from double-lepton triggered datasets have been used, while for the  $t\bar{t}$  analysis single-lepton triggered sets are used.

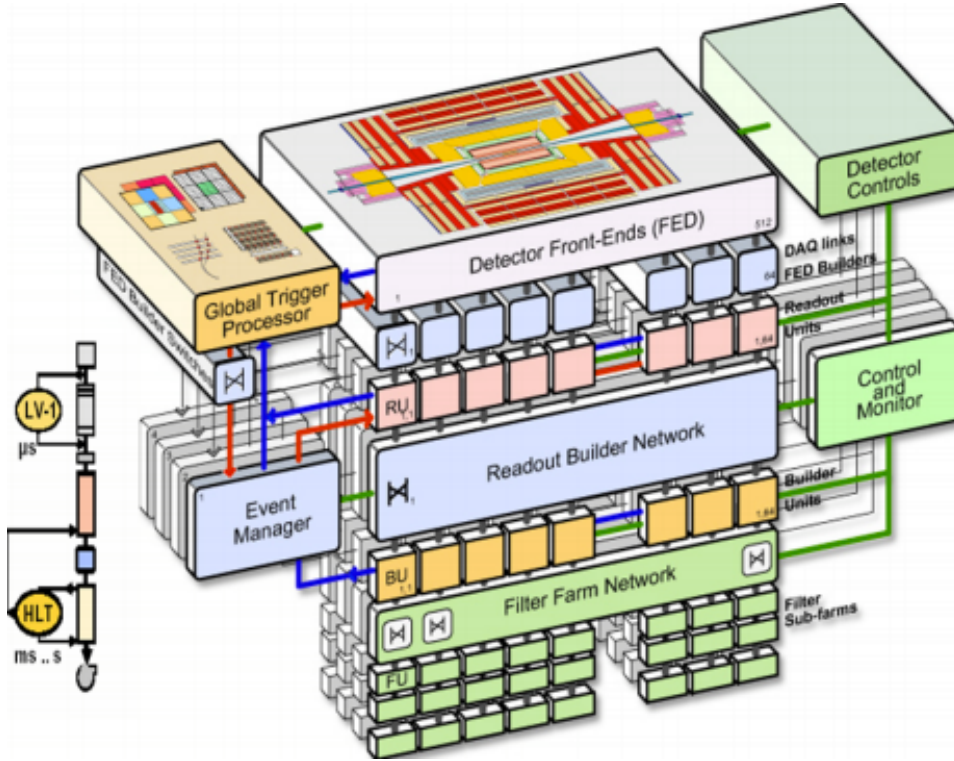


Figure 3.12: CMS Data Acquisition before LS1

### 3.2.6.1 L1 Trigger

The L1 triggers use information from the calorimeters and the muon system, whereas up to now, the tracker information can not be used at this level of triggering due to the big size of the data. There are some efforts to eventually include tracker information in L1 trigger.

The calorimeter L1 trigger uses the reconstructed-hits (rec-hits) of HCAL and ECAL, where the muon trigger L1 relies on the information of the three muon systems. There are various L1 trigger paths. If an event passes one of these L1 paths, the decision is passed to the front ends via the Trigger Timing and Control system(TTC) and the event is taken from the buffers. The ones that do not "fire" any of the triggers are discarded here.



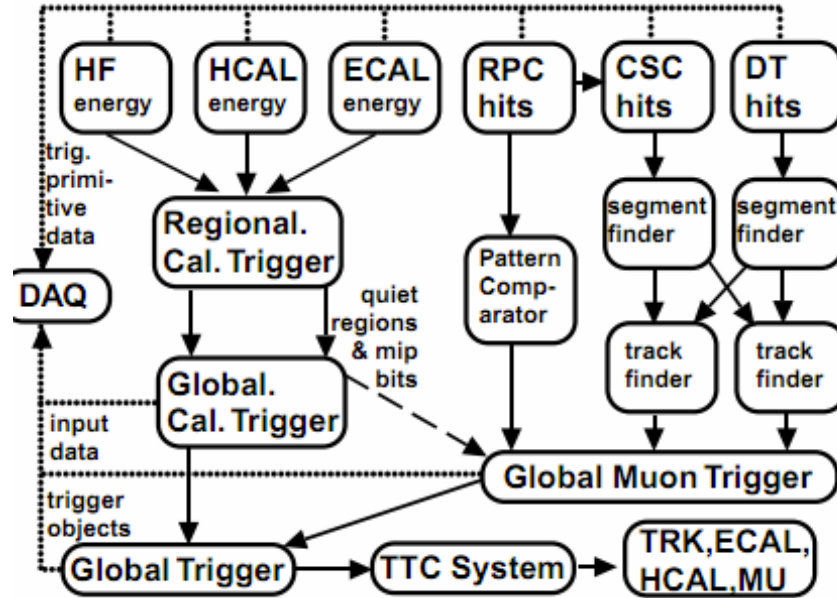


Figure 3.13: L1 trigger schema.

### 3.2.6.2 High Level Trigger

CMS High Level Trigger (HLT) relies on more sophisticated trigger algorithms. For optimal flow of data, event selection is performed in multiple stages by applying High Level Trigger filters. The HLT farm can reach the information used in L1 and some extra that can not be used in L1 step due to time constraints. HLT can reach the full event information with full granularity including tracker information.

Once an event is selected by an HLT path, the event is sent to data centre at CERN, then distributed to other computer centers around the world connected by the grid system to be stored.

### 3.2.7 CMS Software Framework

CMS Software Framework (CMSSW), clear from its name is the framework of different softwares combining all steps from data taking to the analysis level. CMSSW is a "modular" software based on mainly C++, and python is used to link the C++ libraries.

The software is based on Event Data Model (EDM) framework, running with a single

configuration file. The software is based on the concept of an "event", a C++ object container related to a particular collision. The events are stored under a single C++ vector; `edm::Event` vector.

CMSSW consists of many modules for different steps of data taking and data analysis. Example CMSSW modules include `EDProducer`, `EDAnalyzer`, `EDFilter`, `EDLooper` etc. The modular structure of CMSSW is shown in Figure 3.14. As seen in the figure, a single configuration file defines the order and parameters of several modules, which creates the desired output files.

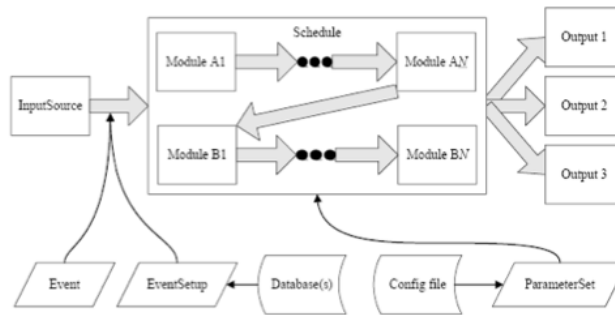


Figure 3.14: CMSSW modular structure.

### 3.2.7.1 CMS Data StructureEvent Data Model

Event Data Model (EDM) [79] forms the basic data structure for storing and further analysing the CMS data offline.

In this concept, an event is defined to be a collection of C++ classes, containing each bit of data of different physical objects such as reconstructed electrons, muons, jets; collections of trigger and signals from different sub-detectors, such as tracker collection, calorimeter rec-hits. etc. All the data and the physical objects are identified from the "signals" they leave in the detector. The physical objects are reconstructed from the detector information through different steps of reconstruction using CMSSW framework. The reconstruction of physical objects will be discussed in Chapter 4.

For the pseudo-data, namely the Monte-Carlo simulations using various models, the events that are generated using MC generators described in Chapter 2 are passed through the detector simulation using GEANT-4 program [80]. The event information

starting from the detector response to the reconstruction of the physical observables are collected in so called "data-tiers". The main data-tiers regarding the flow of data of CMS can be summarized as RAW, DIGI, RECO, AOD, and MINIAOD for real data and GEN, SIM, DIGI for the MC simulation. The content of different data tiers is illustrated in Figure 3.15.

- RAW: This tier is the first data format that is collected by the CMS detector. This contains all detector signals and the trigger information. The rest of the chain for physics object reconstruction is based on the RAW data.
- DIGI: This tier is made up of the raw data collected by the detector which is converted to digital signals.
- RECO: This tier consists of all objects from reconstruction step, the step which produces high level physics objects such as leptons and jets. Hence this tier contains reconstructed physics objects for analysis purposes.
- AOD: This tier is a data-tier that is a slimmed version of RECO data to provide data for multiple analysis purposes. The AOD files contain less objects than the RECO tier, which is sufficient for most of the physics analyses.
- GEN: This tier contains information of the generated Monte Carlo event at particle level an Matrix-Element level, before being passed through the detector simulation step.
- SIM: This tier contains the energy depositions of detector simulation results for the generated particles as an outcome of GEANT-4 program.
- DIGI (MC): This tier is the converted version of SIM information as if it was collected by the CMS experiment. The reconstruction of MC events follow the same procedure as the data based on DIGI events.
- MINIAOD: is a new format [81] implemented for Run II, containing objects produced by CMS Physics Analysis Toolkit (PAT) [82]. It is designed to contain physics objects needed for most of the analyses.

The event data files for data an MC samples are stored in ROOT [83] file format. The high level physics objects are kept in collections depending on their type. The phys-

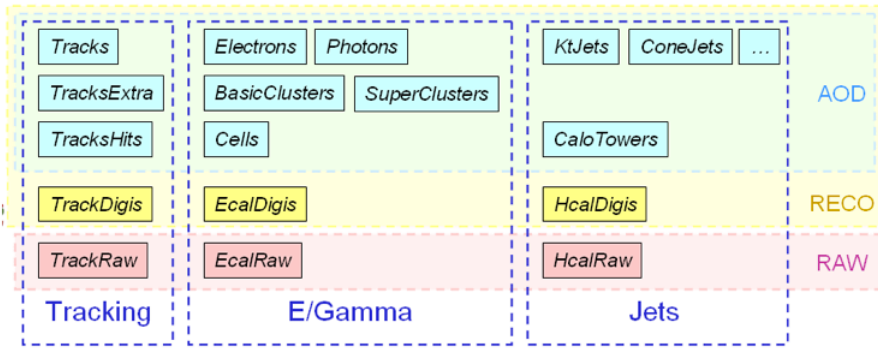


Figure 3.15: Content of different Data Tier files for some objects [79].

ical objects are kept under the Candidate collection, and each collection of objects (electrons, muons) have reference to the related objects (Tracker, Calorimeter, Muon system information).

## CHAPTER 4

### DATA ANALYSIS

The analysis studies are discussed in detail in this chapter, where special emphasis is given in the details of the reconstruction of the signals and extraction of physics results. Obtained final results are also discussed here.

#### 4.1 Analysis Outline

In this section, analyses carried out with CMS Run I and Run II data are given, for which the theoretical aspects and the experimental apparatus are described in the previous chapters. First analysis is the study of multi-differential cross section of Z + jet production, and the latter is the measurement of Underlying Event (UE) observables within  $t\bar{t}$  events. The Z bosons are reconstructed from opposite sign di-leptons (electrons or muons), and the  $t\bar{t}$  events are reconstructed from events where one top decays to muon and the other hadronically.

With the given amount of data of 2012, there are  $\sim 1.5$  Million Z + 1 jet events, which gives enough statistical precision for multiple cross section measurements to be carried on. The measurements presented in this section covers several kinematic regions in Z and jet rapidity, and hence provides stringent test of perturbative QCD predictions.

LHC Run-II measurements at ultimate precision require improved modeling and dedicated measurements of top quark events. Underlying Event is an important ingredient to the modeling, and it is important to verify and improve the "tunes" that describe the

UE. In this measurement presented in this chapter, the study of UE variables, which are properties of charged particles accompanying  $t\bar{t}$ , are studied with the 13 TeV data collected in 2015.  $t\bar{t}$  is reconstructed from single muon and jet final state. Top quarks are dominantly decaying into a W boson and a b quark. In the process of interest, one of the W bosons is decaying to a lepton and a neutrino, and the other to quark-antiquark pair. Hence, the final state of interest, discussed in detail in this chapter, consists of a well isolated lepton, four jets originated from the quarks two of which are "b-tagged", and a large missing  $E_T$ , or  $E_T^{\text{miss}}$ , due to presence of a neutrino from W decay.

In the first part of this chapter, object definitions and the selection criteria applied in both analyses are given. Then, Z+jet multi-dimensional measurement results are shown, and finally the results are given for the UE study.

## 4.2 Object Definitions and Selection Criteria

Signal events in collision data are identified through a series of trigger and identification selections. The reconstruction of physics objects and the description of the selection criteria applied is given. Z+jet analysis is carried out in di-lepton channel, where for the UE analysis  $t\bar{t}$  is selected from single-muon final-state.

### 4.2.1 Leptons

Both analyses strongly rely on the cleanest reconstruction and identification of leptons. The first selection of events is based on lepton selection, which cleans most of the QCD background. The main challenges of lepton reconstruction are; having high reconstruction and selection efficiencies where mis-identification is suppressed, obtaining perfect momentum resolution, and minimising related systematic uncertainties. In this section, the selection of events with one or two leptons is discussed including steps from trigger level to offline object identification and selection criteria.

#### 4.2.1.1 Trigger

As described in the previous chapter, the first level (L1) of the CMS trigger system, composed of custom hardware processors, is designed to select events of interest (in less than few  $\mu\text{s}$ ) using information from the calorimeters and muon detectors. The High Level Trigger (HLT) processor farm further decreases the event rate from maximum 100 kHz to 2 kHz maximum, before data storage.

The rates of various triggers were prescaled since the instantaneous luminosity increased throughout the 2012 and 2015 runs. Only unprescaled triggers were used in the presented measurements.

For the Z + jet study, events are selected if they passed any of the di-lepton (pair of oppositely charged muons or electrons) triggers. At HLT stage, the double leptons are required to have the certain transverse energy  $E_T$ . The threshold for double leptons are 17 GeV for the leading lepton and 8 GeV for the second lepton. Further selection and isolation are imposed using calorimetry and tracker are added at trigger level for the double electron trigger.

For the UE study, events firing single-muon triggers are selected. Since the study is carried out using charged-particles, there are plenty of statistics, and the inclusion of the single-electron channel is not adding a value, but only increasing the background contamination. Hence, the measurement is done only in muon channel.

More details of trigger criteria used are given in Appendix A.

#### 4.2.1.2 Electron Reconstruction and Selection

CMS has a design of calorimeter and tracker to reconstruct electrons with high precision, which is important for multiple physics goals. The analysis of Z+jets rely on clean definition of leptons; muons are discussed later in this chapter.

Electrons are reconstructed using various signals from different sub-detectors, which gives a clean collection of electrons, with small misidentification probability, good resolution of the momentum and small systematic uncertainties. The reconstruction

of electrons starts in ECAL, then propagated to tracker. The energy is spread over several crystals in ECAL, mainly because of radiation happening due to the material before ECAL. 33% (86%) of electron initial energy is radiated in lowest ( $\eta \sim 0$ ) (highest ( $|\eta| \sim 1.4$ )) material budget regions. In order to reconstruct the initial electron energy, it is essential to collect the energy of radiated photons, which mainly spreads over  $\phi$  direction due to magnetic field bending the trajectory of the electron.

First, a "seed" is found, which is the crystal with highest energy deposit in a given region. Then, two different clustering algorithms are deployed, "hybrid" in EB and "multi- $5 \times 5$ " in EE regions, that finds a cluster of hits, called the super-cluster (SC). In endcap region, energy deposit in PS lying in the acceptance of the SC is also added. By deploying these algorithms, it is found on simulation that the energy recover is better than simple  $5 \times 5$  matrix around the highest energy deposit [84].

Then, tracker information enters the game. Again, due to large radiative losses, the standard track reconstruction is not efficient, hence special procedure is used for electrons. The procedure starts with finding "seeds" again, using two approaches; one starting from ECAL SC's and the other starting from inner tracker going outwards towards ECAL SC's. Electron tracks are finally reconstructed applying a Gaussian Sum Filter (GSF) fit to determine the track parameters of the collected hits.

As noted earlier, electrons are only used in Z+jet study and combined to the measurements from the di-muon channel. For that, electrons are selected from the central region ( $|\eta| < 2.4$ ) except a pseudorapidity ( $\eta$ ) gap between ECAL Barrel and Endcap ( $1.4442 < |\eta| < 1.566$ ). Electron candidates are required to have transverse momentum ( $p_T$ ) larger than 20 GeV.

Electron Physics Object Group of CMS (POG) defined medium cut based id selection criteria are used, which corresponds to a working point of 80% identification efficiency. The electron selection criteria are summarised in Table 4.1. Particle Flow (PF) isolation cut ( $PF_{rho}^{ISO}$ ) is applied, where Effective Area ( $A_{Eff}$ ) correction is applied to correct the full neutral part as in the equation below (using  $\Delta R < 0.3$ ).

$$PF_{rho}^{ISO} = ch_{Iso}^{03} + \max(0.0, nh_{Iso}^{03} + ph_{Iso}^{03} - \rho' * A_{Eff})/p_T^e; \quad (4.1)$$



where  $ch_{Iso}^{03}$  is sum of the charged hadrons,  $nh_{Iso}^{03}$  is sum of the neutral hadrons and  $ph_{Iso}^{03}$  is the sum of photons in the cone size of  $\Delta R = 0.3$  around the electron. The electron selection criteria are summarised in Table 4.1.

Table 4.1: Electron selections used in this analysis. More details can be found in [1].

Selection		
$p_T^e > 20 \text{ GeV}$ $ \eta_e  < 2.4$ Opposite Charge Di-electrons		
vertex fit probability $< 10^{-6}$ nhits $\leq 1$		
$PF_{rho}^{ISO} < 0.15$		
Variable	Barrel	Endcap
$d\eta_{IN}$	$< 0.004$	$< 0.007$
$d\phi_{IN}$	$< 0.06$	$< 0.03$
$\sigma_{i\eta i\eta}$	$< 0.01$	$< 0.03$
$H/E$	$< 0.12$	$< 0.10$
$d0_{vtx}$	$< 0.02$	$< 0.02$
$dz_{vtx}$	$< 0.1$	$< 0.1$
$ 1/E - 1/p $	$< 0.05$	$< 0.05$

#### 4.2.1.3 Muon Reconstruction and Selection

Muons are first reconstructed independently in the silicon tracker (*tracker track*) and in the muon spectrometer (*standalone-muon track*). Based on these, two reconstruction approaches are used [85]:

- *Global Muon* reconstruction (outside-in): Starting from a standalone muon in the muon system, a matching tracker track is found and a *global-muon track* is fitted combining hits from the tracker track and standalone-muon track.
- *Tracker Muon* reconstruction (inside-out): Tracker tracks (above a certain momentum threshold) are considered as possible muon candidates and are extrapolated to the muon system, taking into account the expected energy loss and the

uncertainty due to multiple scattering. If at least one muon segment (i.e. a short track stub made of DT or CSC hits) matches the extrapolated track in position, the corresponding tracker track qualifies as a *tracker-muon track*.

The muon candidates are selected from the Particle-Flow collection. Muon identification is important to reject the cosmic ray muons, to suppress hadronic punch-through and muons from decays in flight, and to guarantee a good  $p_T$  measurement. Medium identification criterion as suggested by muon POG is used, both for Z+jet and UE analyses. The particle flow based combined relative particle flow isolation (PFIso-Corr) is defined by

$$PFIsoCorr = \frac{[\sum^{Chhad} p_T + \max(0., \sum^{Nhad} p_T + \sum^{EM} p_T - 0.5 \sum^{PU} p_T)]}{p_T^\mu} \leq 0.2, \quad (4.2)$$

where the sum of charged hadrons (Ch had), neutral hadrons (N had), photons (EM), and charged particles from the pileup (PU) in cone of  $\Delta R = 0.4$  and the factor 0.5 corresponds to a naive average of neutral to charged particles and it has been measured in jets. This  $PFIsoCorr \leq 0.2$  is a loose cut which can be used to suppress the contamination of muons contained in jets. For Z + jet analysis, two muons are required, where the muons must have opposite charge, and both with  $p_T > 20$  GeV, and be located in the muon chamber region ( $|\eta| < 2.4$ ). For  $t\bar{t}$  reconstruction, exactly one muon is required with  $p_T > 22$  GeV, and to be located in the muon chamber region ( $|\eta| < 2.4$ ).

The selections used in the analyses are listed in Table 4.2.

#### 4.2.2 Particle Flow

CMS particle-flow (PF) algorithm [86, 87] aims to reconstruct individual particles (leptons, photons, charged and neutral hadrons) by linking tracks, ECAL clusters, and HCAL clusters. The momentum or energy of each particle is formed by using information from all sub-detectors.

The procedure starts with finding the tracks of each charged particle. Then, the tracks

Table4.2: Muon selections used in this analysis.

Selection
$p_T^\mu > 20 \text{ GeV (22 GeV)}$ $ \eta_\mu  < 2.4$
recoMu.isGlobalMuon() & recoMu.isPFMuon() Number of Pixel Hits $> 0$ Number of Muon Hits $> 0$ Number of Muon Stations $> 1$ Normalized $\chi^2 < 10$ $ d_{xy}  < 0.2 \text{ cm}$ $ d_x  < 0.5 \text{ cm}$ Number of tracker layer with hits $> 5$ PFIsoCorr $\leq 0.2$

are linked to the energy clusters in the calorimeters.

#### 4.2.2.1 Vertex and Track Reconstruction

The success of PF reconstruction relies mostly on efficient reconstruction of tracks [88]. Wide scale of CMS physics goals require good resolution in high energy objects up to 1 TeV transverse momentum, and on the other hand as low as 150 MeV. Typical energy of the particles in a jet with transverse momentum of  $\sim 30 \text{ GeV}$  can be as low as 150 MeV. The CMS tracker described in detail in Chapter 2 is designed to fulfil these needs.

CMS track finding algorithm works as follows. Firstly, "hits" in tracker layers are found with local reconstruction, and are connected using Combinatorial Track Finder to form tracks. Then, the tracks are used to reconstruct the primary vertices.

#### 4.2.2.2 PF Object Reconstruction

As discussed in Section 4.2.1.2, for electrons the track finding needs a special treatment due to high Bremsstrahlung radiation, and the muons are reconstructed as described in Section 4.2.1.3. The algorithm runs as follows. Once the tracks are reconstructed, they are matched to calorimeter signals, by extrapolating the tracks through the calorimeters. Tracks that were linked to isolated muons and electrons are discarded from this process, hence firstly, the charged-hadrons are reconstructed. The clusters reconstructed by clustering algorithm in calorimeters, which is capable of distinguishing overlapping clusters, is matched to the tracks if they lie in the vicinity of the track. Then, remaining calorimeter clusters that are not matched to tracks are either assigned as neutral hadrons if the cluster is in HCAL or as photons if the cluster is in ECAL. The calorimeter and track information is combined for the charged candidates to construct the four-momentum. If the calorimeter energy is exceeding the track momentum, the difference is said to be from another neutral particle overlapping with the charged particle.

The PF algorithm improves greatly the jet response. It also improves the reconstruction of tau leptons, which is out of scope for this thesis.

#### 4.2.2.3 Charged Particle Selection Criteria

To study the UE, the properties of charged particles are studied. To achieve this, charged particle flow candidate particles are used. The following selections are applied on the charged PF candidates, where  $d_0$  and  $d_z$  corresponds to impact parameters projected on  $x - y$  plane and  $z$  axis respectively, whereas  $S_{d_0}$  and  $S_{d_z}$  are the corresponding significances.

- $p_T > 500 \text{ MeV}$ ,  $|\eta| < 2.1$ ;
- $d_0 < 3 \text{ cm}$ ,  $d_z < 1 \text{ cm}$ ,  $S_{d_0} < 10$ ,  $S_{d_z} < 10$ ;
- Tight Primary Vertex assignment ( $fromPV() \geq 2$ );
- Remove PF constituents of 4 jets from  $t\bar{t}$  decay by  $\Delta R(PF, jetconst.) < 0.05$ ;

- Remove the muon satisfying  $\Delta R(PF, \mu) < 0.05$ .

The main challenge is to remove the extra particles coming from PU. The tight primary vertex assignment kills the PU contamination. In Figure 4.1 the average number of charged particles is shown with respect to number of primary vertices in the event. It is seen that the distribution is independent of number of primary vertices, hence proves that PU contamination is removed. The muon, as well as the particles coming from the jets that are originating from  $t\bar{t}$  decay are removed from collection of particles of interest. This is necessary to probe particles coming from the UE.

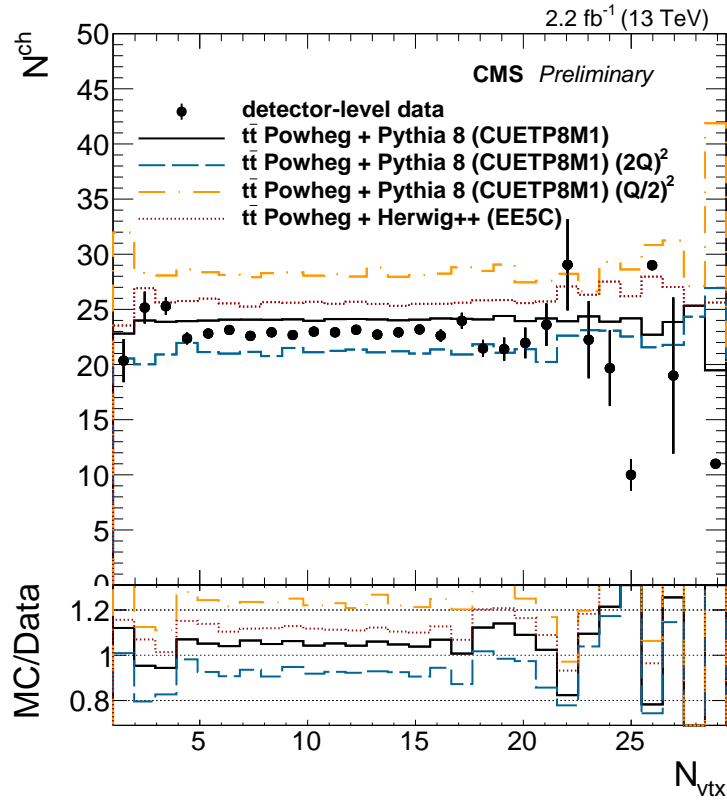


Figure 4.1: Number of charged particles versus number of vertices in data and simulation.

#### 4.2.3 Jet Reconstruction and Selection

Jets are reconstructed using the PF objects described in the previous section. Jets are clustered using the anti- $k_t$  algorithm [89] with a size parameter of  $R$  0.5 (changed to

0.4 13 TeV data).

Charged Hadron Subtraction is also used in order to ensure that jets are from same primary vertex of physics interest, by requiring  $z$  component of primary vertex to be  $z < 24 \text{ cm}$ , radius in  $x - y$  plane to be less than  $2 \text{ cm}$ , and number of degrees of freedom of vertex fit to be  $n.d.o.f. > 4$ .

Despite the success of reconstructing individual PF candidates, detector response is not linear, thus it is not easy to measure the correct energy of jets. Jet energy correction (JEC) are applied to correct  $p_T$  and to make jet response flat in pseudo-rapidity space. In data L1FastJet + L2Relative + L3Absolute + L2L3Residual, and in MC L1FastJet + L2Relative + L3Absolute are used. L1FastJet is using FastJet simulation to remove the energy coming from pile-up events. L2Relative is to make the jet response flat in all  $\eta$  regions. The uniformity in pseudo-rapidity can be achieved by applying correction to jets in any  $\eta$  relative to jets in central region ( $|\eta| < 1.3$ ). This L2Relative can be done by MC truth or by data-driven dijet balance. L3Absolute makes jet response flat in  $p_T$  space. This correction is derived from MC truth or data-driven  $Z/\gamma$ +jet balance. After L1FastJet + L2Relative + L3Absolute correction, the jet energy is approximately equal to that of generator-level jets. However, during the data taking period the current jet energy correction is not enough to compensate difference between real data and MC. By studying dijet and vector boson plus jets, new jet energy correction, L2L3Residual, is introduced to correct jets in real data on top of the normal sequences. More details about JEC can be found at [90].

The decay leptons may mix into the jet collection in the final state during event reconstruction. Leptons can intervene jets in two possible ways. First, if the energy of lepton is high enough, it might be reconstructed as a jet which increases the jet multiplicity. Second, leptons can decay into a jet cone. These leptons will add up the total energy of jets. In this study Particle-Flow framework is not used to remove decay leptons before jet clustering. These leptons are vetoed from the jet collection by a simple  $\Delta R$  cut of 0.5.

Loose identification criterion from JetMET POG is used to improve the jet quality. Jet  $p_T > 30 \text{ GeV}$  threshold is used to reject low PU jets and get a better jet energy resolution. In this study, the jet acceptance is extended to forward region covering

jets within rapidity  $|y| < 4.7$ , which lies beyond the silicon tracker acceptance, creating some further challenges. For that challenge regarding PU contamination, a new method is developed. Cut based PU identification criteria are applied to further reduce pile-up contamination. Table 4.3 summarizes the selection criteria used for jets.

Table4.3: Jet selection criteria used in this analysis.

Selection
$p_T^{jet} > 30 \text{ GeV}$ $ y_{jet}  < 4.7$
Charged Hadron Fraction $> 0$ Neutral Hadron Fraction $< 0.99$ Charged Multiplicity $> 1$
<i>(Only on jets with <math> y_{jet}  &lt; 2.4</math>)</i> Charged EM Fraction $< 0.99$ Neutral EM Fraction $< 0.99$ Number of Constituents $> 1$

#### 4.2.3.1 b-tagging

Identifying jets originating from b-quarks, named as b-tagging, is important for many physics signals. For the reconstruction of the  $t\bar{t}$  signal, it is an essential element, in order to suppress other background processes.

The neutral hadrons containing heavy quarks, when produced in the hadronisation of the hard scattering, flies a certain distance before decay chain starts. This forms a so called "Secondary Vertex" with respect to the PV. Figure 4.2 shows a sketch of SV formation, which is distinguishable, thanks to the tracker resolution. CSV algorithm is used to distinguish the b-quark jets from light jets. The algorithm runs on jets wing individual particles and builds a discriminant in range  $[0,1]$ . The value is chosen with  $> 0.89$ , which corresponds to 80% of efficiency with few % of mistag rate.

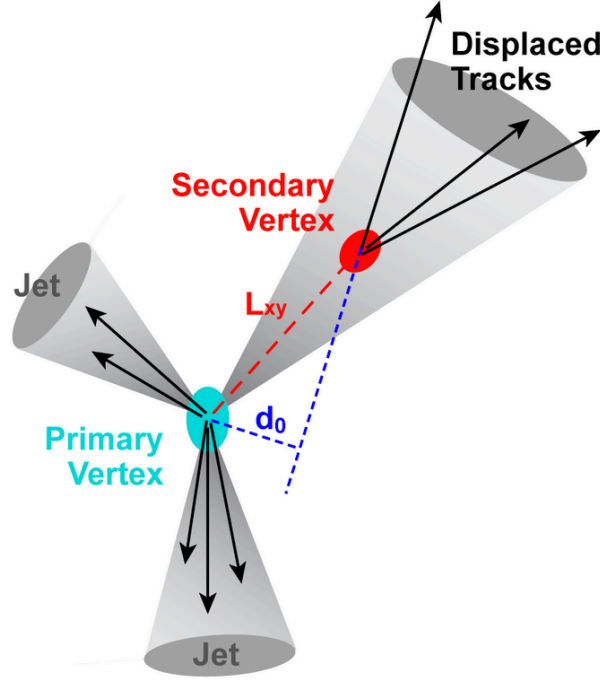


Figure 4.2: Illustration of Secondary Vertex and variables used to identify them [91].

#### 4.2.4 $E_T^{\text{miss}}$ Reconstruction and Selection

Another important variable for the  $t\bar{t}$  reconstruction is the missing transverse momentum,  $E_T^{\text{miss}}$ . The neutrinos are weakly interacting particles giving no signal in the detector. Due to momentum conservation, they manifest themselves as a missing momentum in transverse plane.  $E_T^{\text{miss}}$  is simply the negative sum of the transverse momenta of visible particles. There are several algorithms reconstructing the  $E_T^{\text{miss}}$ . The analysis uses Particle-Flow based  $E_T^{\text{miss}}$ , as many other CMS analyses. The  $E_T^{\text{miss}}$  is the negative of sum of all particles reconstructed using PF algorithm.

### 4.3 Pile-Up Reweighting Technique

In the MC production an approximate distribution of pile-up interactions is assumed. However, this assumption does not match the conditions for each data-taking period. Also, the final distribution for the number of reconstructed primary vertices is still sensitive to the details of the primary vertex reconstruction, the differences in the underlying event in data vs Monte Carlo and there is a bias caused by the offline event



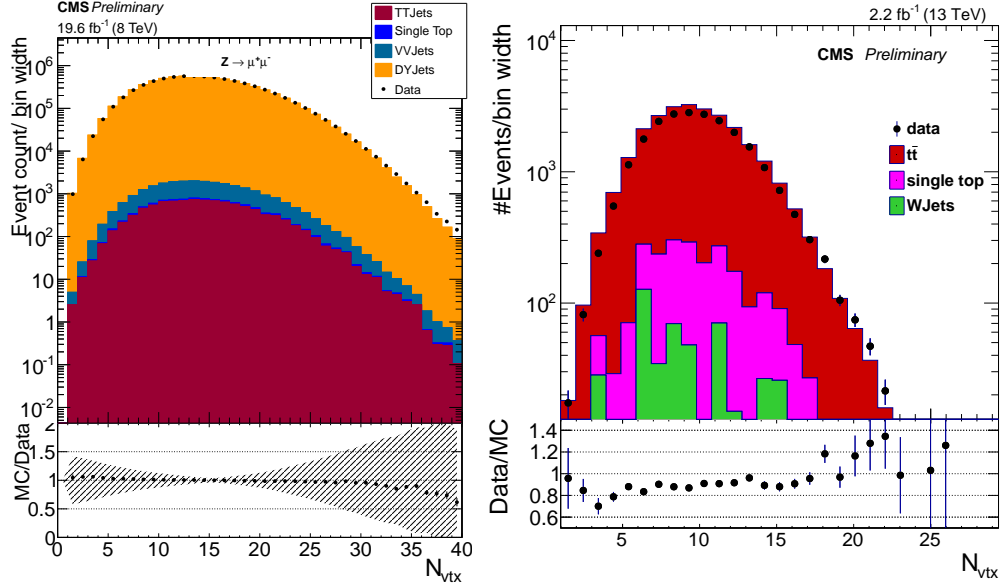


Figure 4.3: Number of vertex distribution in data and simulation sets, compared after pile-up reweighting technique is performed.

selection criteria and even by the trigger. In order to correct these effects, the number of simulated pileup interactions in MC are reweighted by the data pileup distribution using the entire data-taking period. The official pile-up re-weighting procedure is described in [92]. Number of vertex distributions from Z+jet and  $t\bar{t}$  analyses are shown, after the reweighting in Fig 4.3, and it is observed that the PU reweighting technique works well in removing discrepancies.

#### 4.4 Efficiency Corrections

In order to measure particle reconstruction efficiencies from the data without relying on the efficiency predictions from MC, a data-driven approach to measure particle efficiencies called "Tag and Probe" method is utilised. This method uses the known di-object resonances such as Z or  $J/\psi$ . The "Tag and Probe" method requires one object to satisfy tight requirements ("tag" object) while the other object is required to satisfy the loose requirements ("probe" object). Invariant mass (in this case Z from muons and electrons) is calculated with this pair of objects.

In this analysis, the scale factors are used to compensate the differences between data

and MC efficiencies. The efficiencies of data and MC are calculated and found the scale factor, ratio between data and MC efficiencies. ID and isolation are provided as a function of  $p_T$  and  $|\eta|$  while trigger efficiency (trigger efficiencies are for muons only) is given as a function of  $|\eta|$ .

For the Z + jet analysis, the values of selection and identification efficiencies are  $\sim 58\%$  ( $\sim 88\%$ ) for electron (muon) channels.

#### 4.5 Background Determination and Subtraction

In the final state of interest, there are other processes apart from the one of interest, which creates so called "background".

For the Z + jet reconstruction, the di-lepton pairs are assumed to be coming from the decaying Z boson. Any other processes with two leptons in final state would "mimic" the Z boson. The process with the highest contribution is from di-boson decaying into at least two charged leptons. The other dominant background is  $t\bar{t}$  where both top quarks decay leptonically. The Z bosons decaying into pairs of  $\tau$  leptons is also a background. The  $\tau$  lepton decay into muon or electron and two neutrinos and can mimic the same final state. These events are treated within the unfolding machinery the same way as the "fakes". Other backgrounds are estimated from MC samples and subtracted from data before unfolding. The cross sections used are summarised in Table 4.4. Other backgrounds, such as W+jet with W decaying to a charged lepton and a neutrino, a jet can be mis-identified as a lepton and mimic the same final state. However, this is highly suppressed by the good isolation criteria of leptons. The same discussion holds for QCD processes of multijets where two jets are faking leptons.

For the  $t\bar{t}$  analysis, the signal is reconstructed in lepton + jet channel. The main background for this is W+jets, but this is highly suppressed by requiring two b-tagged jets. The same discussion for QCD in Z+jet is valid for  $t\bar{t}$ . The measurement involves only studying charged particle properties, and the effect of backgrounds are negligible. The effect is tested and found to be less than 0.1 %.

Table4.4: Monte Carlo Samples.

Dataset name	x-sec (pb) $\times$ BR
Z+jet	3531.8
$t\bar{t}$	245
$ZZ \rightarrow 2l\ 2q$	$17.654 \times 0.14$
$ZZ \rightarrow 2l\ 2\nu$	$17.654 \times 0.04$
$ZZ \rightarrow 4l$	$17.654 \times 0.01$
$WZ \rightarrow 2l\ 2q$	$33.21 \times 0.07$
$WZ \rightarrow 3l\ \nu$	$33.21 \times 0.03$
$WW \rightarrow 2l\ 2\nu$	$54.838 \times 0.11$
single $t$ , $t$ channel	56.4
single $\bar{t}$ , $t$ channel	30.7
single $t$ , $s$ channel	3.79
single $\bar{t}$ , $s$ channel	1.76
single $t$ ( $\bar{t}$ ), $tW$ channel	11.1

#### 4.6 Correction for Detector Effects

To be able to compare the measurements to the results of other experiments, and to theoretical predictions, it is necessary to eliminate the detector effects. Complications arise when a measured value is subject to random fluctuations caused by detector effects. Each observation is then characterized by a true (and unknown) value  $t$  that is smeared by detector effects and becomes a measured value  $m$ . In general, one can simply smear the prediction to include the distortions of the detector. However, the measurement cannot be subsequently compared with the results of other experiments because the smearing is detector dependent. Therefore, the measurement should be "unfolded" of detector effects. For the Z + jet analysis, the jet  $p_T$  and  $y$  resolution may have a large effect and thus the angular distribution measurement may need to be unfolded.

The continuous distributions for  $t$  and  $m$  are related by a convolution [93]. For a measured distribution  $f_{meas}$ , the true distribution is defined by  $f_{true}$

$$f_{meas}(m) = \int R(m|t) f_{true}(t) dt \quad (4.3)$$

where  $R$  is called the response function and depends only on the measuring apparatus. For a measurement binned into a histogram, Eq. 4.3 becomes

$$m_i = \sum_{j=1}^N R_{i,j} t_j \quad (4.4)$$

where  $N$  is the total number of bins. The response matrix then has the simple interpretation of a conditional probability:  $R_{i,j}$  is the probability that an observed value in bin  $i$  corresponds to a true value in bin  $j$ .

To obtain the true distribution, one may intuitively invert the response matrix such that

$$\mathbf{t} = R^{-1} \mathbf{m} \quad (4.5)$$

where  $\mathbf{t}$  and  $\mathbf{m}$  are vectors of the true and measured values, respectively. However, unfolding techniques perform more complicated inversions (discussed in [93]) in order to minimize statistical fluctuations. The unfolding procedure in the analysis was performed with the RooUnfold package [94]. The RooUnfold package provides a common framework to evaluate various unfolding algorithms, providing implementations for the Iterative, Singular Value Decomposition, and TUnfold methods, as well as bin-by-bin correction factor and unregularized matrix inversion methods.

## 4.7 Z + jet Study

The signature of a Z boson decay is the presence of a high  $p_T$  isolated lepton pair (either a pair of electrons or a pair of muons). Selected events are required to have a pair of leptons with an invariant mass window of 40 GeV around the known Z mass. Particle-Flow jets are selected using the infrared and collinear safe anti- $k_t$  clustering algorithm requiring  $p_T > 30$  GeV and be in the calorimeter acceptance of  $|y| < 4.7$ . All the distributions are corrected for the efficiency of the trigger, selection, reconstruction and isolation. They are calculated by a Tag and Probe method as previously described. The results are shown after applying the unfolding procedure to

Table 4.5: Number of events reconstructed in data and Monte-Carlo in each  $N_{jet}$  bin in muon channel.

bin	0	1	2	3	4	5	6	7
ZZJets4L	145.01	173.075	124.226	33.786	7.98397	1.7078	0.308267	0.0472352
Single Top	139.733	431.892	207.586	62.4945	9.73418	1.46731	1.35701	0
ZZJets2L2Nu	1243.45	350.323	94.4457	20.9614	4.04434	0.643819	0.184974	0.00872009
ZZJets2L2Q	773.762	2212.12	1911.12	542.656	138.264	28.2506	5.72645	0.859881
WWJets2L2Nu	1179.11	385.796	114.332	24.4228	4.69081	0.461405	0	0
WZJets2L2Q	756.34	1470.67	1266.21	554.554	178.002	41.8406	8.8393	1.33613
WZJets3LNU	789.442	891.859	366.658	94.6252	21.982	3.68267	0.878225	0.095663
TTJets	344.959	2245.2	4154.26	1933.88	600.913	152.084	36.4671	10.3353
DY+jets	6.2698e+06	967632	190223	34113.4	6095.42	967.309	155.601	20.8243
TOTAL	6.27517e+06	975793	198462	37380.7	7061.03	1197.45	209.363	33.5072
DATA	6.26771e+06	970556	197542	37921	7173.77	1382.24	241.256	35.9628
Ratio	1.00119	1.0054	1.00466	0.985754	0.984285	0.866307	0.867803	0.931718

deconvolve the distributions from detector effects. Results from muon and electron channel separately, compared at detector level with the theoretical prediction are also discussed.

#### 4.7.1 Z Boson Reconstruction

Z bosons are reconstructed from the selected opposite charged di-lepton events with the criteria explained in previous sections. The events lying in the Z mass window of  $71 < M(Z) < 111$  GeV are used for the analysis. In Figure 4.4 the invariant mass of di-lepton pairs is shown for electron and muon channels. The jet rapidity, extended to 4.7, is shown in Figure 4.6 in both channels. It is seen that the data is well described by the MC. The distribution of number of jets produced with the Z boson, up to 7 jets, is shown in Figure 4.5 and the number of events are given in Table 4.5. Figure 4.7 shows the rapidity distribution of di-lepton pairs, where in Figure 4.8 the leading jet  $p_T$  distribution is given.

The measurement focuses on three main variables:  $p_T(j_1)$ ,  $y(Z)$ , and  $y(j_1)$ , that describe the kinematics of the events. Three different multidimensional cross sections measurements using these variables have been carried out:

- $d^2\sigma/dp_T(j_1)dy(j_1)$

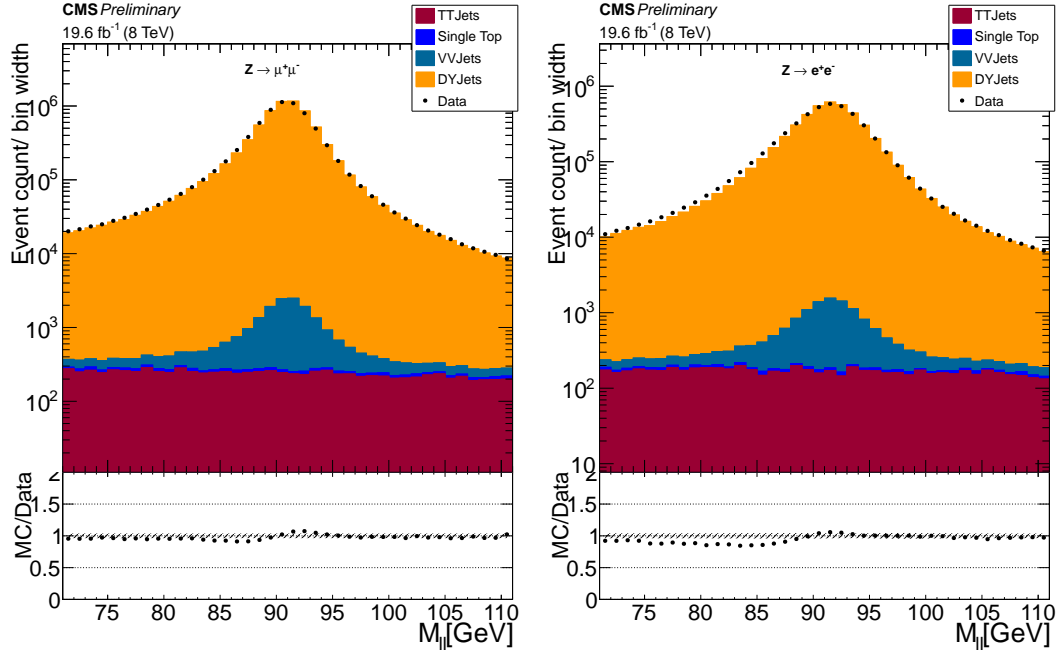


Figure 4.4: Detector level di-lepton invariant mass, from di-muon and di-electron channels, compared with simulation sets.

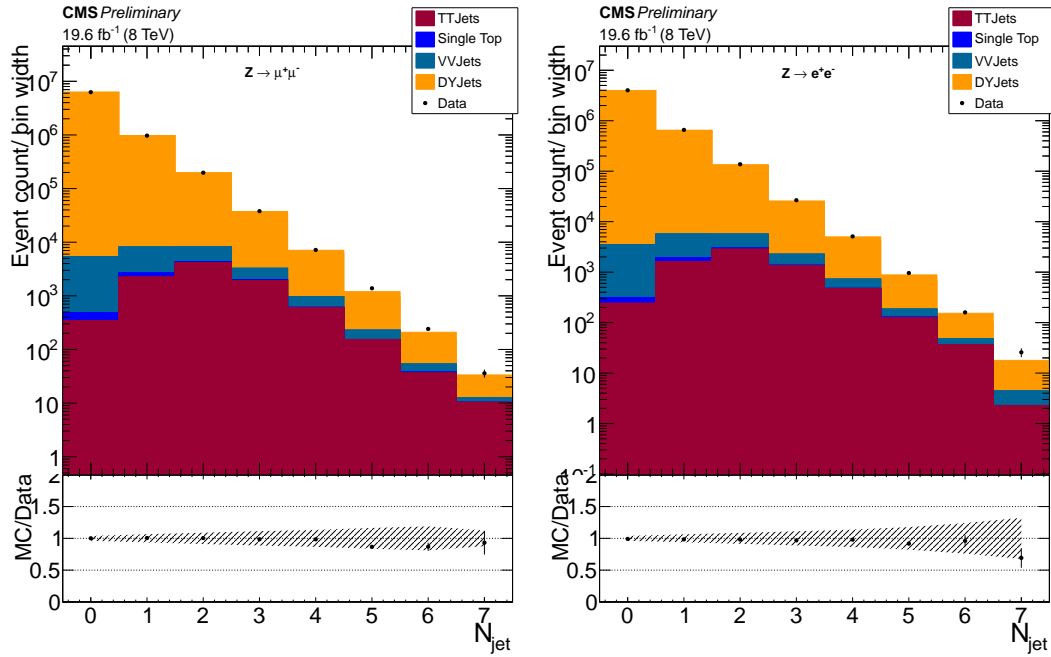


Figure 4.5: Detector level jet multiplicity, from di-muon and di-electron channels, compared with simulation sets.

- $d^2\sigma/dy(Z)dy(j_1)$
- $d^3\sigma/dp_T(j_1)dy(j_1)dy(Z)$

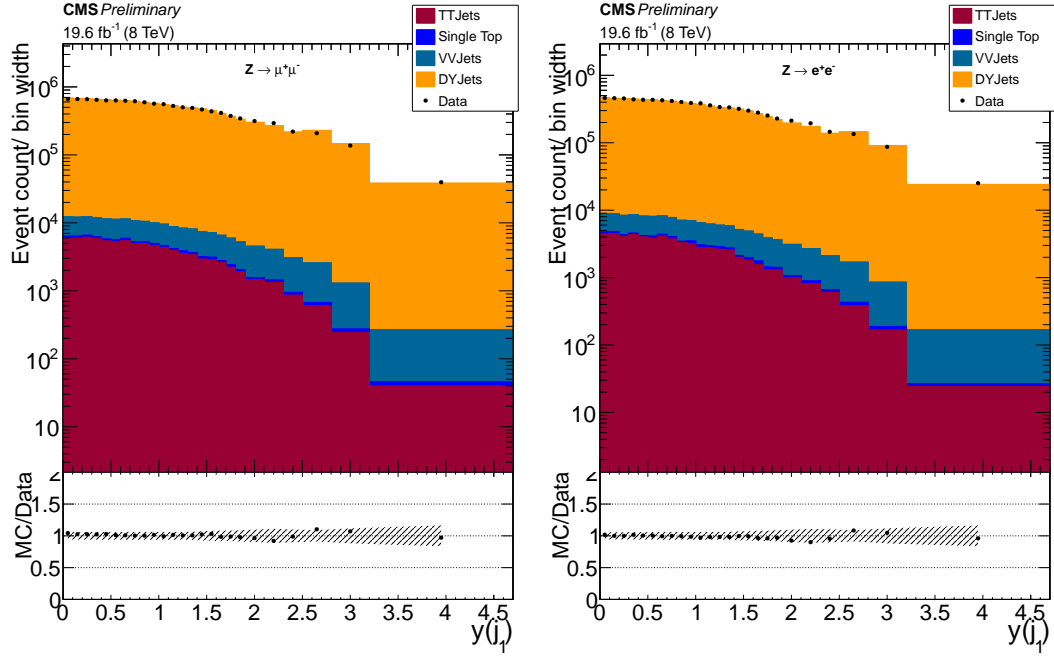


Figure 4.6: Detector level rapidity of the jet with highest transverse momentum, from di-muon and di-electron channels, compared with simulation sets.

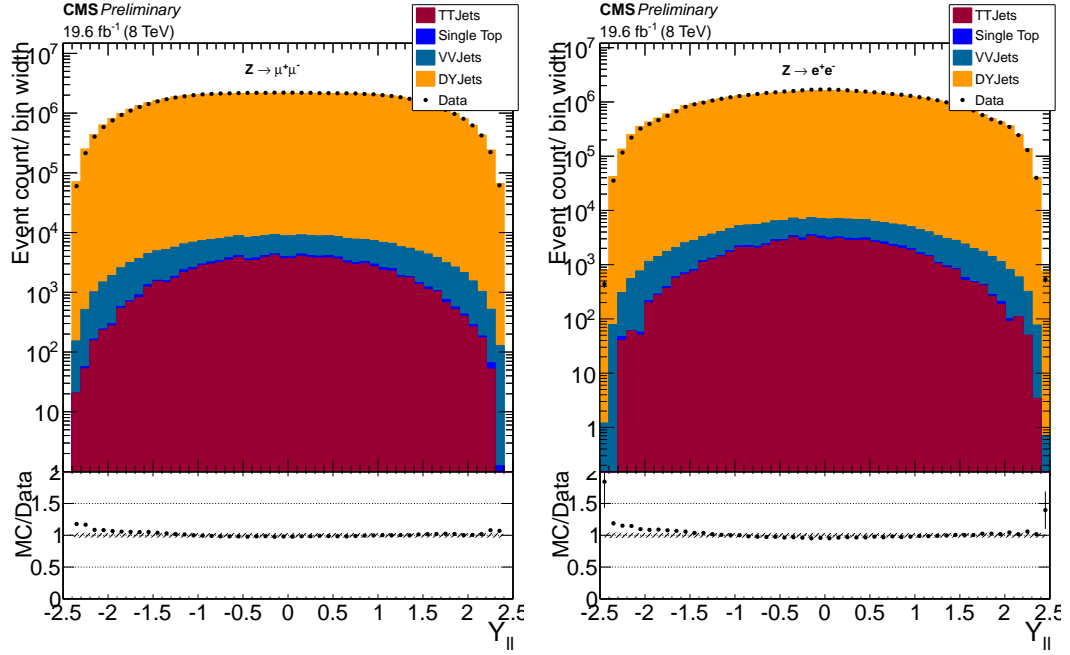


Figure 4.7: Detector level rapidity of the Z boson reconstructed from di-muon and di-electron pairs, compared with simulation sets.

The symmetry with respect to the transverse plane  $y = 0$  is used to minimise the statistical uncertainties by taking the absolute value of rapidities, such that the differential cross section  $d^2\sigma/dp_T(j_1)dy(j_1)$  is estimated from a two-dimensional histogram

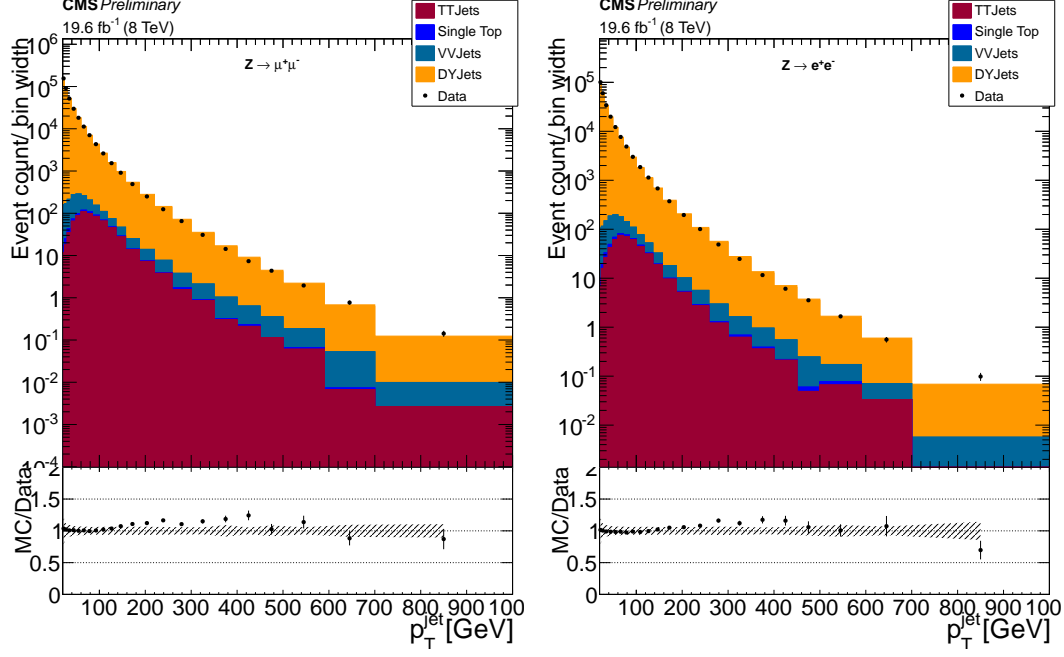


Figure 4.8: Detector level transverse momentum of the leading jets, from di-muon and di-electron channels, compared with simulation sets.

of  $(p_T, |y(j_1)|)$  and the differential cross section  $d^2\sigma/dy(Z)dy(j_1)$  from a histogram of  $(|y(j_1)|, |y(Z)|\text{sign}(y(Z)y(j_1)))$ . Here,  $\text{sign}(x) = 1$  for  $x \geq 0$  and  $\text{sign}(x) = -1$ , for  $x < 0$ , is used to distinguish same- and opposite-sign configurations of  $Z$  and jet. The three-dimensional differential cross section is calculated similarly.

## 4.7.2 Unfolding Details

The details of the unfolding procedure is described in this section. In this analysis, Bayesian iterative D'Agostini method [95] is used within RooUnfold framework. One dimensional unfolding is carried out for each range, in each measurement channel separately. The phase space definition at generator level and the response matrices of each range is given in the subsections below.

### 4.7.2.1 Generator Level Phase-space

The measurement is carried out in the "fiducial" volume, implementing selection criteria also at the generator level. Generator level  $Z$  bosons are reconstructed from final



products, in order to mimic the detector level selections.

To achieve this, "status-1" particles of PYTHIA 6 is used. The di-lepton pairs are chosen with  $p_T$  greater than 20 GeV and  $|\eta| < 2.4$ . Here, the leptons are "dressed"; the photons in a cone of  $\Delta R < 0.1$  to the lepton is added to it. This ensures to recover the effects of QED FSR and to approach closer to the true Z kinematics. The lepton pairs with invariant mass in the Z mass window of  $71 < M(Z) < 111$  GeV are used. The generator level jets are reconstructed using "stable" particles excluding neutrinos, using anti- $k_t$  algorithm with distance parameter of 0.5. The jets are required to have  $p_T$  greater than 30 GeV and  $|y| < 4.7$ .

#### 4.7.2.2 Response Matrices

The response matrices are given in Figure 4.9 for the di-muon channel. For each measurement, one dimensional unfolding is carried out. The variable that is to be unfolded is chosen to be the variable with highest bin migrations. As seen in Figure 4.9 the  $p_T$  distribution has  $\sim 60\%$  of events in diagonal, the jet rapidity  $\sim 90\%$  and the Z rapidity  $\sim 98\%$ . Hence, for the jets generated in bin  $i$  is 60% reconstructed in the same bin, where 40% of the cases it is migrated to other bins. Hence for the measurements of  $d^2\sigma/dp_T(j_1)dy(j_1)$  and  $d^3\sigma/dp_T(j_1)dy(j_1)dy(Z)$ , the unfolding is carried out with respect to  $dp_T(j_1)$ . For  $d^2\sigma/dy(Z)dy(j_1)$  measurement, the unfolding is carried out with respect to  $dy(j_1)$

The number of iterations are set to be the optimal value for each range, such that the  $\chi^2$  of change is greater than and closest to one. The unfolding machinery and the choice of number of iterations have been tested against any possible bias on the results. Further discussions can be found in Appendix B.

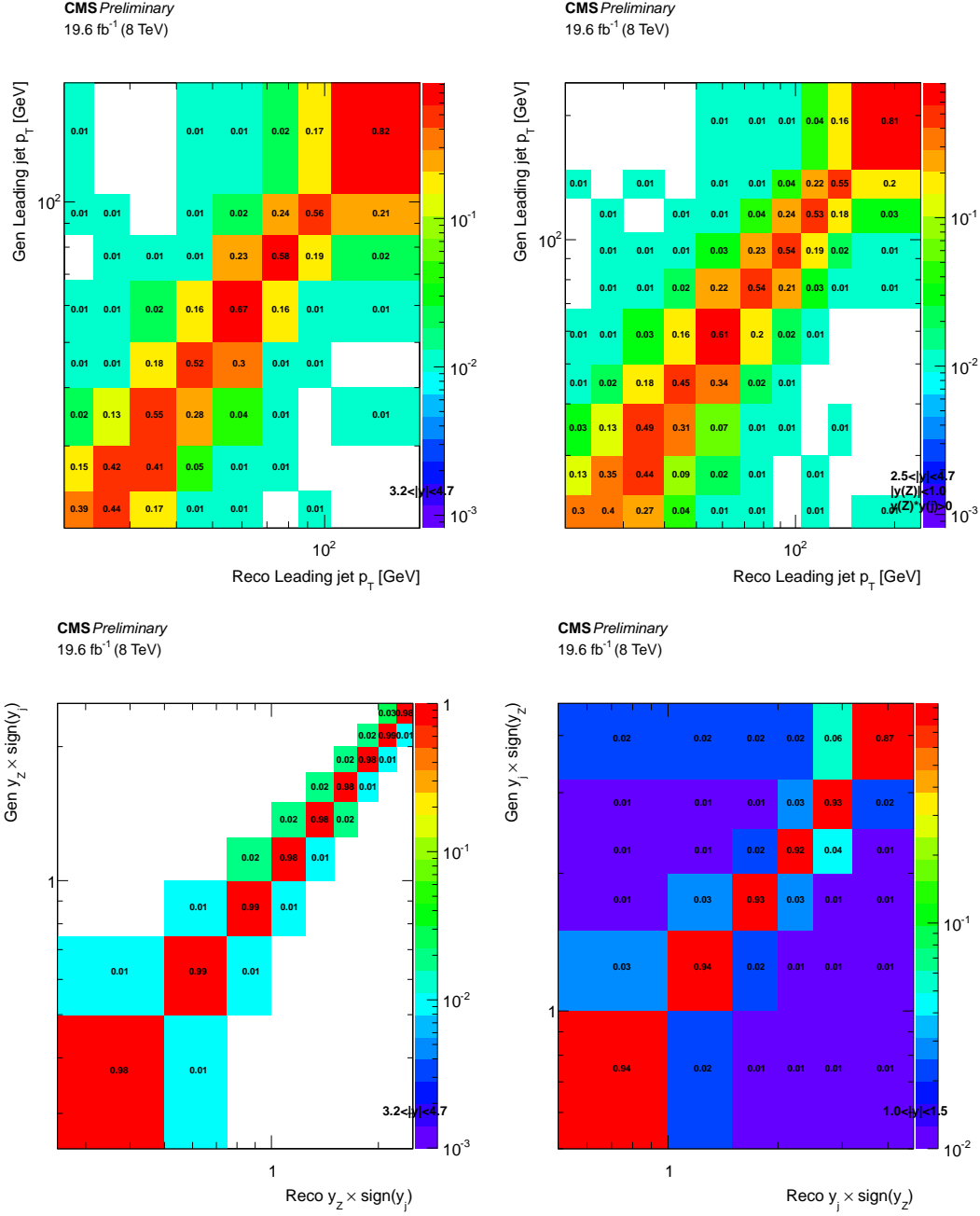


Figure 4.9: Response matrices for  $d^2\sigma/dp_T(j_1)dy(j_1)$ ,  $d^3\sigma/dp_T(j_1)dy(j_1)dy(Z)$ , and  $d^2\sigma/dy(Z)dy(j_1)$  in di-muon channel.

### 4.7.3 Residual PU removal in the forward region

In the forward region with low  $p_T$  a discrepancy is observed which is not covered by the experimental uncertainties. In Figures 4.10 and 4.11 the azimuthal angle difference between the Z boson and the leading jet ( $\Delta\phi(Z,j)$ ) distributions are shown on MC sample. The inclusive distributions are compared with the distributions for the jets that are matched to gen jets with ( $\Delta R < 0.5$ ). It is observed that there is a big contamination in the forward regions from the "not-matched" jets, which are mainly PU jets.

The rejection of jets originating from pileup is more difficult outside the tracker geometric acceptance, since the vertex constraint cannot be used to reject the charged particles coming from pileup. Therefore, despite the jet pileup rejection criterion, which are "extrapolated" from the tracker region to forward, a contamination of jets from pileup remains, and needs to be subtracted. This region beyond the tracker acceptance,  $2.5 < |y| < 4.7$ , is used only for  $Z + \geq 1$  jet multidimensional differential cross section measurements, where only the leading jet is relevant.

The fraction of events in which the leading jet comes from a pileup event, denoted as  $f_{PU}$ , is estimated using a control sample of a Z boson produced with one jet exclusively. This is obtained by requiring exactly one jet with  $p_T$  above 30 GeV. On top of this, any other jet activity is vetoed by requiring no other jets with  $p_T$  above 20% of the Z boson transverse momentum. All jets with  $p_T > 12$  GeV are considered for this ratio veto. As Z boson and a jet coming from two different pp collisions are independent, the distribution of the  $\Delta\phi(Z,j)$  is expected to be flat, which is confirmed by the simulation. For the Z boson and the jet of a  $pp \rightarrow Z + 1$  jet event the distribution is expected to peak at  $\pi$  due to momentum conservation. The veto on additional jets enforces the  $p_T$  balance between the Z boson and the jet, reducing the signal presence in low values of  $\Delta\phi(Z,j)$ . It has been checked on the simulation that this contribution is negligible in the region  $\Delta\phi(Z,j) < 1$ , as shown in Figures Therefore,  $f_{PU}$  is estimated from the fraction of events in that region, which purely contains the PU jets.

To clean this residual PU contamination, a method described in this section is applied. The method uses ( $\Delta\phi(Z,j)$ ) as a discriminant to define PU contamination in the

signal. The fraction of pileup events estimated from the control sample is then used to correct the signal data sample. The same method is applied to the simulation. This makes the description of pileup effects in the simulation agree with data. The ratio of the value of  $f_{\text{PU}}$  obtained from the simulation to that measured in data decreases monotonically as a function of  $p_{\text{T}}$ . In the  $p_{\text{T}}$  bin 30–50 GeV it ranges up to 1.25 (1.35) for  $|y(j_1)|$  between 2.5 and 3.2 (3.2 and 4.7). Beyond  $p_{\text{T}} = 50$  GeV the discrepancy is negligible and the results are identical with or without the pileup subtraction.

The real Z+1j events are expected to peak around ( $\Delta\phi(Z, j) = \pi$ ) where the Z+PU events are expected to be flat. The PU region is defined as ( $\Delta\phi(Z, j) < 1.0$ ). ( $\Delta\phi(Z, j)$ ) is plotted for different jet  $y$  (2.5, 3.2, 4.7) and  $p_{\text{T}}$  (20, 24, 30, 40, 50, 68 GeV) bins in Data & MC. Figures 4.10- 4.11 shows the ( $\Delta\phi(Z, j)$ ) distributions for Z+1j exclusive events in the forward regions.

The fraction  $f_{\text{PU}}$  is estimated from the formula:

$$\hat{f}_{\text{PU}} = \frac{\pi N_{\Delta\phi < 1}}{N} \quad (4.6)$$

with  $N_{\Delta\phi < 1}$  the number of events with the azimuthal angle between the Z boson and the leading jet smaller than 1 and  $N$  the total number of events. The fraction  $f_{\text{PU}}$  is estimated from the fraction of events with  $\Delta\phi < 1$ ,  $\hat{f}_{\text{PU}} = \pi \cdot f_{\Delta\phi < 1}$ . The estimation is calculated as a function of jet transverse momentum and rapidity using the same binning as the one used for the measurement,  $(|y|, p_{\text{T}}) \in \{2.5, 3.2, 4.7\} \times \{20, 24, 30, 40, 50, 68 \text{ GeV}\}$ .

It is shown using the MC sets that the fraction of events whose  $p_{\text{T}}$ -leading jet comes from pileup is the same in the signal sample ( $Z + \geq 1$  jet) as in the control sample ( $Z + = 1$  jet). Each bin of the measured distribution is corrected by rescaling the number of events by  $1 - \hat{f}_{\text{PU}}$  to remove the contribution from PU jets. The estimation is calculated both on MC and data separately and applied to both. These corrections are shown in Figure 4.12. The difference observed between the real data and the simulation is taken into account in the systematics uncertainties described in the next section. By definition the fraction estimation  $\hat{f}_{\text{PU}}$  is contaminated by the signal events with small azimuthal separation between the Z boson and the  $p_{\text{T}}$ -leading jet, in particular by signal events from double parton scattering, and these events are

also removed by the method. As the corrections are applied both on MC and data, this "over-correction" is corrected back by the unfolding. For large jet transverse momentum,  $\hat{f}_{\text{PU}}$  become smaller and its value is correctly estimated by the simulation. Therefore, the  $(1 - \hat{f}_{\text{PU}})$  correction is applied only for  $p_{\text{T}}(j_1) < 70 \text{ GeV}$ , and for larger values, as for central jets, the pileup subtraction is taken into account by the unfolding.

After applying the factors, the leading jet  $p_{\text{T}}$  spectrum is compared to matched and not-matched cases. In Figure 4.13 the the leding jet  $p_{\text{T}}$  spectra are given for all y bins.

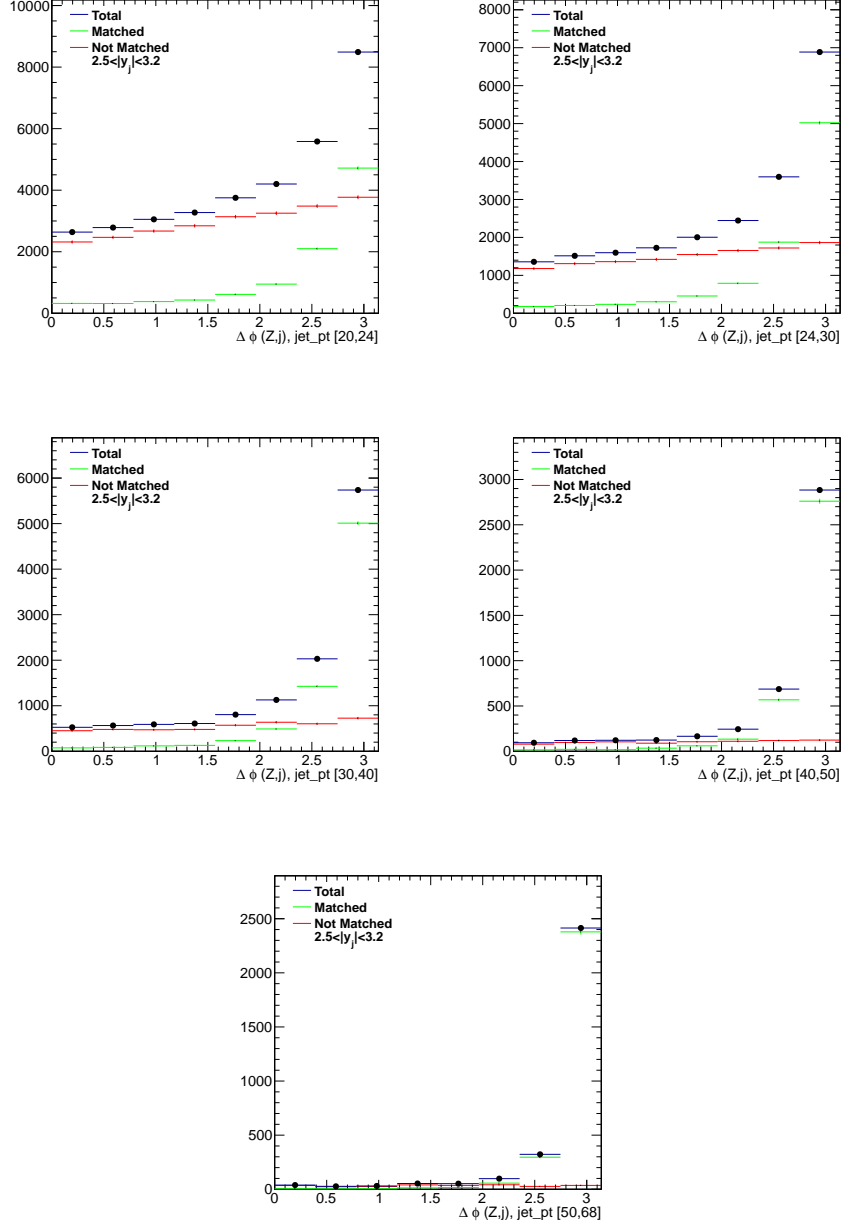


Figure 4.10: The azimuthal angle difference distributions between the Z boson and the jet ( $\Delta\phi(Z, j)$ ) for jets with  $y$  [2.5,3.2] for Z+1j exclusive events. The green (red) lines represent the jets that are matched (not-matched) to a gen jet.

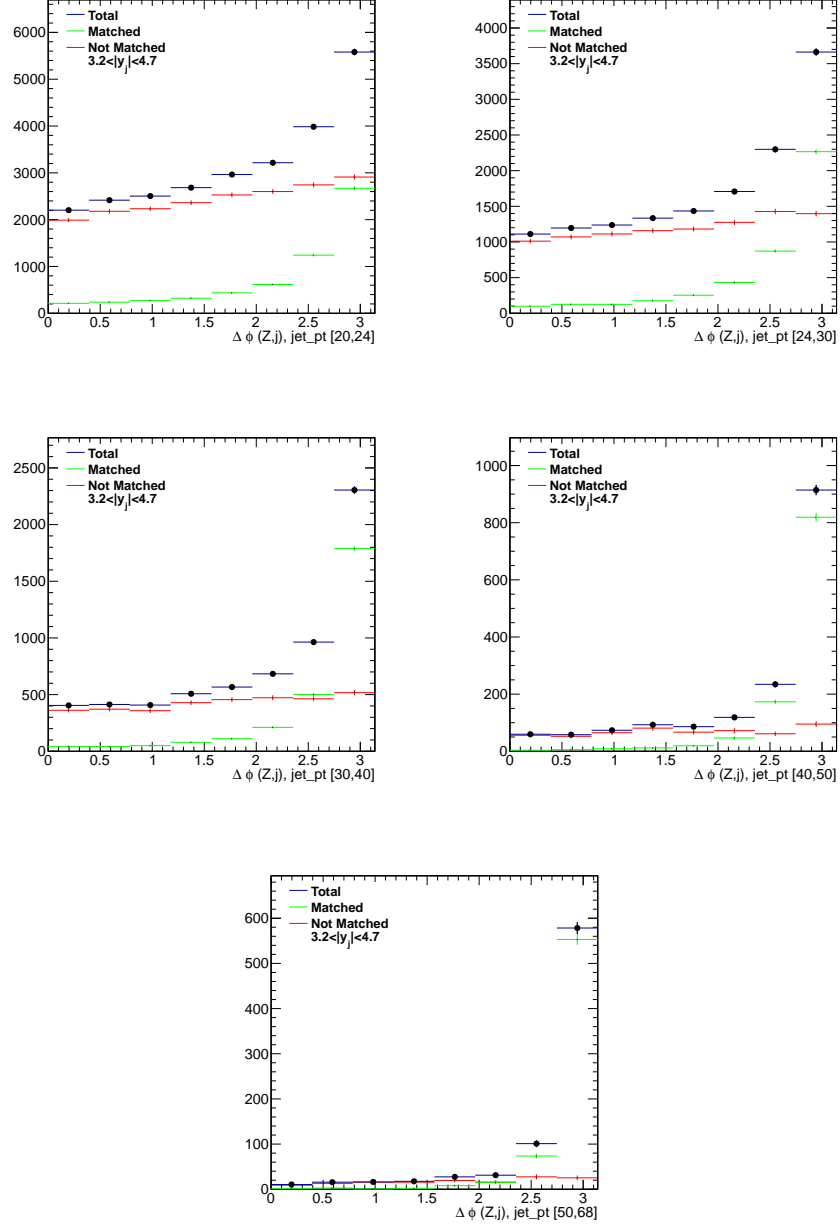


Figure 4.11: The azimuthal angle difference distributions between the Z boson and the jet ( $\Delta\phi(Z,j)$ ) for jets with  $y [3.2,4.7]$  for Z+1j exclusive events. The green (red) lines represent the jets that are matched (not-matched) to a gen jet.

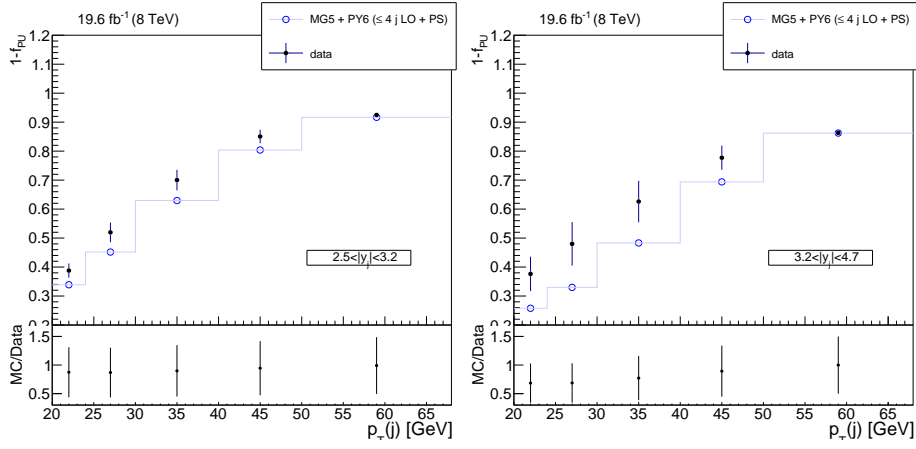


Figure 4.12: Obtained factors on Data and MC with the ratio MC/Data

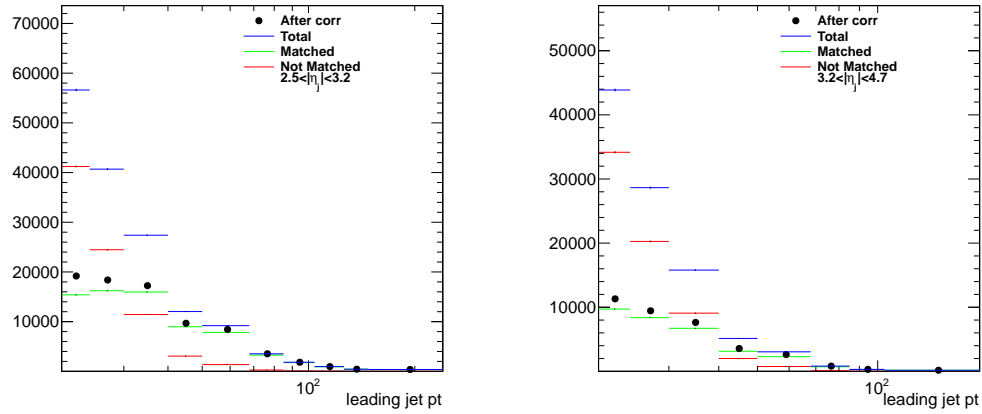


Figure 4.13: The leading jet  $p_T$  distributions on MC. The green (red) lines represent the jets that are matched (not-matched) to a gen jet.



#### 4.7.4 Systematic Uncertainties

In this section, several sources of uncertainties on the measurement taken into account are explained. Main source of experimental uncertainties are uncertainties of Jet Energy Scale and Resolution, Luminosity measurement, Pile-up, cross sections of the background processes, identification and trigger efficiency corrections of the leptons. Theoretical uncertainties originating from QCD scale and PDF's are also taken into account for MG5\_aMC sample. These uncertainties are estimated as explained in this section.

Experimental uncertainties:

Table 4.6 shows the breakdown of experimental uncertainties for  $d^2\sigma/dp_T(j_1)dy(j_1)$  measurement, first bin in jet  $y$  in the forward region.

Table4.6: Leading jet  $p_T$  (  $2.5 < |y(j_1)| < 3.2$ )

$p_T(j_1)$ range	$d^2\sigma/dp_T(j_1)dy(j_1)[pb/GeV]$	stat	JES	Lumi	JER	PU	xsec	pu subt	unf	tot
30-40	0.1521	0.3514	8.03	0.01713	0.881	1.621	0.0927	3.872	6.296	14.53
40-50	0.08394	0.4616	7.155	0.03492	1.026	1.001	0.1895	1.169	2.279	9.969
50-68	0.04135	0.5868	7.023	0.05692	1.203	0.5192	0.3029	0.8659	1.02	9.332
68-85	0.01812	0.8986	7.608	0.08077	1.085	0.06827	0.4134	1.196	1.748	10.3
85-104	0.008413	1.259	8.415	0.09875	0.9055	0.4415	0.486	0.9041	2.687	11.64
104-126	0.003788	1.714	8.39	0.1198	1.083	0.2966	0.5661	0.6735	2.5	11.66
126-148	0.001688	2.478	10.48	0.1425	1.111	0.4836	0.647	0.5171	1.771	14.07
148-240	0.0003444	3.284	9.747	0.1498	1.638	0.5103	0.6667	0.4186	3.704	14.51

- Jet Energy Scale (JES)

Uncertainty of Jet Energy Scales is estimated by scaling the jet momenta in data using centrally provided uncertainties, which are estimated separately for each calibration step. JES uncertainties are the most dominant uncertainty of the measurement and it is of the order of 5 - 10 % for central jets and 10 - 25 % for forward jets.

- Jet Energy Resolution (JER)

The Jet Energy Resolutions is worse in data then in MC simulations. Thus, MC jets are smeared to mach the data resolution using officially provided factors.

The uncertainty of Jet Energy resolution is taken into account by varying the factor up and down around the central value. The effect is found to be around 1% for central jets and up to 10 % for forward jets.

- Luminosity

$\pm 2.6$  % of uncertainty is taken into account on the Luminosity measurements. This is applied on globally scaling to extract the cross section as well as the normalisation of background samples before subtracting from data.

- Pile-up

The uncertainty of pile-up reweighing is estimated on MC, by varying the minimum bias cross section up and down 5% to extract the weights applied on the MC samples which is then propagated to the unfolding.

- Pile-up subtraction method

To estimate the uncertainty of the method described in Section 4.7.3, the factors applied in data are varied by 50% and propagated through unfolding.

- cross sections

The cross sections used to normalise background samples listed in Table 4.4 are varied by 10 % for  $t\bar{t}$  and 15 % VV samples and subtracted from data before unfolding.

- Lepton ID and trigger efficiency corrections

The uncertainty on the Scale Factors used is taken into account, as a global uncertainty on the measurement as 2.5 % for muon and 0.5 % for electron final state.

- Unfolding

The uncertainty assigned to unfolding method is done by comparing an alternate model. An alternate sample generated by SHERPA 1.4 is used to build another unfolding machinery for each distribution. The data is then unfolded using this separate response, and the difference between the measurement and this one is assigned as unfolding uncertainty.

Theoretical uncertainties:

The theoretical uncertainties are estimated on MG5\_aMC sample, which provides internal reweighting method [96].

- QCD scale uncertainties

The fixed-order calculation uncertainties are estimated by varying the renormalisation and the factorisation scales by factors of  $1/2$  and  $2$ . The envelope of the variations of all factor combinations is taken as the uncertainty. The extrema, which are the two combinations when the scales are varied by  $1/2$  and by  $2$  respectively, are excluded from the envelope.

- PDF uncertainties

The uncertainty coming from the PDF's is estimated using replicas of the NNPDF 3.0 PDF set, by taking the RMS of 100 replicas as following PDF4LHC recommendations [97]. The uncertainty coming from the choice of  $\alpha_s$  in the simulations is taken into account by varying the value by 0.001.

#### 4.7.5 Combination of Electron and Muon Channels

The measurements carried out in di-electron and di-muon channels are combined to obtain a single Z production cross section in di-lepton channel. The solutions are found analytically using RooUnfold package. The combination is two fold; obtaining the central values, and combining the uncertainties.

For the combination of the central values, simple weighted average is done. For a binned measurement of say  $N$  bins, the combined result is the sum of the matrix multiplication, where the weights are represented with  $N \times 2N$  bins and the measurement as a vector of  $1 \times 2N$ , bins  $1-N$  corresponding to first channel, and  $(N+1)-2N$  to the second. Constraining physically that the sum of the weights should be one, one finds the weights in terms of individual channel total uncertainties.

The combination of uncertainties requires delicate handling of correlations between channels for different sources of uncertainties. The JES, JER, pile-up, luminosity and

cross section uncertainties are treated as fully correlated between channels. The rest are treated as uncorrelated.

More details of combination algorithm can be found in [98].

#### 4.7.6 Results

Obtained results of the differential cross section measurements are presented in this section, after being unfolded for detector effects and the results are combination of the two measurement channels.

##### 4.7.6.1 $d^2\sigma/dp_T(j_1)dy(j_1)$

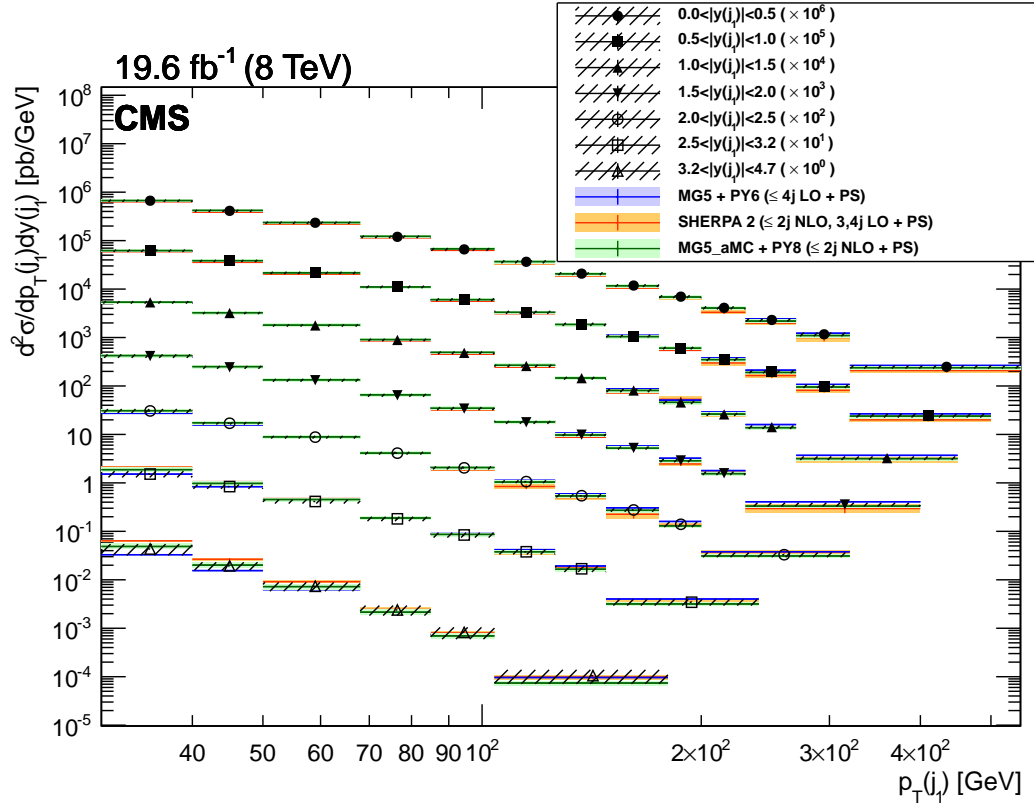


Figure 4.14: The differential cross section for Z + jets production as a function of the leading jet transverse momentum and rapidity.

The  $d^2\sigma/dp_T(j_1)d|y(j_1)|$  measurement, shown in Figure 4.14, corresponds to the

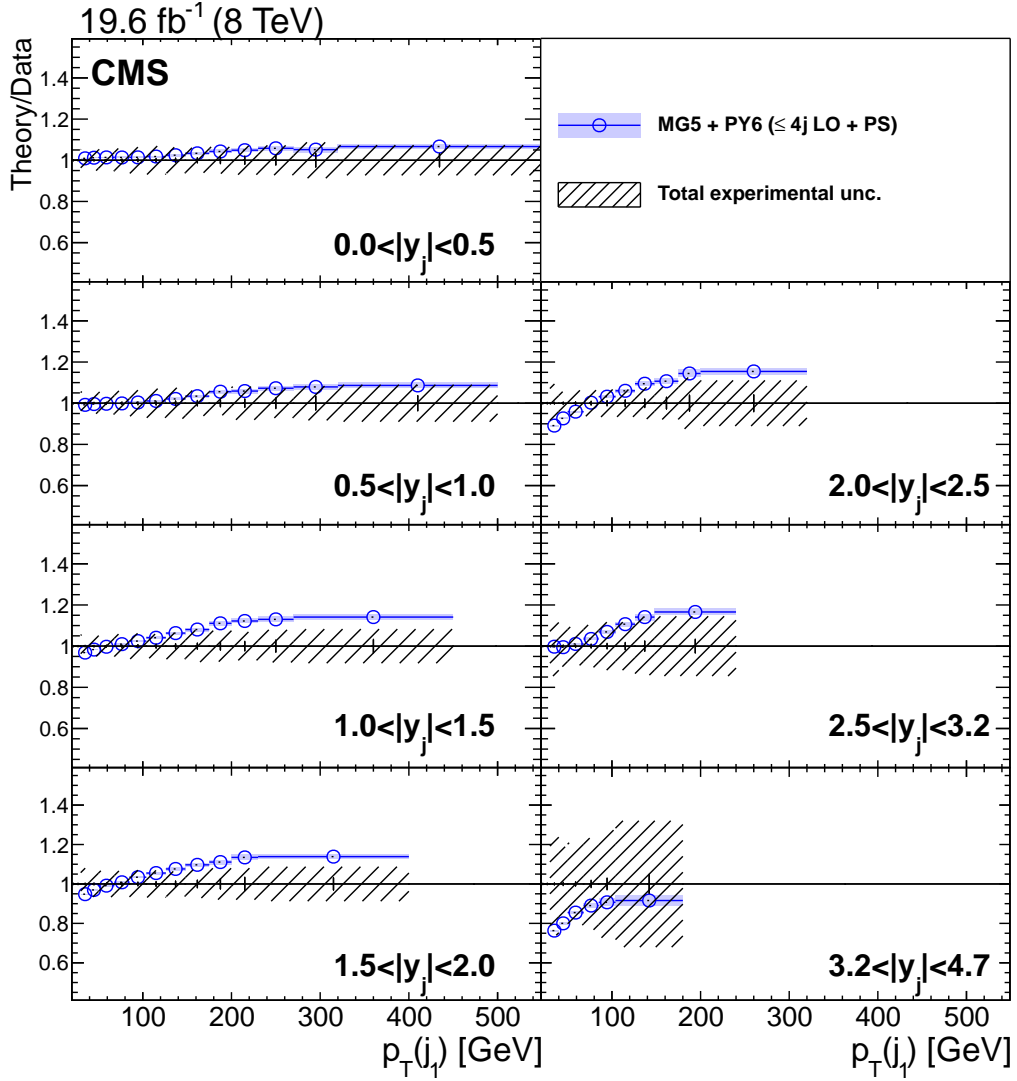


Figure 4.15: Ratio to the measurement of  $d^2\sigma/dp_T(j_1)dy(j_1)$  obtained with MADGRAPH 5 + PYTHIA 6.

range  $p_T < 550$  GeV of the one dimensional differential  $d\sigma/dp_T$  measurement done up to 1 TeV presented in Ref. [11] extending the jet absolute rapidity range up to 4.7. The ratios of the obtained results to the theoretical predictions from MADGRAPH 5 + PYTHIA 6, SHERPA 2, and MG5\_aMC + PYTHIA 8 are presented in Figures 4.15–4.16. A disagreement in the shapes of the  $d\sigma/dp_T$  spectrum is observed between the measurement and the predictions computed with MADGRAPH 5 + PYTHIA 6. This disagreement becomes more prominent when moving from the central region ( $|y(j_1)| = 0$ ) to the more forward region ( $|y(j_1)| = 2.5$ ). However, when comparing SHERPA 2, and MG5\_aMC + PYTHIA 8 predictions, such a dependence on the

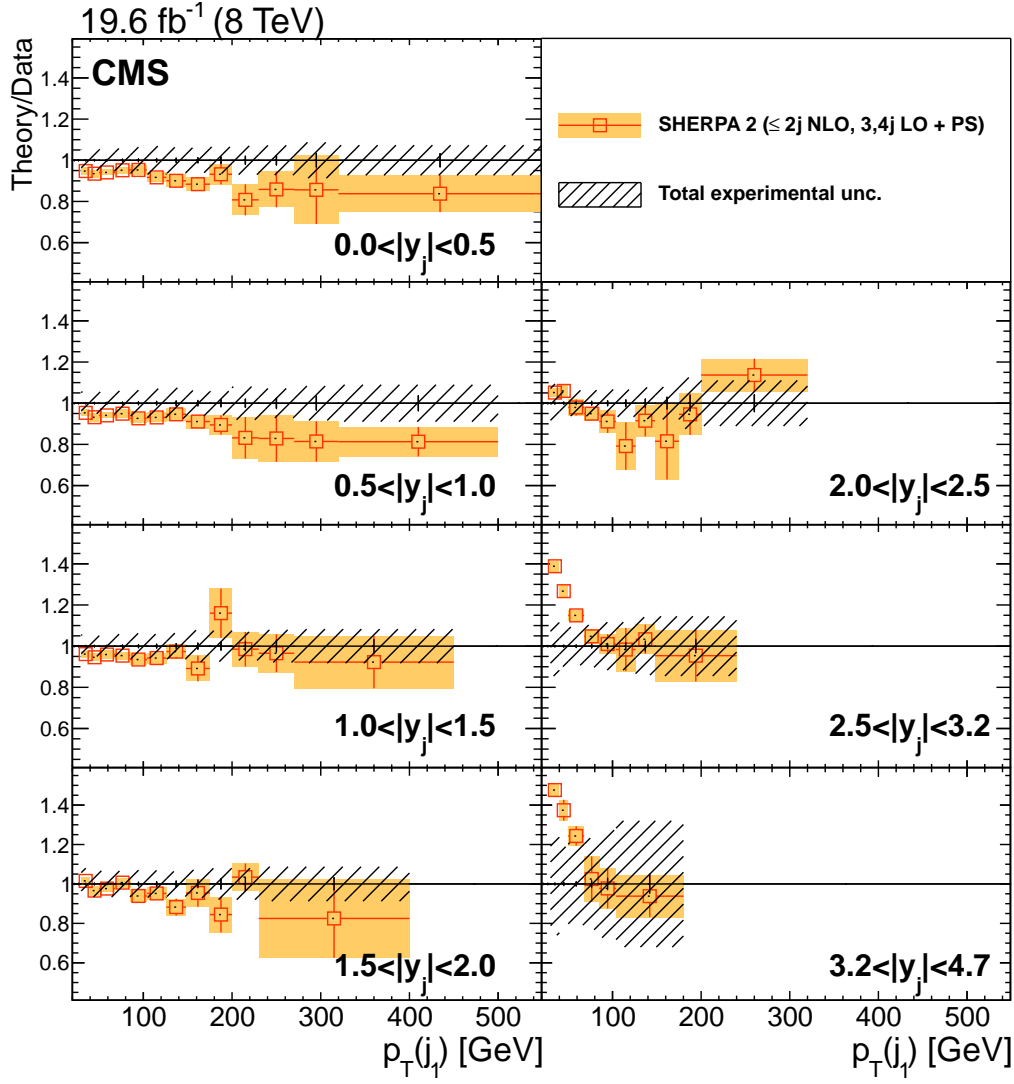


Figure 4.16: Ratio to the measurement of  $d^2\sigma/dp_T(j_1)dy(j_1)$  obtained with SHERPA 2.

rapidity of the jet for the region  $|y(j_1)| < 2.5$  is not observed within the statistical uncertainty of the prediction, that is larger than the MADGRAPH 5 + PYTHIA 6 sample.

In the forward region beyond  $|y(j_1)| = 2.5$  the MADGRAPH 5 + PYTHIA 6 predictions shows the same feature as for  $|y(j_1)| < 2.5$ , despite the large experimental uncertainties in this region mainly due to a larger jet energy scale uncertainty. The SHERPA 2 prediction shows a significant difference with the spectrum of the jet transverse momentum being narrower than in data. The MG5\_aMC + PYTHIA 8 shows a similar feature, but less pronounced than SHERPA 2 predictions, and MG5\_aMC + PYTHIA 8 discrepancy is covered by the experimental uncertainties.

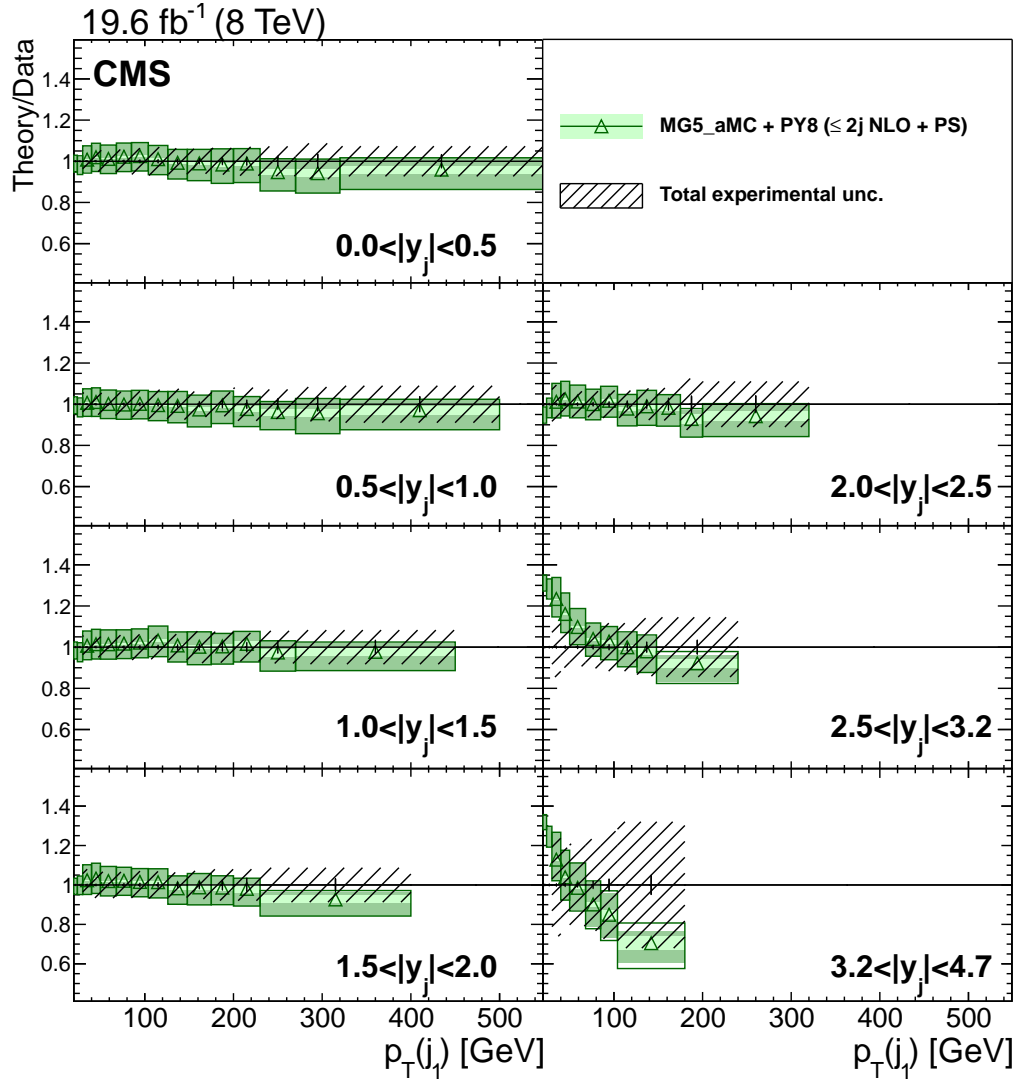


Figure 4.17: Ratio to the measurement of  $d^2\sigma/dp_T(j_1)dy(j_1)$  obtained with MG5\_aMC + PYTHIA 8.

#### 4.7.6.2 $d^2\sigma/dy(Z)dy(\mathbf{j}_1)$

The Z boson and jet rapidity distributions are independently well-modelled by all the simulation samples as reported in Ref. [11]. However, it is also observed that the correlations between these two observables are not described well by the tree-level calculations. The two-dimensional cross section with respect to both rapidities is shown in Figures. 4.18–4.20 . the MADGRAPH 5 + PYTHIA 6 calculation predicts a more central leading jet when the Z boson is central. On contrary when the Z is forward, MADGRAPH 5 + PYTHIA 6 predicts a more forward leading jet in the same hemisphere ( $y(Z) \cdot y(\mathbf{j}_1) > 0$ ). The prediction from SHERPA 2, and MG5\_aMC + PYTHIA 8 agree well with the measurement when the jet is in the central region ( $|y(\mathbf{j}_1)| < 2.5$ ), while some discrepancies are observed when the jet is in more forward regions. The MC samples predict more tails in the rapidity, especially when the Z boson and the jets are well separated in rapidity; such as when the Z boson and the jet are in opposite hemispheres ( $y(Z) \cdot y(\mathbf{j}_1) < 0$ ) the discrepancy gets larger for higher  $|y(Z)|$ . The discrepancies are bigger for the prediction obtained with SHERPA 2.



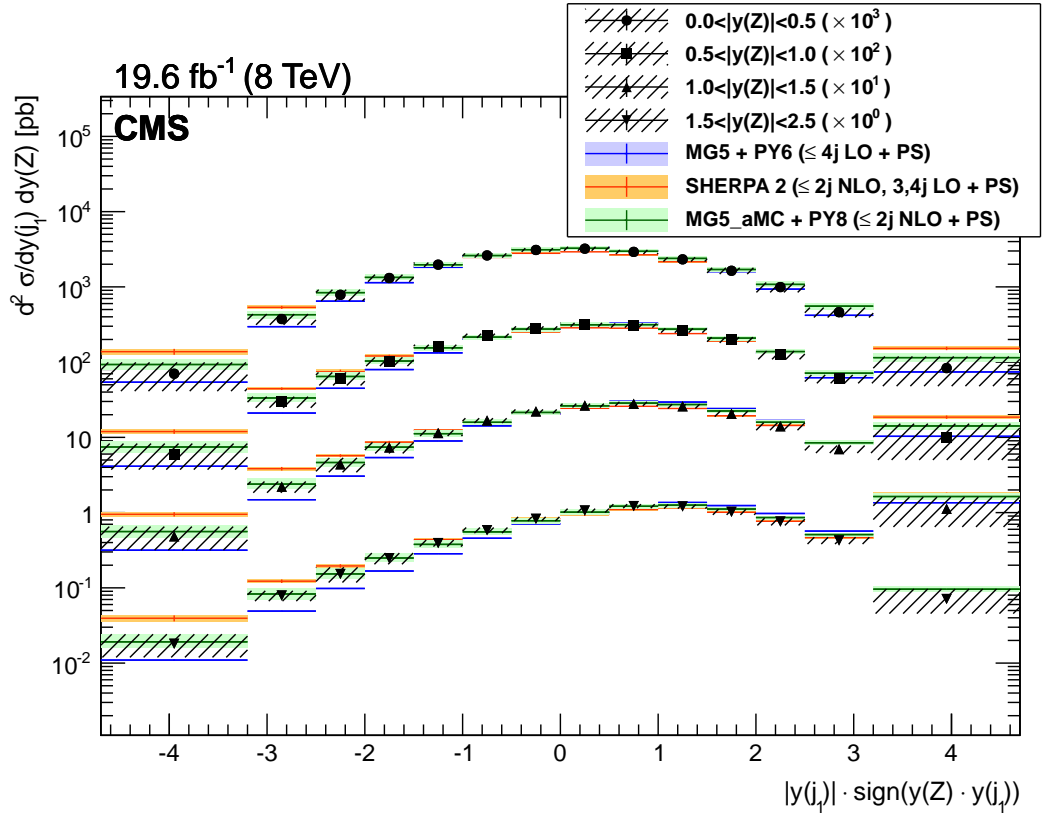


Figure 4.18: The differential cross section for Z + jets production as a function of the Z boson and leading jet rapidity.

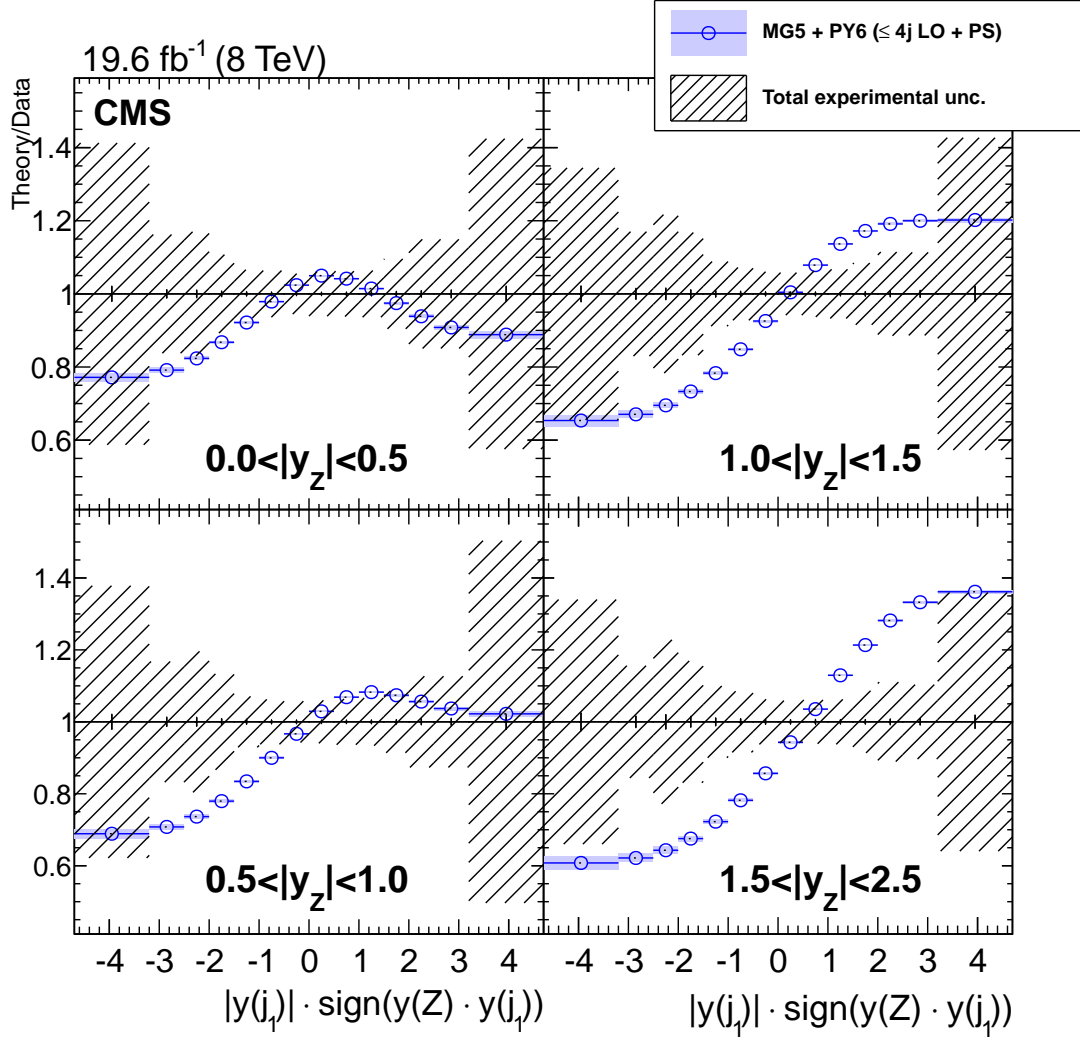


Figure 4.19: Ratio to the measurement of  $d^2\sigma/dy(Z)dy(j_1)$  obtained with MADGRAPH 5 + PYTHIA 6.

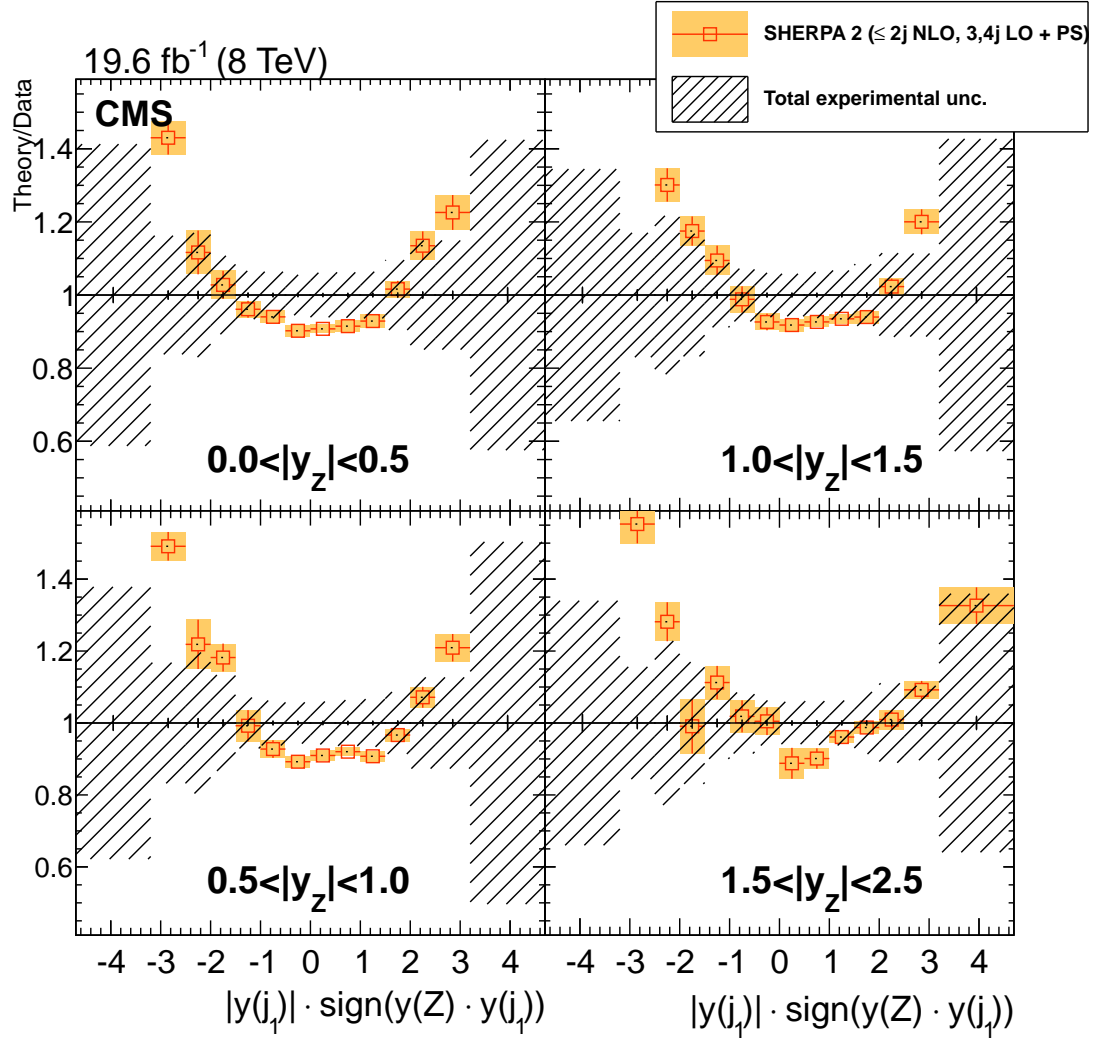


Figure 4.20: Ratio to the measurement of  $d^2\sigma/dy(Z)dy(j_1)$  obtained with SHERPA 2.

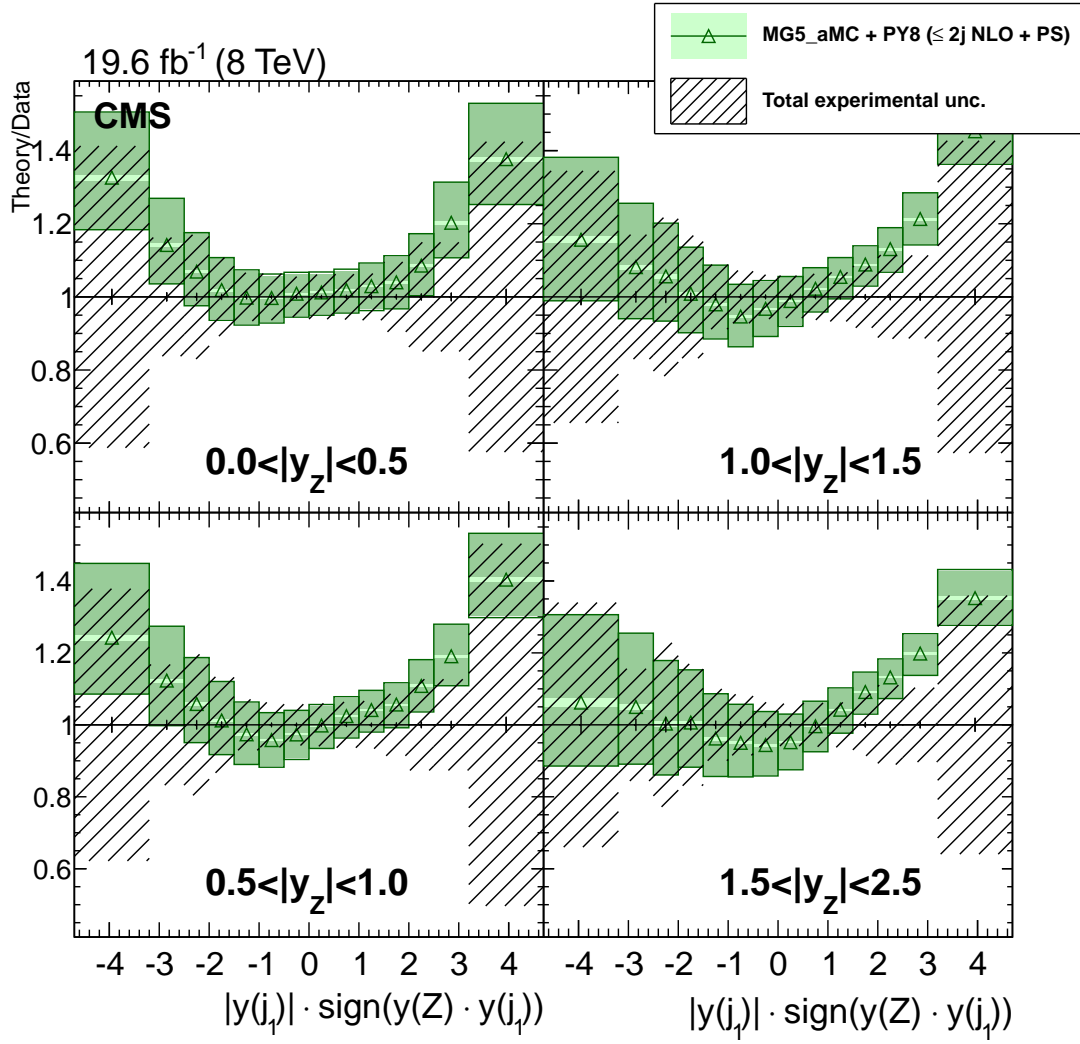


Figure 4.21: Ratio to the measurement of  $d^2\sigma/dy(Z)dy(j_1)$  obtained with MG5\_aMC + PYTHIA 8.

#### 4.7.6.3 $d^3\sigma/dp_T(\mathbf{j}_1)dy(\mathbf{j}_1)dy(Z)$

Finally, the measurement of the differential cross section is shown. The measurement with respect to both jet transverse momentum and rapidity has been repeated for two different bins of the Z boson rapidity as shown in Figures 4.22–4.26. MADGRAPH 5 + PYTHIA 6 prediction to the measurement shape of the leading jet  $p_T$  spectrum is similar in both Z rapidity intervals. However the prediction shows a more pronounced discrepancy when the boson is in the most forward region ( $|y(Z)| \in (1, 2.5)$ ). In the jet rapidity region,  $|y(j_1)| \in (1, 5, 2.5)$  with same sign configuration ( $y(j_1) \cdot y(Z) > 0$ ), the shape of the ratios actually differ between the two Z boson rapidity intervals. However, this discrepancy cannot be considered as significant when considering the precision of the measurement. The features seen in previous section for  $d^2\sigma/(dy(Z)dy(j_1))$  translates into global shifts of the ratio distributions depending on the  $y(Z)$  and  $y(j_1)$  intervals as well as Z boson and jets being in same and opposite hemispheres.

The bottom plots of Figures 4.25 to 4.28 give more understanding of the discrepancy observed previously for the SHERPA 2, and MG5\_aMC + PYTHIA 8 predictions for the jet in the forward region ( $|y(j_1)| \in (2.5, 4.7)$ ). The observed deficit in the cross section can be attributed to soft jets, since higher cross section values with the leading jet below 90 GeV are expected by the predictions. The discrepancy is larger when the Z boson and the leading jet are well separated in rapidity, as seen in bottom right plot of Figure 4.28, and it is observed that the discrepancy is the smallest for the region  $|y(Z)| \in (1, 2.5)$  and  $y(Z) \cdot y(j_1) > 0$ , which corresponds to the region where the the boson and the jet are closest to each other.

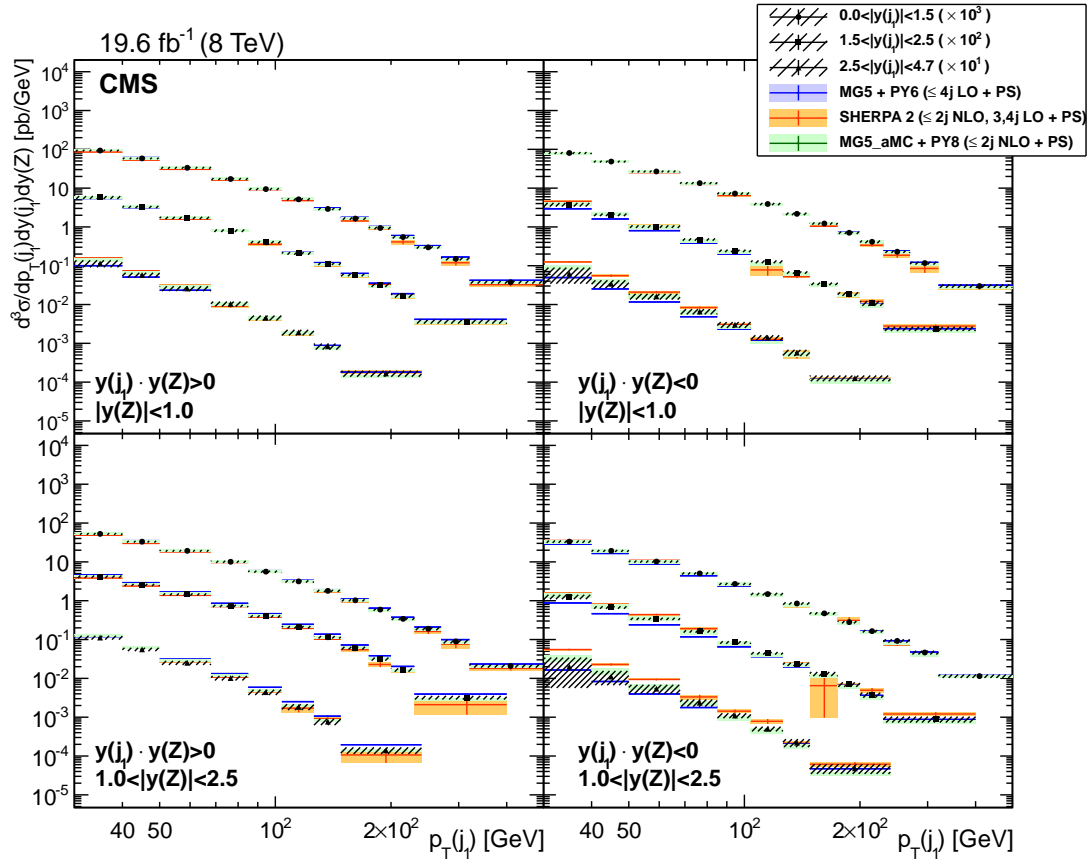


Figure 4.22: The differential cross section for Z + jets production as a function of the rapidities of the Z boson and leading jet, and of the transverse momentum of the jet for the configuration.

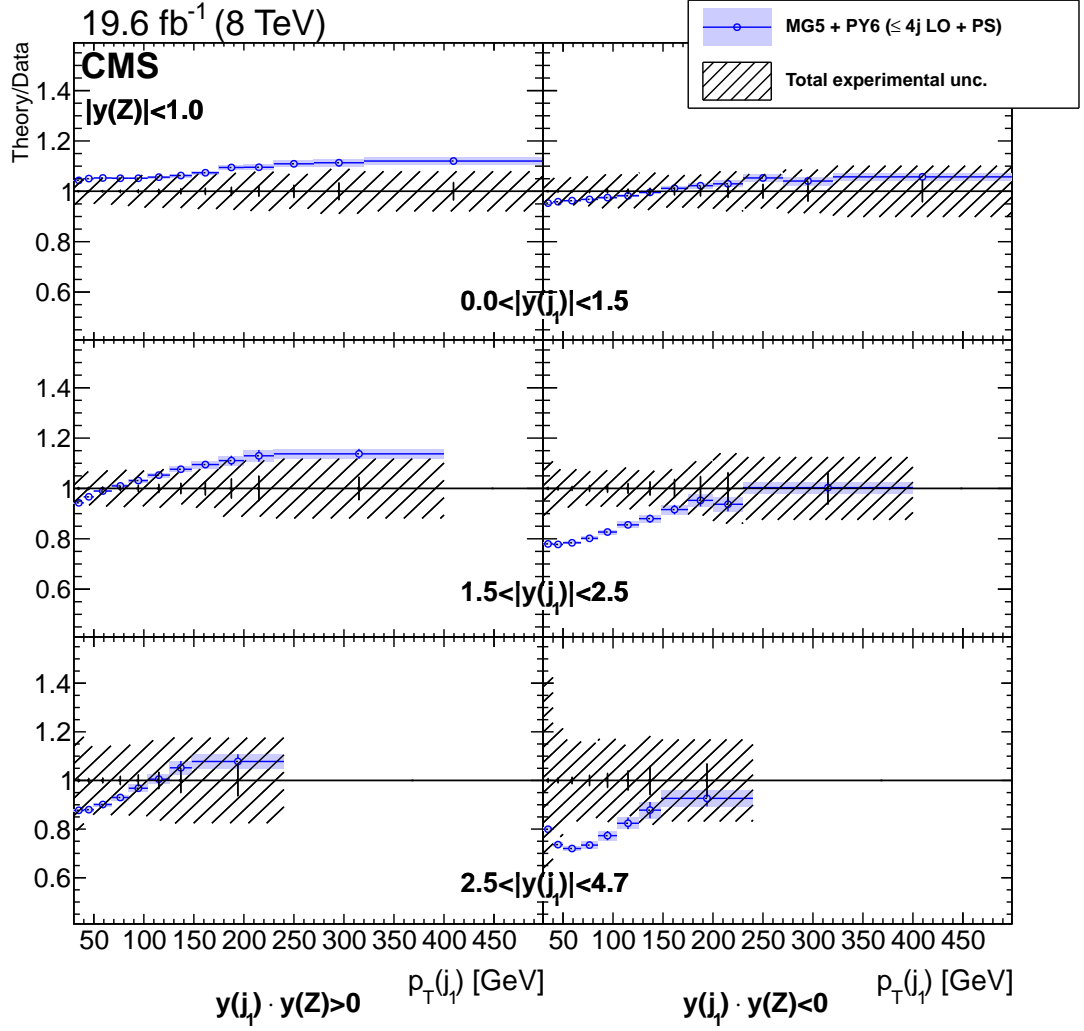


Figure 4.23: Ratio to the measurement of  $d^3\sigma/dp_T(j_1)dy(j_1)dy(Z)$  obtained with MADGRAPH 5 + PYTHIA 6.

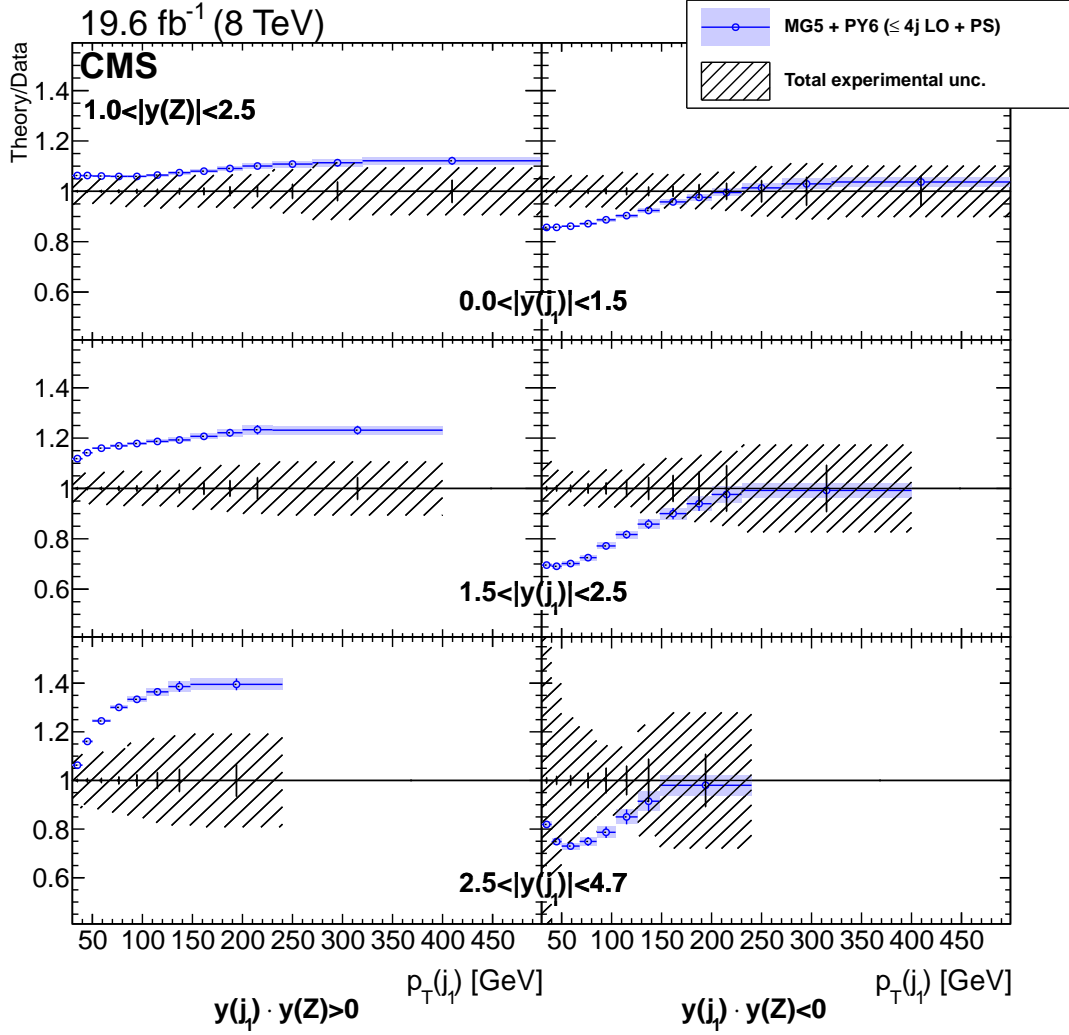


Figure 4.24: Ratio to the measurement of  $d^3\sigma/dp_T(j_1)dy(j_1)dy(Z)$  obtained with MADGRAPH 5 + PYTHIA 6.



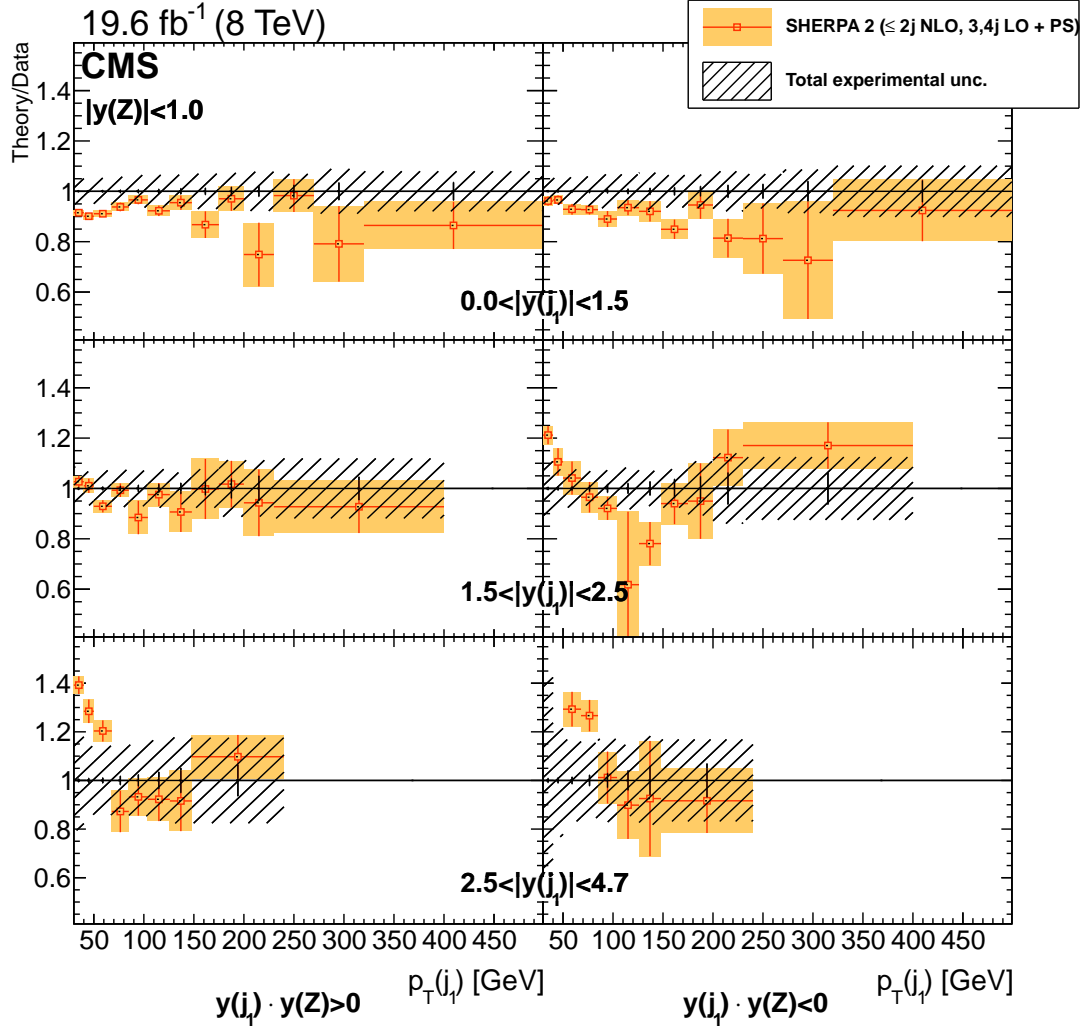


Figure 4.25: Ratio to the measurement of  $d^3\sigma/dp_T(j_1)dy(j_1)dy(Z)$  obtained with SHERPA 2.

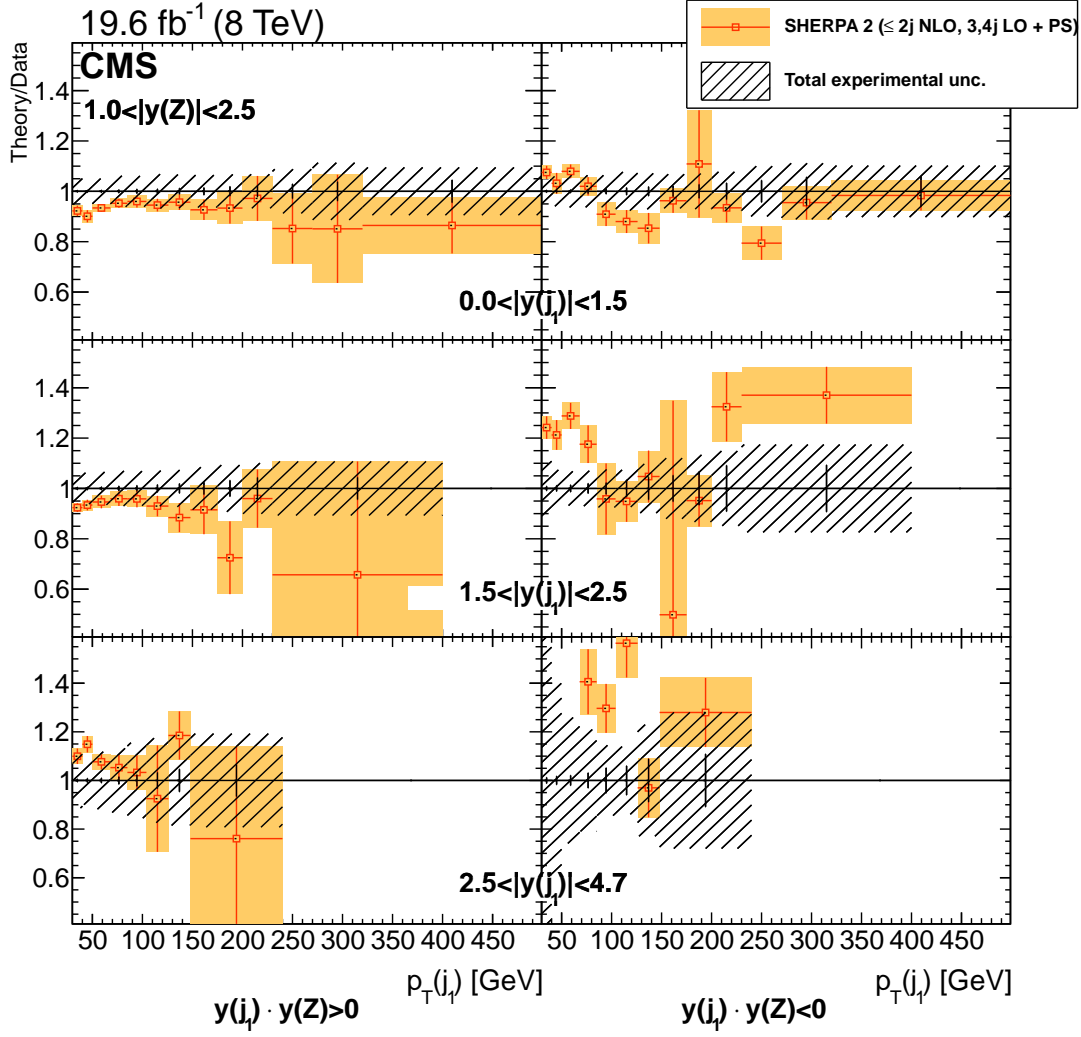


Figure 4.26: Ratio to the measurement of  $d^3\sigma/dp_T(j_1)dy(j_1)dy(Z)$  obtained with SHERPA 2.

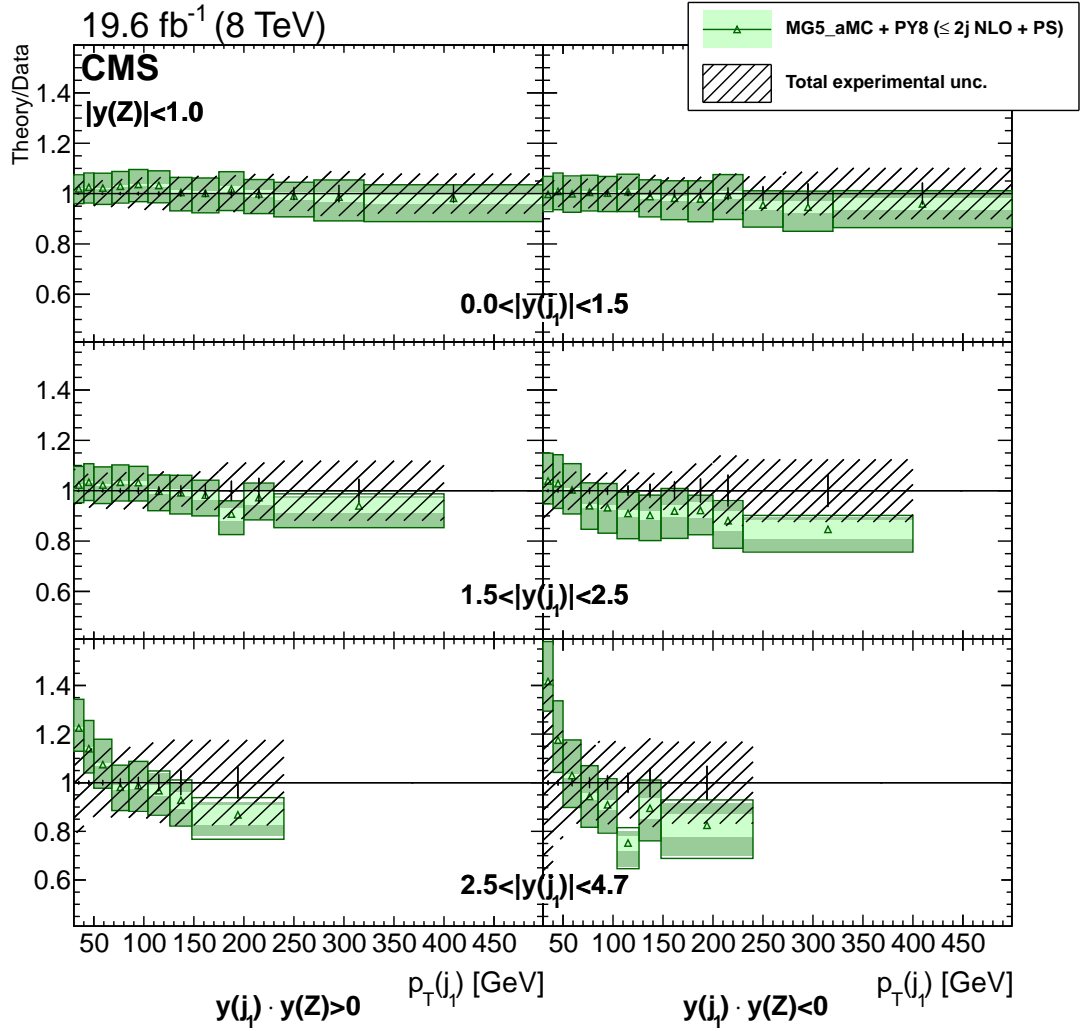


Figure 4.27: Ratio to the measurement of  $d^3\sigma/dp_T(j_1)dy(j_1)dy(Z)$  obtained with MG5\_aMC + PYTHIA 8.

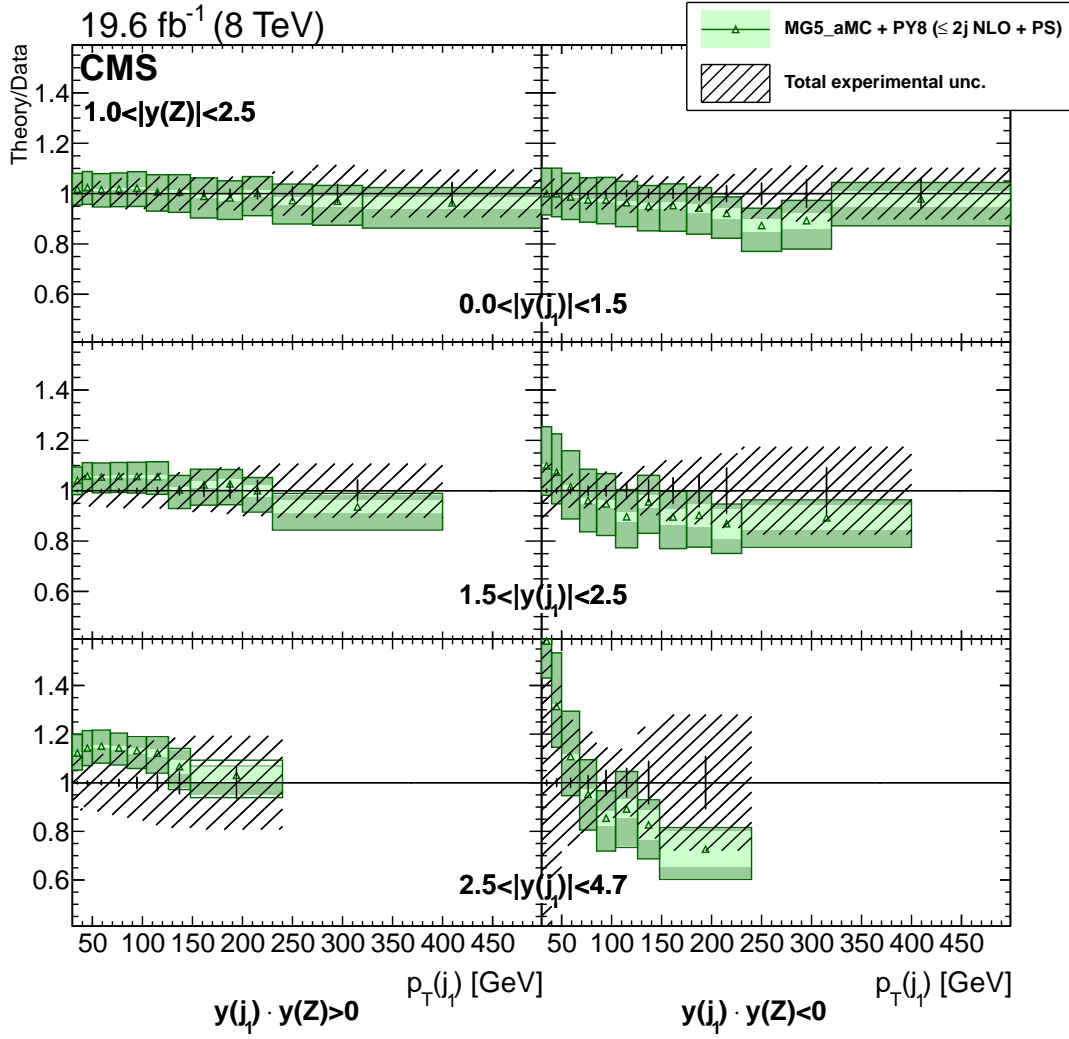


Figure 4.28: Ratio to the measurement of  $d^3\sigma/dp_T(j_1)dy(j_1)dy(Z)$  obtained with MG5\_aMC + PYTHIA 8.

## 4.8 Underlying Event Study with $t\bar{t}$

As described in detail in Chapter 2, the QCD Monte Carlo (MC) generators such as PYTHIA and HERWIG++ have parameters that may be adjusted to control the behavior of their event modeling. A specified set of these parameters that has been adjusted to better fit some aspects of the data is referred to as a "tune". The PYTHIA8 tune CUETP8M1 and the HERWIG++ tune EE5C are constructed by fitting the UE data at several center-of-mass energies, where the "leading object" is the highest transverse momentum charged particle or the highest transverse momentum charged-particle jet in the event. These tunes also describe well the UE as measured in Z-boson production. However, very little is known about the UE in heavy quark production.

In this section, analysis of UE in top-quark production using 13 TeV data is presented. The  $t\bar{t}$  pair is used as the leading object to probe the UE.

### 4.8.1 Kinematic Reconstruction

The kinematics of the  $t\bar{t}$  system is reconstructed in the  $\mu + jets$  final state. In each event, the reconstruction starts with leptonically decaying W boson using the lepton momentum and the  $E_T^{\text{miss}}$ .

The longitudinal component of the neutrino,  $p_{z,\nu}$ , is determined by means of the quadratic equation given below, depending on the charged lepton kinematics, with the constraint that the reconstructed W boson mass be 80.4 GeV.

$$p_{z,\nu}^{\pm} = \frac{\mu p_{z,l}}{p_{T,l}^2} \pm \sqrt{\frac{\mu^2 p_{z,l}^2}{p_{T,l}^4} - \frac{E_l^2 p_{T,\nu}^2 - \mu^2}{p_{T,l}^2}} \quad (4.7)$$

$$\mu = \frac{M_W^2}{2} + p_{T,l} p_{T,\nu} \cos \Delta\phi \quad (4.8)$$

For 34% of the events, the discriminant in the equation is negative and yields complex solutions. This situation is attributed to resolution of  $E_T^{\text{miss}}$ . As a solution, the  $x$  and  $y$  components of the  $E_T^{\text{miss}}$  are varied to make the W boson transverse mass ( $m_{T,W}$ ) equal to 80.4 GeV, which makes the discriminant zero. As a result of this, 89% of these events with complex solutions are recovered. For the remaining 11% no solution is found by varying the  $x$  and  $y$  components of the  $E_T^{\text{miss}}$ .

Then, the jet pair that gives the invariant mass closest to 80.4 GeV is selected among the jets that are not b-tagged, and this pair is assigned to the hadronic top quark ( $t_{\text{had}}$ ). The two (or one) neutrino solutions are used to select the lepton-neutrino-b-jet combination that gives the invariant mass closest to the top quark mass of 172.5 GeV. This combination corresponds to the leptonic top quark ( $t_{\text{lep}}$ ). The remaining b-tagged jet is assigned to the hadronic top quark. The obtained invariant mass distribution of top quarks is shown in Figure 4.30. The overall shift of 10% is attributed to efficiencies of selections applied, which is not corrected for.

An example event display, showing a candidate  $t\bar{t}$  event, is shown in Figure 4.29. This event has one isolated muon, transverse missing energy of 34 GeV, and five hadronic jets. Two of the jets pass the b-tagging discriminant and are interpreted as originating from the b quarks from top quark decay. Two of the others form an invariant mass of 72 GeV and are interpreted as coming from a hadronically-decaying W boson. As the result of kinematic reconstruction, leptonically decaying top mass is found to be 166 GeV, and the hadronic one as 162 GeV.

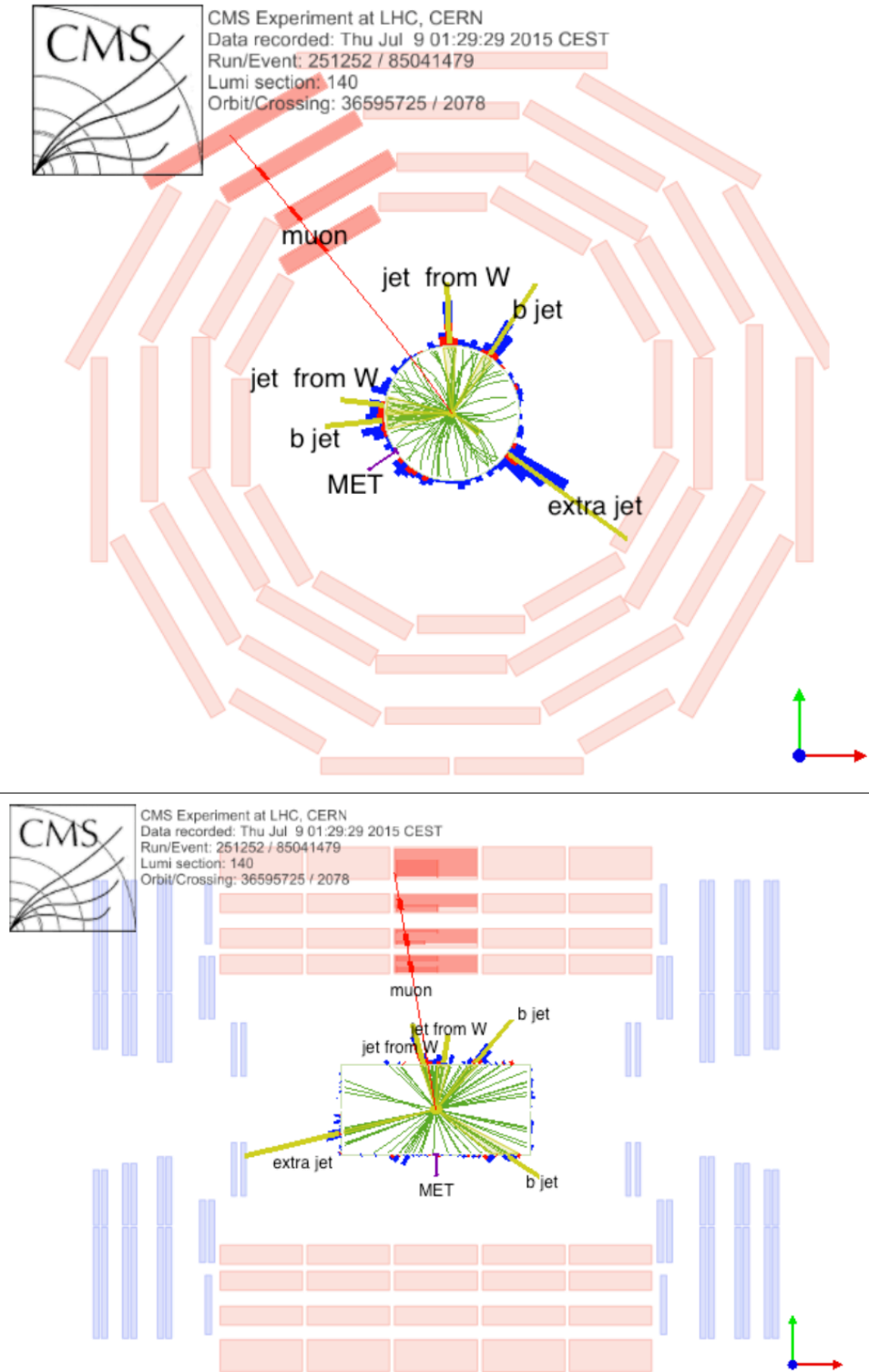


Figure 4.29: Event display of a top-quark pair candidate produced in association with a jet in  $x - y$  (left) and  $r - z$  (right) views.

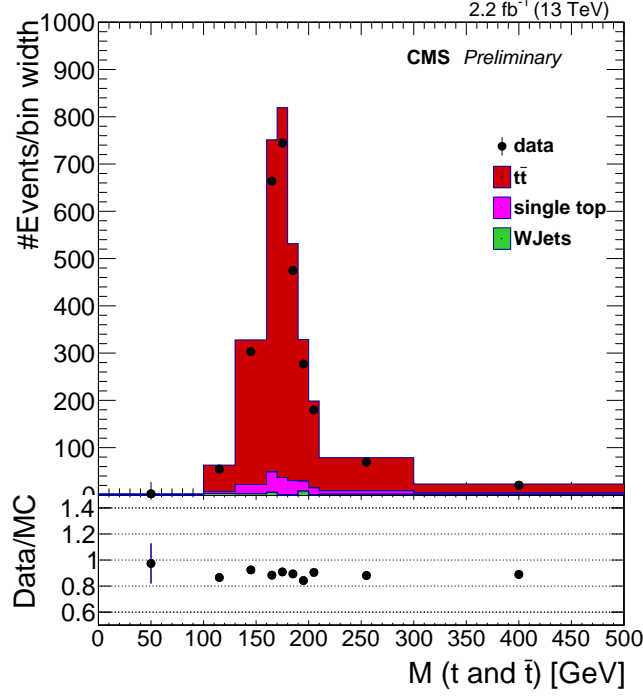


Figure 4.30: The obtained invariant mass of top quarks after kinematic reconstruction

The following azimuthal angle is defined to characterize soft events:

$$\phi^k = \tan^{-1} \frac{p_y^k}{p_x^k}, \quad (4.9)$$

where  $k$  represents either the  $t\bar{t}$  system or a charged particle candidate. The soft event regions are defined as in Table 4.7 using the azimuthal angle difference between the  $t\bar{t}$  system and the charged particle candidates,  $\Delta\phi$ . The charged PF candidates found in a  $60^\circ$  around  $\phi^{t\bar{t}}$  are considered to be produced in the "toward" direction, while the particles in the opposite direction are considered to be produced in the "away" direction. The charged particles remaining within  $60-120^\circ$  of  $\phi^{t\bar{t}}$  are considered to be produced in the "transverse" direction. The transverse and toward regions are expected to be mostly populated by the soft event activity, to be sensitive to the multi-parton-interactions and beam-beam-remnant components of the underlying event. The away region is sensitive to the modeling of the recoil of the  $t\bar{t}$  system.



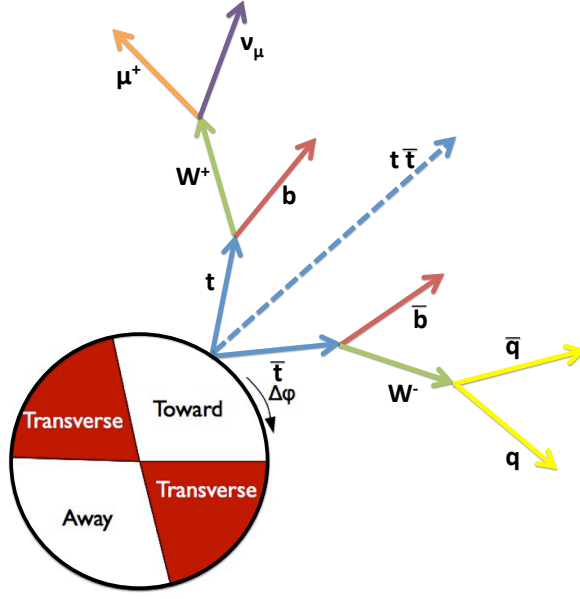


Figure 4.31: Schematic view of the UE regions defined with respect to the azimuthal angle difference between the charged particle candidate and the axis of the  $t\bar{t}$  system with a schematic diagram of  $t\bar{t}$  decay chain.

Table 4.7: Definition of the soft event regions.

toward	$\Delta\phi < 60^\circ$
transverse	$60^\circ < \Delta\phi < 120^\circ$
away	$\Delta\phi > 120^\circ$

#### 4.8.2 Categorization of the Events

To study the effect of the modeling of the recoil, the sample is studied inclusively, as well as in three jet multiplicity bins: 0, 1, and  $\geq 2$  jets. The jets are required to have  $p_T > 15$  GeV and to be produced in association with the  $t\bar{t}$  event. In this section, these jets are referred to as "extra jets", meaning the jets accompanying the  $t\bar{t}$  as extras.

The measured quantities are the charged multiplicity ( $N_{ch}$ ), the scalar sum of the transverse momenta of the charged particles ( $\Sigma p_T$ ), and the average transverse momentum per charged particle  $\overline{p_T}$ .

The stability of the measurement with respect to pile-up is verified by measuring  $N_{ch}$  and  $\Sigma p_T$  for different numbers of primary vertices.

The uncertainty originating from the modeling of the initial- and final-state-radiation (ISR/FSR) in  $t\bar{t}$  events is expected to be accounted for by the factorization and renormalization scale uncertainties. These are calculated by using dedicated  $t\bar{t}$  samples in which the renormalization scale in the parton shower simulation is varied by factors of 2 and 0.5.

### 4.8.3 Results

Obtained results of the charged particle distributions are presented in this section. The presented results are at "detector level", any correction for smearing effects via unfolding is not applied.

### 4.8.4 Charged Particle Activity: Inclusive

In Figures 4.32-4.34, the distributions of  $N_{ch}$ ,  $\Sigma p_T$  and  $\overline{p_T}$  are shown for the overall sample and the three regions defined in the previous section. Predicted distributions obtained with the nominal  $Q^2$  scale as well as  $(2Q)^2$ , and  $(Q/2)^2$  are displayed separately. The nominal scale is set to top quark transverse mass ( $m_T(t)$ ) event-by-event. The predictions from the POWHEG+ PYTHIA8 generator agree well with data in all regions, though a slightly better agreement is observed for charged multiplicities smaller than about 50. For charged particle multiplicities higher than  $\sim 50$ , POWHEG+ PYTHIA8 predicts a higher multiplicity especially in the away region.

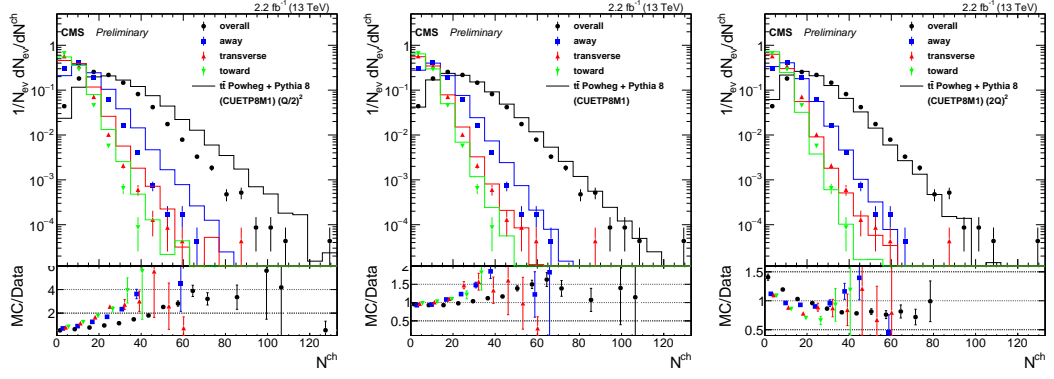


Figure 4.32: The charged PF candidate multiplicity distributions for the away, transverse and toward regions as well as for the overall sample.

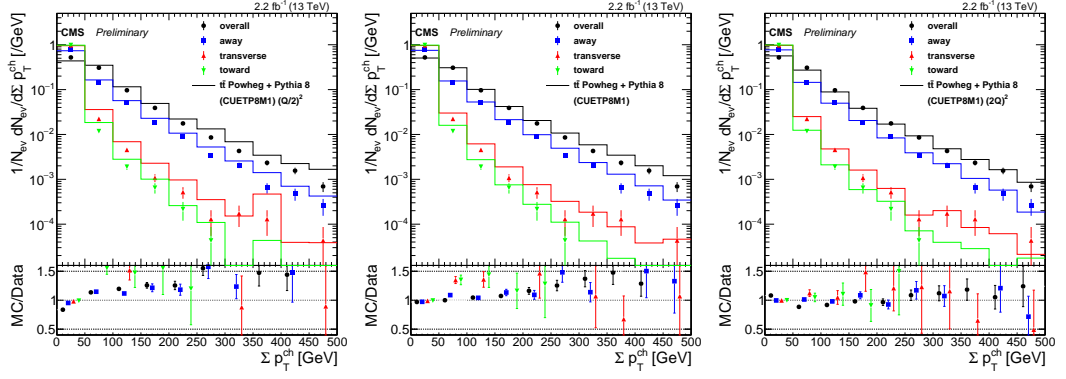


Figure 4.33: The transverse momentum sum distributions of the charged PF candidates for the away, transverse and toward regions as well as for the overall sample.

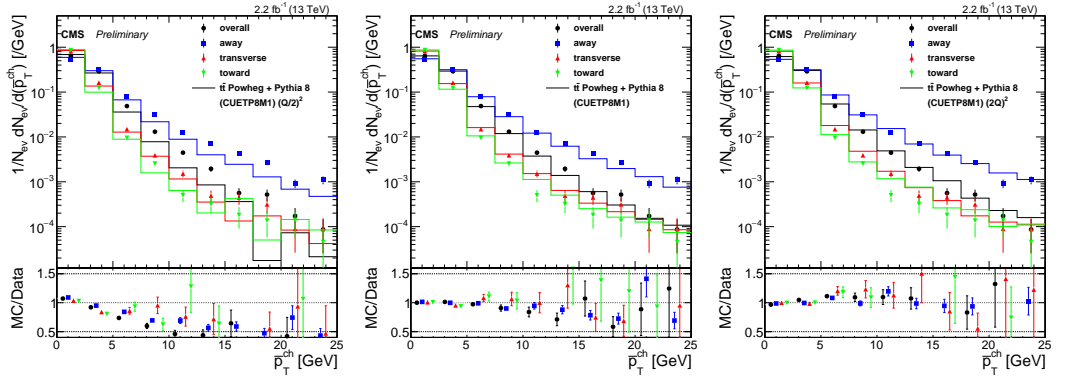


Figure 4.34: The average transverse momentum distributions of the charged PF candidates for the away, transverse and toward regions as well as for the overall sample.

#### 4.8.5 Charged Particle Activity: Profile Against $t\bar{t}$ Kinematical Variables

Distributions of average  $N_{ch}$ ,  $\Sigma p_T$  and  $\overline{p_T}$  are displayed in Figures 4.35-4.37 with respect to the azimuthal angle between the  $t\bar{t}$  system and the charged PF candidate ( $\Delta\phi$ ) and in Figures 4.38-4.37 with respect to  $p_T(t\bar{t})$ . When there are no extra jets (i.e. no jets other than the four jets associated with the  $t\bar{t}$  production) with  $p_T(j) > 15$  GeV and  $|\eta| < 2.4$ , only a very small increase in  $N_{ch}$ ,  $\Sigma p_T$  or  $\overline{p_T}$  with increasing  $\Delta\phi$  is observed. Conversely, as the number of extra jets increases,  $N_{ch}$ ,  $\Sigma p_T$  and  $\overline{p_T}$  grow significantly with  $\Delta\phi$ . This may be explained by the fact that in the presence of an extra jet in the event, more of the recoil particles are clustered in the jet and the  $t\bar{t}$  system becomes more boosted. This is supported by Figures 4.38-4.40, which show that  $N_{ch}$ ,  $\Sigma p_T$  and  $\overline{p_T}$  increase with  $p_T(t\bar{t})$  only in the away direction. In Figures 4.35-4.40, data at the detector level are compared to POWHEG+ PYTHIA8 and POWHEG+ HERWIG++ predictions with different renormalization scales. The scale dependence is most prominent in the UE observables measured as a function of  $p_T(t\bar{t})$  for events with no extra jets.

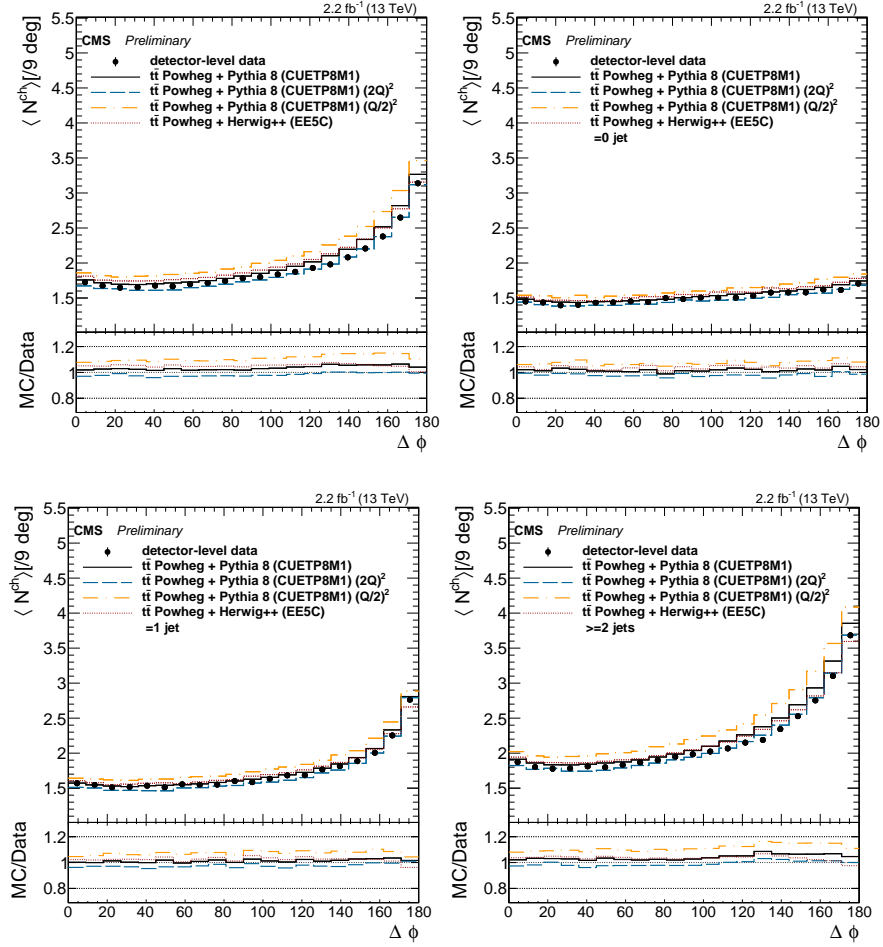


Figure 4.35: The number of charged particles vs the angle with respect to the event-by-event axis defined using  $p_T^{t\bar{t}}$  for the inclusive and no extra jet events (top), and for the events with one and at least two extra jets (bottom).

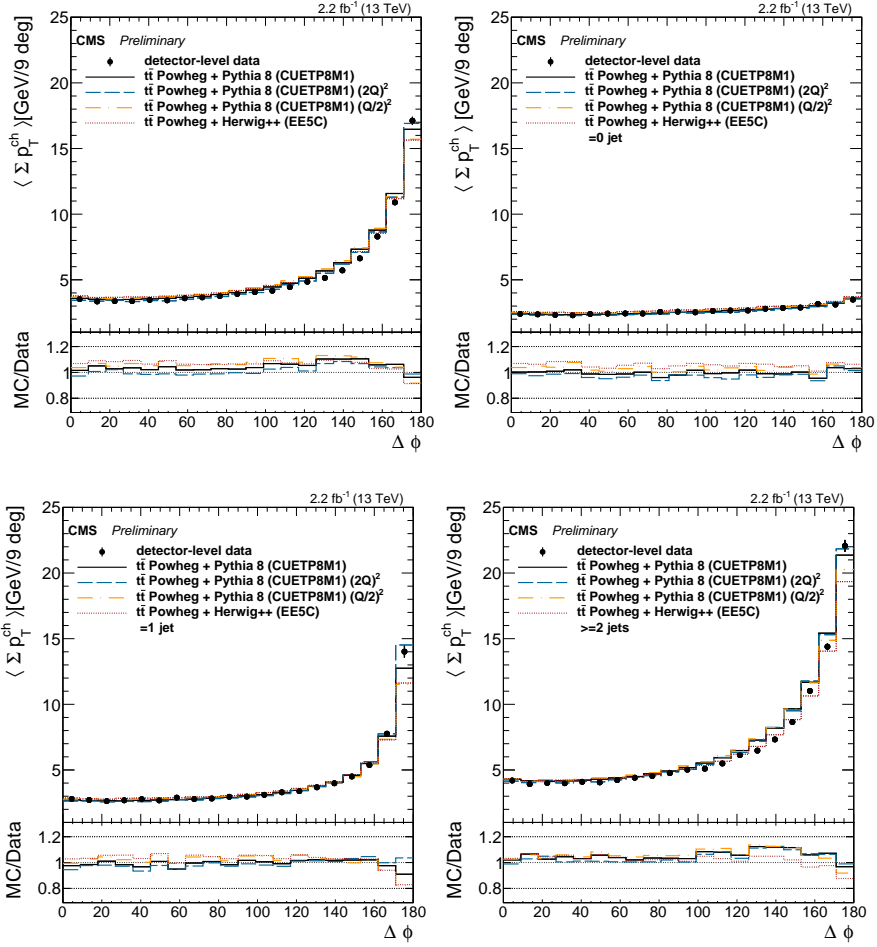


Figure 4.36: Sum of the charged  $p_T$  vs the angle with respect to the event-by-event axis defined using  $p_T^{\text{tt}}$  for the inclusive and no extra jet events (top), and for the events with one and at least two extra jets (bottom).

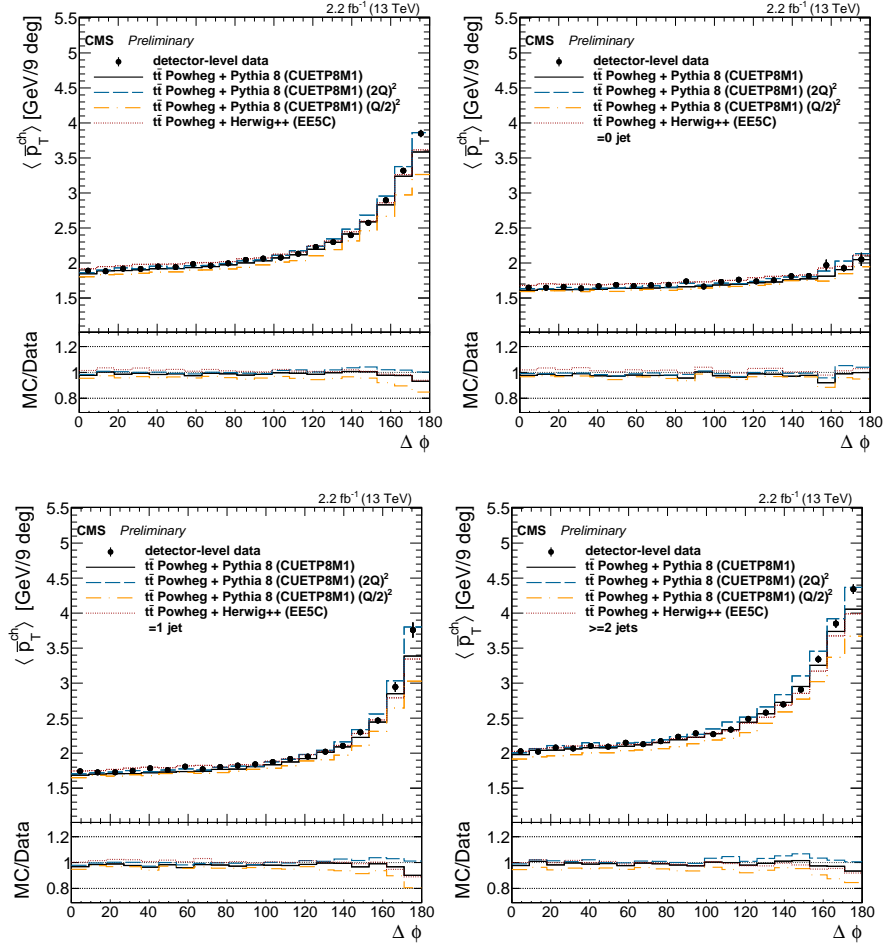


Figure 4.37: The average  $p_T$  per charged particle vs the angle with respect to the event-by-event axis defined using  $p_T^{t\bar{t}}$  for the inclusive and no extra jet events (top), and for the events with one and at least two extra jets (bottom).

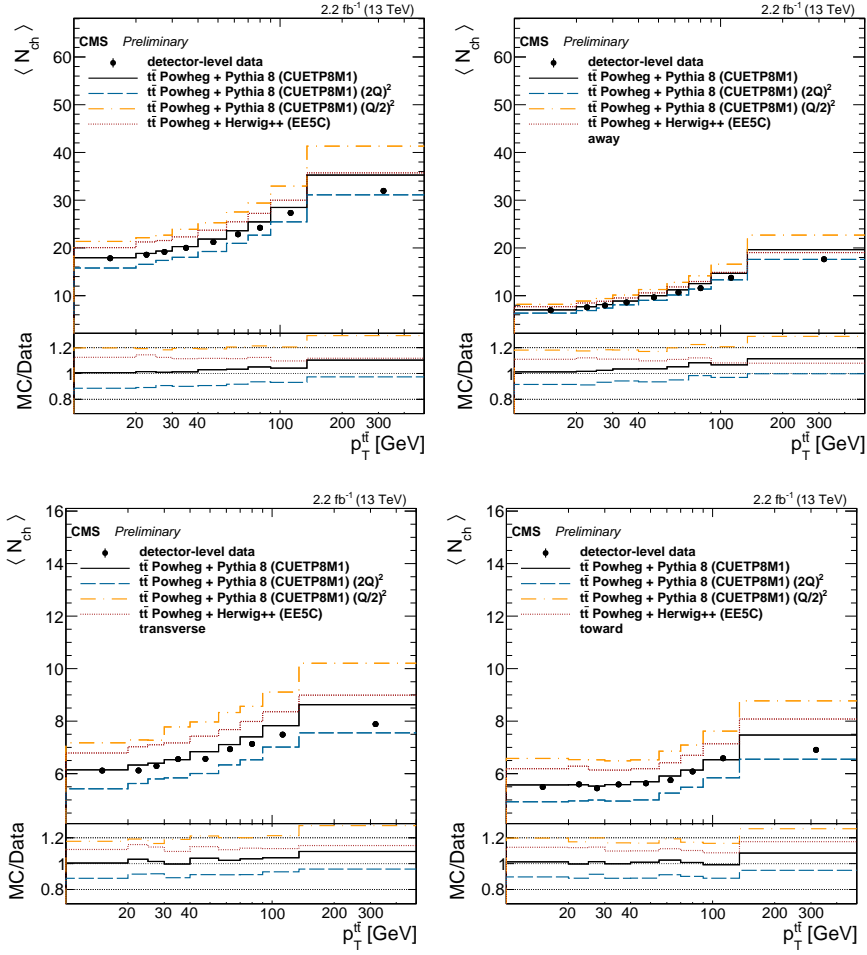


Figure 4.38: The number of charged particles vs  $p_T^{t\bar{t}}$  for the overall sample and the away (top), transverse and toward regions (bottom) defined with respect to  $\Delta\phi$ .



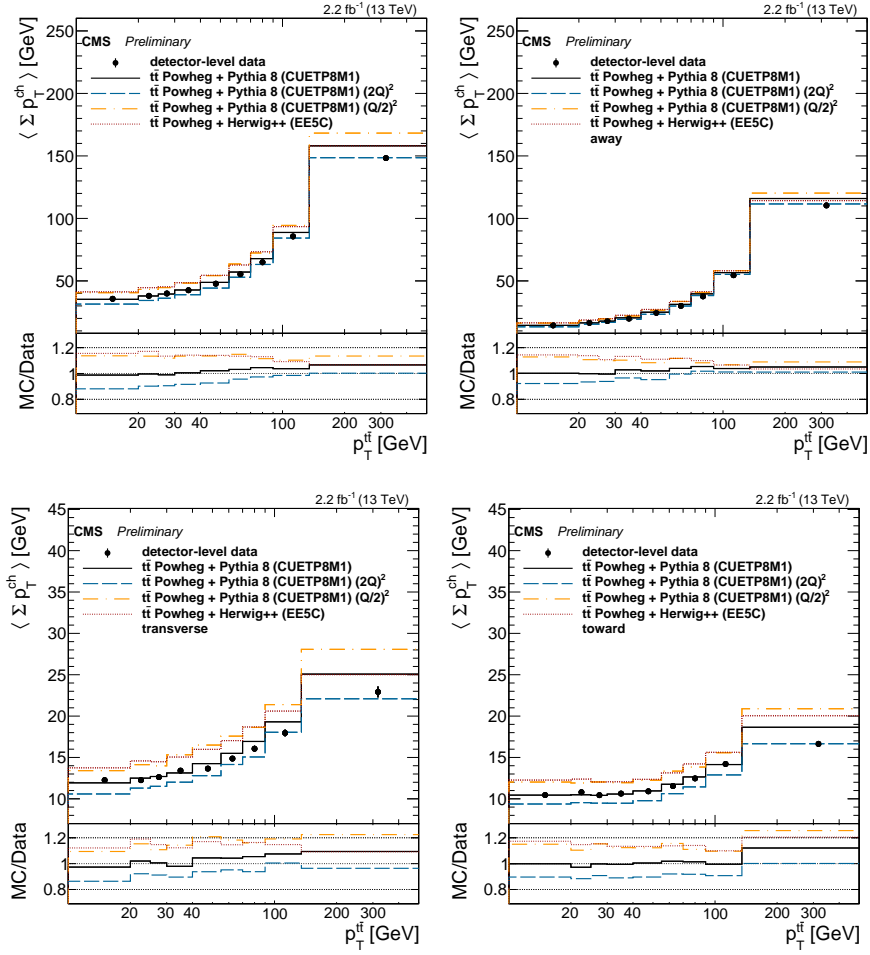


Figure 4.39: Sum of charged  $p_T$  vs  $p_T^{\text{tt}}$  for the overall sample and the away (top), transverse and toward regions (bottom) defined with respect to  $\Delta\phi$ .

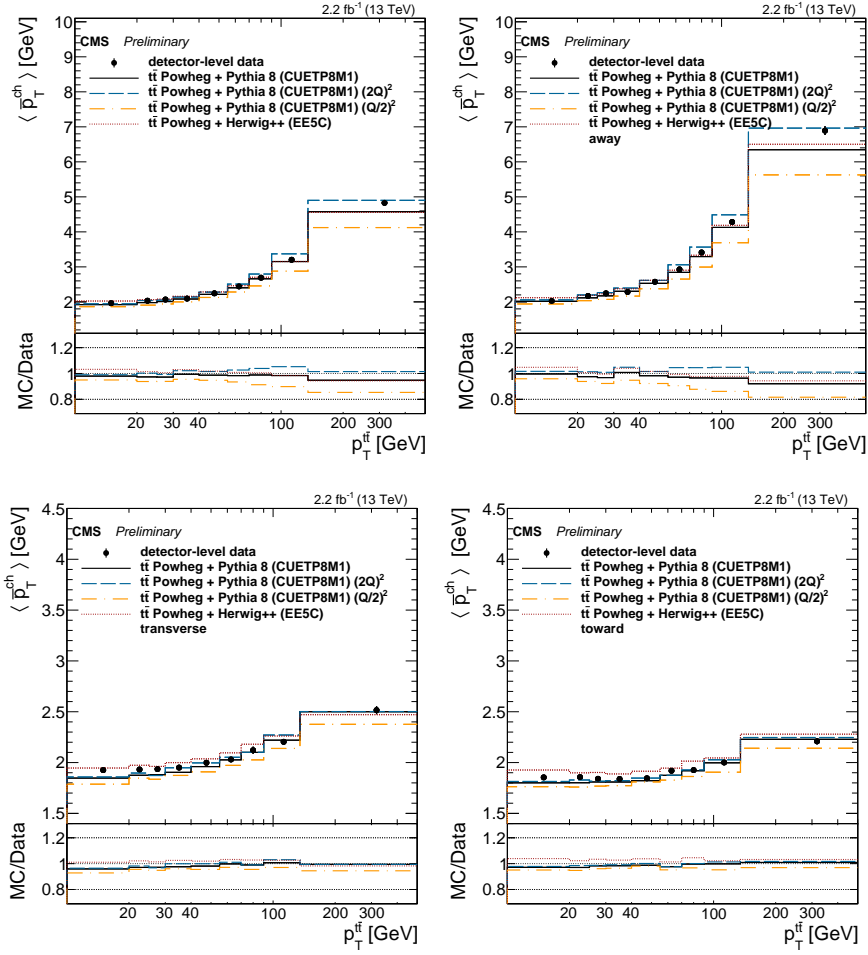


Figure 4.40: The average  $p_T$  per charged particle vs  $p_T^{\text{tt}}$  for the overall sample and the away (top), transverse and toward regions (bottom) defined with respect to  $\Delta\phi$ .

## CHAPTER 5

### CONCLUSIONS

#### 5.1 Discussion of Physics Results

Two different measurements, involving the production of two of the heaviest particles of the SM periodic table, Z boson and the top quark, are presented in this thesis.

In the Z + jet analysis, multiple cross section measurements of production cross section is carried out with respect to several kinematic and angular variables. The measurements provide a stringent test of the state-of-the-art simulations. It has been observed that most of the kinematic variables are described well by the predictions, except tree level MADGRAPH 5 + PYTHIA 6 prediction failing to describe leading jet  $p_T$  spectra. This feature has been confirmed previously by CMS and ATLAS measurements (ATLAS using ALPGEN+ PYTHIA, which provides similar QCD calculation order). It has been found that adding NLO effects to the fixed order calculations improve the description of the measurements. Also, it is seen that correlations between objects when looking into multidimensional cross sections is poorly described, but greatly improved with fixed-order NLO calculations.

In the second analysis, UE is studied associated with  $t\bar{t}$  events. Different tunes have been tested against the measurements. The universality of UE tunes have been proven by showing their validity in the top quark pair production scale. Choice of QCD scale is also tested against the data and slight preference is observed towards scale-up choice. In both analyses, validity of several tunes (CUTP8M1, Z2\*, EE5C ...) has been verified against the CMS data.

Overall, the validity of SM predictions obtained from several fixed-order calculations using various programs is verified against the CMS measurements with the given uncertainties. There are some corners of phase-space that is not very well described by some of the predictions, where the agreement is highly improved with improvements in the simulation techniques.

## 5.2 Summary

The Standard Model of particle physics is still the only theory that is verified by the experiments, and gives a complete explanation of the observations, as also shown in the measurements presented in this thesis. The measurements presented in this thesis also adds confidence to our understanding and modelling of nature as discussed.

The results obtained here are published by the CMS collaboration in Refs [11, 21], and they provide valuable input to the theory world, in terms of improving the Monte-Carlo simulations. The Z + jet analysis cross section values and systematic uncertainties will be published in HepDATA platform [99].

The LHC had a very successful data taking periods, and as illustrated here the machine is expected to serve collisions with increasing luminosities for another two decades. The detectors are coping with these developments by upgrading necessary pieces. With increasing statistics and new detectors, the precision of such measurements is expected to increase, testing the Standard Model more stringently, either proving its validity furthermore, or giving hints towards theories Beyond the Standard Model. Such measurements will be of high importance with higher precision for the following LHC periods. The precision will increase firstly because of statistics, but also with improvements in the experimental uncertainties that can be achieved by upgrades of the detector parts and by developing new analysis techniques where the uncertainties cancel out.

## REFERENCES

- [1] “Electron identification criteria.” <https://twiki.cern.ch/twiki/bin/view/CMSPublic/SWGuideElectronID>. Accessed: 03-06-2017.
- [2] G. A. et. al., “Observation of a new particle in the search for the standard model higgs boson with the ATLAS detector at the LHC,” *Physics Letters B*, vol. 716, no. 1, pp. 1 – 29, 2012.
- [3] S. C. et. al, “Observation of a new boson at a mass of 125 gev with the CMS experiment at the LHC,” *Physics Letters B*, vol. 716, no. 1, pp. 30 – 61, 2012.
- [4] “Summaries of CMS cross section measurements.” <https://twiki.cern.ch/twiki/bin/view/CMSPublic/PhysicsResultsCombined/>. Accessed: 03-06-2017.
- [5] T. Aaltonen *et al.*, “Measurement of Inclusive Jet Cross Sections in  $Z/\gamma^* \rightarrow e^+e^- + \text{jets}$  Production in  $p\bar{p}$  Collisions at  $\sqrt{s} = 1.96$  TeV,” *Phys. Rev. Lett.*, vol. 100, p. 102001, 2008.
- [6] V. M. Abazov *et al.*, “Measurement of differential  $Z/\gamma^* + \text{jet} + X$  cross sections in  $p\bar{p}$  collisions at  $\sqrt{s} = 1.96$  TeV,” *Phys. Lett. B*, vol. 669, p. 278, 2008.
- [7] G. Aad *et al.*, “Measurement of the production cross section of jets in association with a Z boson in pp collisions at  $\sqrt{s} = 7$  TeV with the ATLAS detector,” *JHEP*, vol. 07, p. 032, 2013.
- [8] G. Aad *et al.*, “Measurement of the production cross section for  $z/\gamma^*$  in association with jets in pp collisions at  $\sqrt{s} = 7$  TeV with the ATLAS detector,” *Phys. Rev. D*, vol. 85, p. 032009, 2012.
- [9] S. Chatrchyan *et al.*, “Jet production rates in association with W and Z bosons in pp collisions at  $\sqrt{s} = 7$  TeV,” *JHEP*, vol. 01, p. 010, 2012.
- [10] V. Khachatryan *et al.*, “Measurements of jet multiplicity and differential production cross sections of Z+ jets events in proton-proton collisions at  $\sqrt{s} = 7$  TeV,” *Phys. Rev. D*, vol. 91, p. 052008, 2015.
- [11] V. Khachatryan *et al.*, “Measurements of differential production cross sections for a Z boson in association with jets in pp collisions at  $\sqrt{s} = 8$  TeV,” *JHEP*, vol. 04, p. 022, 2017.

- [12] M. Aaboud *et al.*, “Measurements of the production cross section of a  $Z$  boson in association with jets in pp collisions at  $\sqrt{s} = 13$  TeV with the ATLAS detector,” *Eur. Phys. J.*, vol. C77, no. 6, p. 361, 2017.
- [13] CMS Collaboration, “Measurement of the differential cross section of  $Z$  boson production in association with jets in proton-proton collisions at  $\sqrt{s} = 13$  TeV,” CMS Physics Analysis Summary CMS-PAS-SMP-15-010, 2015.
- [14] V. Khachatryan *et al.*, “First Measurement of the Underlying Event Activity at the LHC with  $\sqrt{s} = 0.9$  TeV,” *Eur. Phys. J.*, vol. C70, pp. 555–572, 2010.
- [15] V. Khachatryan *et al.*, “Strange Particle Production in  $pp$  Collisions at  $\sqrt{s} = 0.9$  and 7 TeV,” *JHEP*, vol. 05, p. 064, 2011.
- [16] S. Chatrchyan *et al.*, “Measurement of the underlying event activity in  $pp$  collisions at  $\sqrt{s} = 0.9$  and 7 TeV with the novel jet-area/median approach,” *JHEP*, vol. 08, p. 130, 2012.
- [17] S. Chatrchyan *et al.*, “Jet and underlying event properties as a function of charged-particle multiplicity in proton–proton collisions at  $\sqrt{s} = 7$  TeV,” *Eur. Phys. J.*, vol. C73, no. 12, p. 2674, 2013.
- [18] S. Chatrchyan *et al.*, “Study of the underlying event at forward rapidity in pp collisions at  $\sqrt{s} = 0.9, 2.76$ , and 7 TeV,” *JHEP*, vol. 04, p. 072, 2013.
- [19] CMS Collaboration, “Study of the inclusive production of charged pions, kaons, and protons in pp collisions at  $\sqrt{s} = 0.9, 2.76$ , and 7 tev,” *Eur.Phys.J.C*, vol. 72, p. 2164, 2012.
- [20] CMS Collaboration, “Study of the underlying event, b-quark fragmentation and hadronization properties in  $t\bar{t}$  events,” CMS Physics Analysis Summary CMS-PAS-TOP-13-007, 2013.
- [21] CMS Collaboration, “Underlying event measurement with  $t\bar{t} + X$  events with p-p collision data at  $\sqrt{s}=13$  TeV,” CMS Physics Analysis Summary CMS-PAS-TOP-15-017, CERN, Geneva, 2015.
- [22] T. Gleisberg, S. Hoeche, F. Krauss, A. Schalicke, S. Schumann, and J.-C. Winter, “SHERPA 1. alpha: A Proof of concept version,” *JHEP*, vol. 02, p. 056, 2004.
- [23] D. Griffiths, *Introduction to Elementary Particles*. 2008.
- [24] D. H. Perkins, *Introduction to High Energy Physics*. 2000.
- [25] C. L. Cowan, F. Reines, F. B. Harrison, H. W. Kruse, and A. D. McGuire, “Detection of the free neutrino: a confirmation,” *Science*, vol. 124, no. 3212, pp. 103–104, 1956.

- [26] V. Khachatryan *et al.*, “Measurement of the inclusive 3-jet production differential cross section in proton-proton collisions at 7 TeV and determination of the strong coupling constant in the TeV range,” *Eur. Phys. J.*, vol. C75, no. 5, p. 186, 2015.
- [27] G. Altarelli and G. Parisi, “Asymptotic Freedom in Parton Language,” *Nucl. Phys.*, vol. B126, pp. 298–318, 1977.
- [28] R. D. Ball *et al.*, “Parton distributions for the LHC run II,” *JHEP*, vol. 04, p. 040, 2015.
- [29] J. Gao, M. Guzzi, J. Huston, H.-L. Lai, Z. Li, P. Nadolsky, J. Pumplin, D. Stump, and C. P. Yuan, “CT10 next-to-next-to-leading order global analysis of QCD,” *Phys. Rev. D*, vol. 89, p. 033009, 2014.
- [30] A. M. Cooper-Sarkar, “PDF Fits at HERA,” *PoS*, vol. EPS-HEP2011, p. 320, 2011.
- [31] W. Tung, “Bjorken scaling,” *Scholarpedia*, vol. 4, no. 3, p. 7412, 2009. revision #91065.
- [32] S. Weinzierl, “Introduction to Monte Carlo methods.” hep-ph/0006269, 2000.
- [33] Buckley, Andy *et al.*, “LHAPDF6: parton density access in the LHC precision era,” *Eur. Phys. J.*, vol. C75, p. 132, 2015.
- [34] J. Alwall, M. Herquet, F. Maltoni, O. Mattelaer, and T. Stelzer, “MadGraph 5: Going Beyond,” *JHEP*, vol. 06, p. 128, 2011.
- [35] H. Murayama, I. Watanabe, and K. Hagiwara, “HELAS: HELicity amplitude subroutines for Feynman diagram evaluations.” KEK-91-11, 1992.
- [36] F. Maltoni and T. Stelzer, “MadEvent: Automatic event generation with MadGraph,” *JHEP*, vol. 02, p. 027, 2003.
- [37] J. Alwall, R. Frederix, S. Frixione, V. Hirschi, F. Maltoni, O. Mattelaer, H.-S. Shao, T. Stelzer, P. Torielli, and M. Zaro, “The automated computation of tree-level and next-to-leading order differential cross sections, and their matching to parton shower simulations,” *JHEP*, vol. 07, p. 079, 2014.
- [38] P. Nason, “A New method for combining NLO QCD with shower Monte Carlo algorithms,” *JHEP*, vol. 11, p. 040, 2004.
- [39] S. Frixione, P. Nason, and C. Oleari, “Matching NLO QCD computations with Parton Shower simulations: the POWHEG method,” *JHEP*, vol. 11, p. 070, 2007.
- [40] S. Alioli, P. Nason, C. Oleari, and E. Re, “A general framework for implementing NLO calculations in shower Monte Carlo programs: the POWHEG BOX ,” *JHEP*, vol. 06, p. 043, 2010.

- [41] T. Gleisberg, S. Höche, F. Krauss, M. Schönherr, S. Schumann, F. Siegert, and J. Winter, “Event generation with SHERPA 1.1,” *JHEP*, vol. 02, p. 007, 2009.
- [42] C. F. Berger, Z. Bern, L. J. Dixon, F. Febres Cordero, D. Forde, H. Ita, D. A. Kosower, and Maître, “One-loop calculations with BlackHat,” *Nucl. Phys. Proc. Suppl.*, vol. 183, p. 313, 2008.
- [43] C. F. Berger, Z. Bern, L. J. Dixon, F. Febres Cordero, D. Forde, T. Gleisbert, H. Ita, D. A. Kosower, and D. Maître, “Vector Boson + Jets with BlackHat and SHERPA,” in *Loops and Legs in Quantum Field Theory — Proceedings of the 10th DESY Workshop on Elementary Particle Theory*, 2010. Nucl. Phys. B - Proceedings Supplements, 205-206 (2010) 92.
- [44] T. Sjöstrand, S. Mrenna, and P. Z. Skands, “PYTHIA 6.4 physics and manual,” *JHEP*, vol. 05, p. 026, 2006.
- [45] T. Sjostrand, S. Mrenna, and P. Z. Skands, “A Brief Introduction to PYTHIA 8.1,” *Comput. Phys. Commun.*, vol. 178, pp. 852–867, 2008.
- [46] B. Andersson, G. Gustafson, G. Ingelman, and T. Sjöstrand, “Parton fragmentation and string dynamics,” *Physics Reports*, vol. 97, no. 2, pp. 31 – 145, 1983.
- [47] “Lund-string model.” [https://www.reddit.com/r/ScienceImages/comments/3gbn9s/the\\_hadronization\\_of\\_qcd\\_partons\\_quarks\\_gluons/](https://www.reddit.com/r/ScienceImages/comments/3gbn9s/the_hadronization_of_qcd_partons_quarks_gluons/). Accessed: 03-06-2017.
- [48] M. Bahr *et al.*, “Herwig++ Physics and Manual,” *Eur.Phys.J.C*, vol. 58, p. 639, 2008.
- [49] J. Pumplin, D. R. Stump, J. Huston, H.-L. Lai, P. Nadolsky, and W.-K. Tung, “New generation of parton distributions with uncertainties from global QCD analysis,” *JHEP*, vol. 07, p. 012, 2002.
- [50] V. Khachatryan *et al.*, “Event generator tunes obtained from underlying event and multiparton scattering measurements,” *Eur. Phys. J.*, vol. C76, no. 3, p. 155, 2016.
- [51] P. Skands, S. Carrazza and J. Rojo, “Tuning PYTHIA 8.1: the Monash 2013 Tune,” *Eur. Phys. J. C*, vol. 74, p. 3024, 2014.
- [52] R. D. Ball, L. Del Debbio, S. Forte, A. Guffanti, J. I. Latorre, J. Rojo, and M. Ubiali, “A first unbiased global NLO determination of parton distributions and their uncertainties,” *Nucl. Phys. B*, vol. 838, p. 136, 2010.
- [53] R. D. Ball, V. Bertone, F. Cerutti, L. Del Debbio, S. Forte, A. Guffanti, J. I. Latorre, J. Rojo, and M. Ubiali, “Impact of heavy quark masses on parton distributions and LHC phenomenology,” *Nucl. Phys. B*, vol. 849, p. 296, 2011.



- [54] Particle Data Group, K. A. Olive, *et al.*, “Review of Particle Physics,” *Chin. Phys. C*, vol. 38, p. 090001, 2014.
- [55] R. Gavin, Y. Li, F. Petriello, and S. Quackenbush, “FEWZ 2.0: A code for hadronic Z production at next-to-next-to-leading order,” *Comput. Phys. Commun.*, vol. 182, p. 2388, 2011.
- [56] M. H. Seymour and A. Siodmok, “Constraining MPI models using  $\sigma_{eff}$  and recent Tevatron and LHC Underlying Event data,” *JHEP*, vol. 10, p. 113, 2013.
- [57] O. S. Bruning, P. Collier, P. Lebrun, S. Myers, R. Ostojic, J. Poole, and P. Proudlock, *LHC Design Report*. CERN Yellow Reports: Monographs, Geneva: CERN, 2004.
- [58] “The position of LHC tunnel and the experiments.” <https://alexeinstein.files.wordpress.com/2014/10/lhc.jpg>. Accessed: 03-06-2017.
- [59] G. Aad *et al.*, “The ATLAS Experiment at the CERN Large Hadron Collider,” *JINST*, vol. 3, p. S08003, 2008.
- [60] S. Chatrchyan *et al.*, “The CMS Experiment at the CERN LHC,” *JINST*, vol. 3, p. S08004, 2008.
- [61] A. A. Alves, Jr. *et al.*, “The LHCb Detector at the LHC,” *JINST*, vol. 3, p. S08005, 2008.
- [62] K. Aamodt *et al.*, “The ALICE experiment at the CERN LHC,” *JINST*, vol. 3, p. S08002, 2008.
- [63] O. Adriani *et al.*, “The LHCf detector at the CERN Large Hadron Collider,” *JINST*, vol. 3, p. S08006, 2008.
- [64] G. Anelli *et al.*, “The TOTEM experiment at the CERN Large Hadron Collider,” *JINST*, vol. 3, p. S08007, 2008.
- [65] J. L. Pinfold, “The MoEDAL Experiment at the LHC ? a New Light on the Terascale Frontier,” *J. Phys. Conf. Ser.*, vol. 631, no. 1, p. 012014, 2015.
- [66] C. De Melis, “The CERN accelerator complex. Complexe des accélérateurs du CERN,” Jul 2016. General Photo, <https://cds.cern.ch/record/2197559>.
- [67] W. Herr and B. Muratori, “Concept of luminosity.” <https://cds.cern.ch/record/941318>, 2006.
- [68] “Public CMS Luminosity Information.” <https://twiki.cern.ch/twiki/bin/view/CMSPublic/LumiPublicResults>. Accessed: 03-06-2017.

- [69] “LHC Timeline.” [http://emetral.web.cern.ch/emetral/LHC%20schedule%202015-2034%20FkBordry%202-december-2013\[1\].pdf](http://emetral.web.cern.ch/emetral/LHC%20schedule%202015-2034%20FkBordry%202-december-2013[1].pdf). Accessed: 15-05-2017.
- [70] “CMS detector figures.” <https://cms.cern/detector>. Accessed: 03-06-2017.
- [71] C. Collaboration, “Technical proposal for the upgrade of the CMS detector through 2020,” Tech. Rep. CERN-LHCC-2011-006. LHCC-P-004, Jun 2011.
- [72] V. Karimaki, M. Mannelli, P. Siegrist, H. Breuker, A. Caner, R. Castaldi, K. Freudenreich, G. Hall, R. Horisberger, M. Huhtinen, and A. Cattai, *The CMS tracker system project: Technical Design Report*. Technical Design Report CMS, Geneva: CERN, 1997.
- [73] C. Collaboration, *The CMS electromagnetic calorimeter project: Technical Design Report*. Technical Design Report CMS, Geneva: CERN, 1997.
- [74] C. Collaboration, *The CMS hadron calorimeter project: Technical Design Report*. Technical Design Report CMS, Geneva: CERN, 1997.
- [75] G. Bayatian *et al.*, “Design, performance and calibration of the CMS forward calorimeter wedges,” *Eur. Phys. J.*, vol. C53, pp. 139–166, 2008.
- [76] G. Acquistapace *et al.*, “CMS, the magnet project: Technical design report,” 1997.
- [77] C. Collaboration, *The CMS muon project: Technical Design Report*. Technical Design Report CMS, Geneva: CERN, 1997.
- [78] S. Dasu *et al.*, “CMS. The TriDAS project. Technical design report, vol. 1: The trigger systems,” 2000.
- [79] “CMS Data Formats and Data Tiers.” <https://twiki.cern.ch/twiki/bin/view/CMSPublic/WorkBookDataFormats>. Accessed: 03-06-2017.
- [80] S. Agostinelli *et al.*, “GEANT4—a simulation toolkit,” *Nucl. Instrum. Meth. A*, vol. 506, p. 250, 2003.
- [81] G. Petrucciani, A. Rizzi, and C. Vuosalo, “Mini-AOD: A New Analysis Data Format for CMS,” *J. Phys. Conf. Ser.*, vol. 664, no. 7, p. 072052, 2015.
- [82] W. Adam, V. Adler, B. Hegner, L. Lista, S. Lowette, P. Maksimovic, G. Petrucciani, S. Rappoccio, F. Ronga, R. Tenchini, and R. Wolf, “PAT: the CMS Physics Analysis Toolkit,” Tech. Rep. CMS-CR-2009-083, CERN, Geneva, May 2009.
- [83] “CMSSW Application Framework.” <https://twiki.cern.ch/twiki/bin/view/CMSPublic/WorkBookCMSSWFramework>. Accessed: 03-06-2017.

- [84] V. Khachatryan *et al.*, “Performance of Electron Reconstruction and Selection with the CMS Detector in Proton-Proton Collisions at  $\sqrt{s}= 8$  TeV,” *JINST*, vol. 10, no. 06, p. P06005, 2015.
- [85] *The CMS muon project: Technical Design Report*. Technical Design Report CMS, Geneva: CERN, 1997.
- [86] A. M. Sirunyan *et al.*, “Particle-flow reconstruction and global event description with the CMS detector,” 2017.
- [87] F. Beaudette, “The CMS Particle Flow Algorithm,” in *Proceedings, International Conference on Calorimetry for the High Energy Frontier (CHEF 2013): Paris, France, April 22-25, 2013*, pp. 295–304, 2013.
- [88] S. Chatrchyan *et al.*, “Description and performance of track and primary-vertex reconstruction with the CMS tracker,” *JINST*, vol. 9, no. 10, p. P10009, 2014.
- [89] M. Cacciari, G. P. Salam, and G. Soyez, “The anti-kt jet clustering algorithm,” *JHEP*, vol. 04, p. 063, 2008.
- [90] “Workbook jet energy corrections.” <https://twiki.cern.ch/twiki/bin/view/CMSPublic/WorkBookJetEnergyCorrections>. Accessed: 03-06-2017.
- [91] “b-tagging 101.” <https://amva4newphysics.wordpress.com/2016/01/04/b-tagging-101/>. Accessed: 03-06-2017.
- [92] “Pileup mc reweighting utilities.” <https://twiki.cern.ch/twiki/bin/viewauth/CMS/PileupMCReweightingUtilities>. Accessed: 03-06-2017.
- [93] G. Cowan, “A survey of unfolding methods for particle physics,” *Conf. Proc.*, vol. C0203181, pp. 248–257, 2002.
- [94] T. Adye, “Unfolding algorithms and tests using RooUnfold,” in *Proceedings, PHYSTAT 2011 Workshop on Statistical Issues Related to Discovery Claims in Search Experiments and Unfolding, CERN, Geneva, Switzerland 17-20 January 2011*, (Geneva), pp. 313–318, CERN, CERN, 2011.
- [95] G. D’Agostini, “A multidimensional unfolding method based on Bayes’ theorem,” *Nucl. Instrum. Meth. A*, vol. 362, p. 487, 1995.
- [96] R. Frederix, S. Frixione, V. Hirschi, F. Maltoni, R. Pittau, and P. Torrielli, “Four-lepton production at hadron colliders: aMC@NLO predictions with theoretical uncertainties,” *JHEP*, vol. 02, p. 099, 2012.
- [97] J. Butterworth *et al.*, “PDF4LHC recommendations for LHC Run II,” *J. Phys.*, vol. G43, p. 023001, 2016.

- [98] A. Leonard, *Measurement of Z boson production in association with jets at the LHC and study of a DAQ system for the Triple-GEM detector in view of the CMS upgrade*. PhD thesis, Universite Libre de Bruxelles, 2015.
- [99] E. Maguire, L. Heinrich, and G. Watt, “HEPData: a repository for high energy physics data,” in *22nd International Conference on Computing in High Energy and Nuclear Physics (CHEP 2016) San Francisco, CA, October 14-16, 2016*, 2017.

## APPENDIX A

### TRIGGER DETAILS FOR BOTH ANALYSES

Further technical details of the trigger paths used in the analyses are given in this section. The trigger path names used in both analyses are given in the table below.

TableA.1: Di-lepton and single-muon triggers used in the analyses.

Electron	HLT_Ele17_CaloIdT_CaloIsoVL_TrkIdVL_TrkIsoVL_Ele8_CaloIdT_CaloIsoVL_TrkIdVL_TrkIsoVL_v*
Muon	HLT_Mu17_Mu8_v*
Muon	HLT_Mu20_v*

The selection criteria applied at trigger level on the electrons are given in the table below.

TableA.2: Identification and isolation criteria using calorimetry and tracker at trigger level for the leading (second leading) electron.

Criteria	Selections
CalIdL	$H/E < 0.15(0.10)$
CalIdL	$\sigma_{i\eta i\eta} < 0.014(0.035)$
CalIdT	$H/E < 0.10(0.075)$
CalIdT	$\sigma_{i\eta i\eta} < 0.011(0.031)$
CalIsoVL	$E\text{CalIso}/E_T < 0.2(0.2)$
CalIsoVL	$H\text{CalIso}/E_T < 0.2(0.2)$
TrkIdVL	$d\eta < 0.01(0.01)$
TrkIdVL	$d\phi < 0.15(0.10)$
TrkIsoVL	$\text{TrkIso}/E_T < 0.2(0.2)$



## APPENDIX B

### UNFOLDING CHECK FOR Z + JET ANALYSIS

Further details regarding the unfolding machinery used in Z + jet analysis are presented in this appendix.

#### B.1 Pull Test for Unfolding

The test is carried out by dividing the inclusive sample into two halves, one half is used to train the unfolding, and the other half is divided into 100 small samples. Each of those are treated as data input and unfolded using the response from the first half. The plots here show the results of the pull distributions. The "pull" is defined as;

$$pull = \frac{unf - gen}{\sigma_{unf}} \quad (B.1)$$

where  $unf$  corresponds to the cross section obtained after unfolding,  $gen$  is the generated cross section value, and  $\sigma_{unf}$  is the statistical uncertainty obtained after unfolding. The figures show the pull distribution for the most populated bins of each rapidity range as well as the sum of all ranges. The mean value is expected to be around zero showing that there is no bias due to the unfolding machinery, and the mean should be one corresponding to correct estimation of statistical uncertainties. As seen in figures below, both expectations are satisfied.

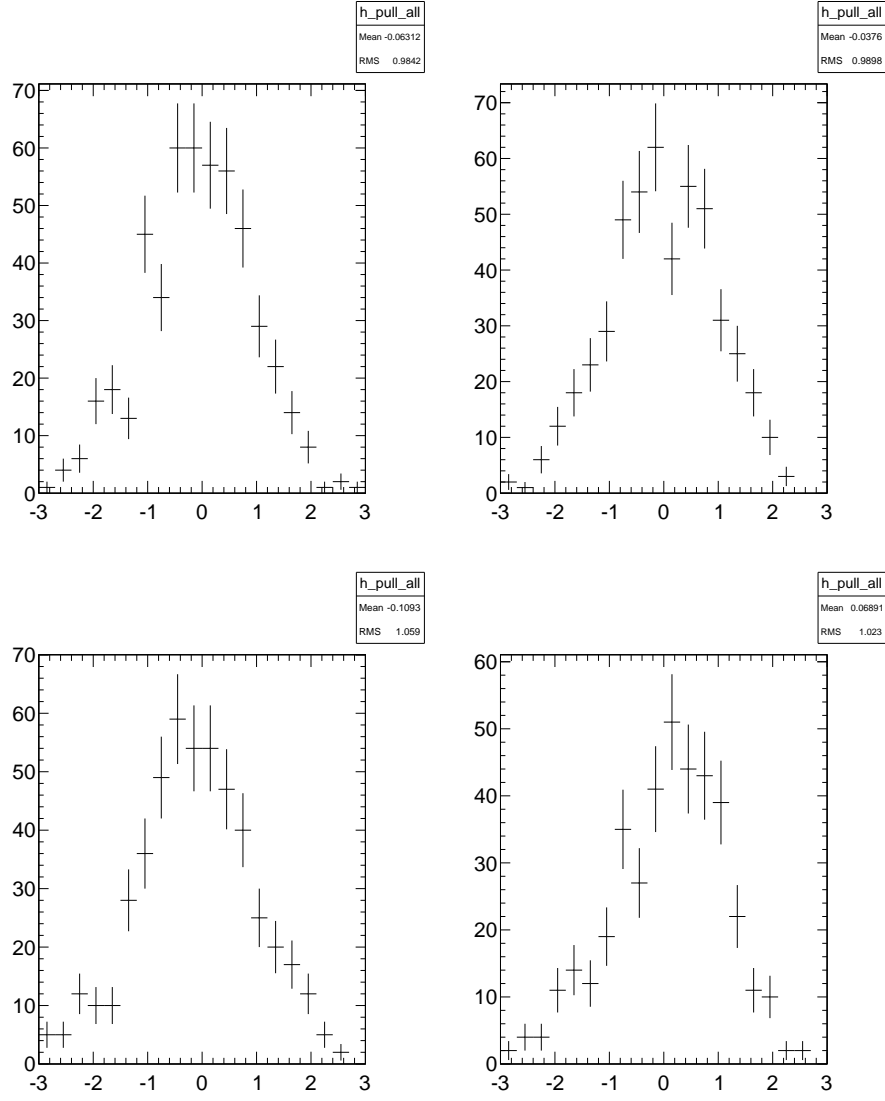


Figure B.1: Pull test for different jet  $y$  ranges.



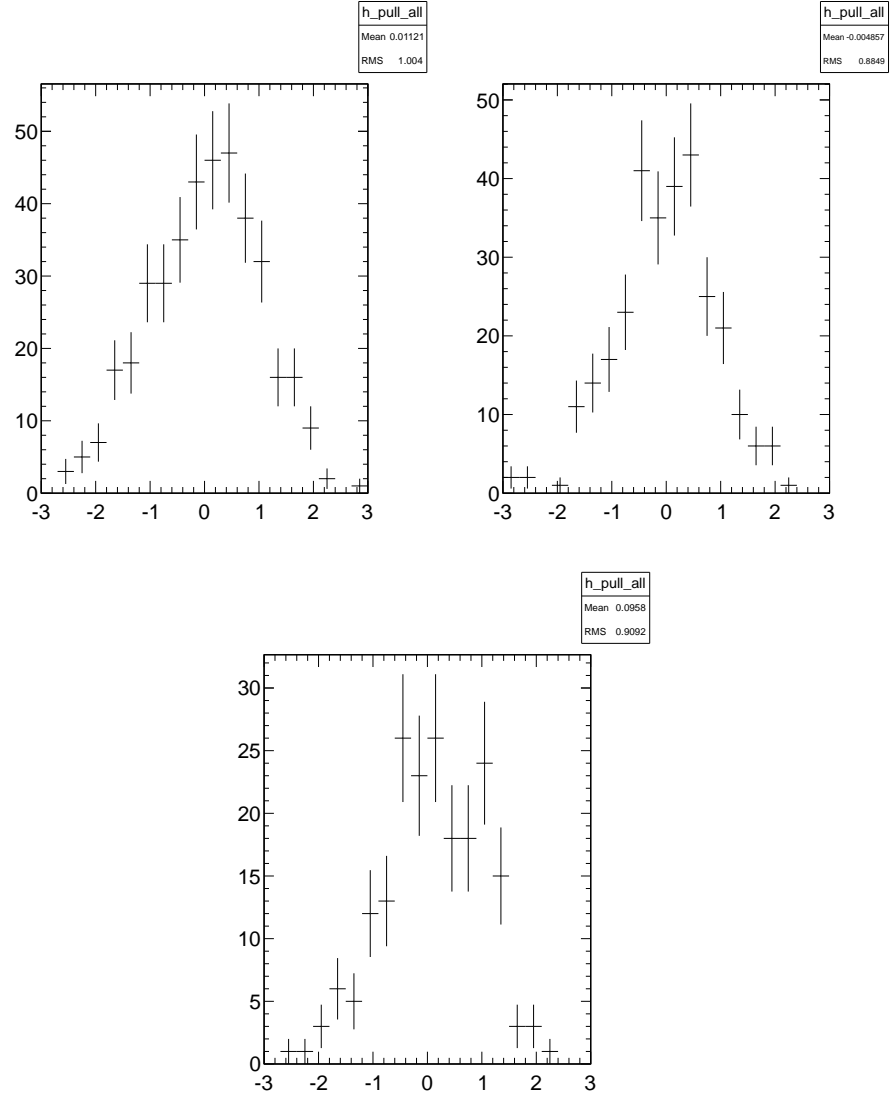


Figure B.2: Pull test for different jet  $y$  ranges.

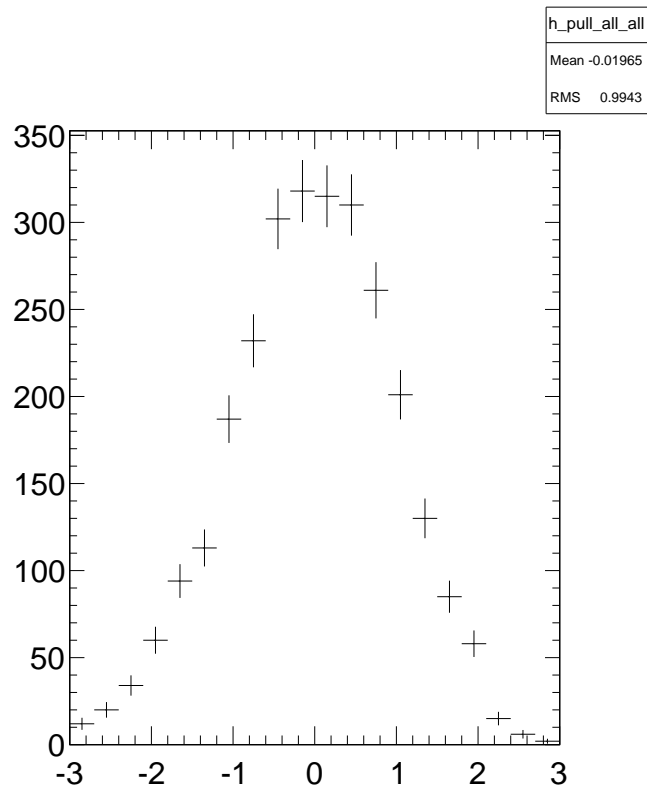


Figure B.3: Pull test for all jet  $y$  ranges combined.

## B.2 Response Matrices of Z + jet Analysis

Response matrices for all the measurements, for each range of kinematical variables are given in the figures below. For the unfolding machinery, the binning of the variables are chosen such that at least 50% of the events are reconstructed in the diagonal. In all figures it is seen that the requirement is fulfilled.

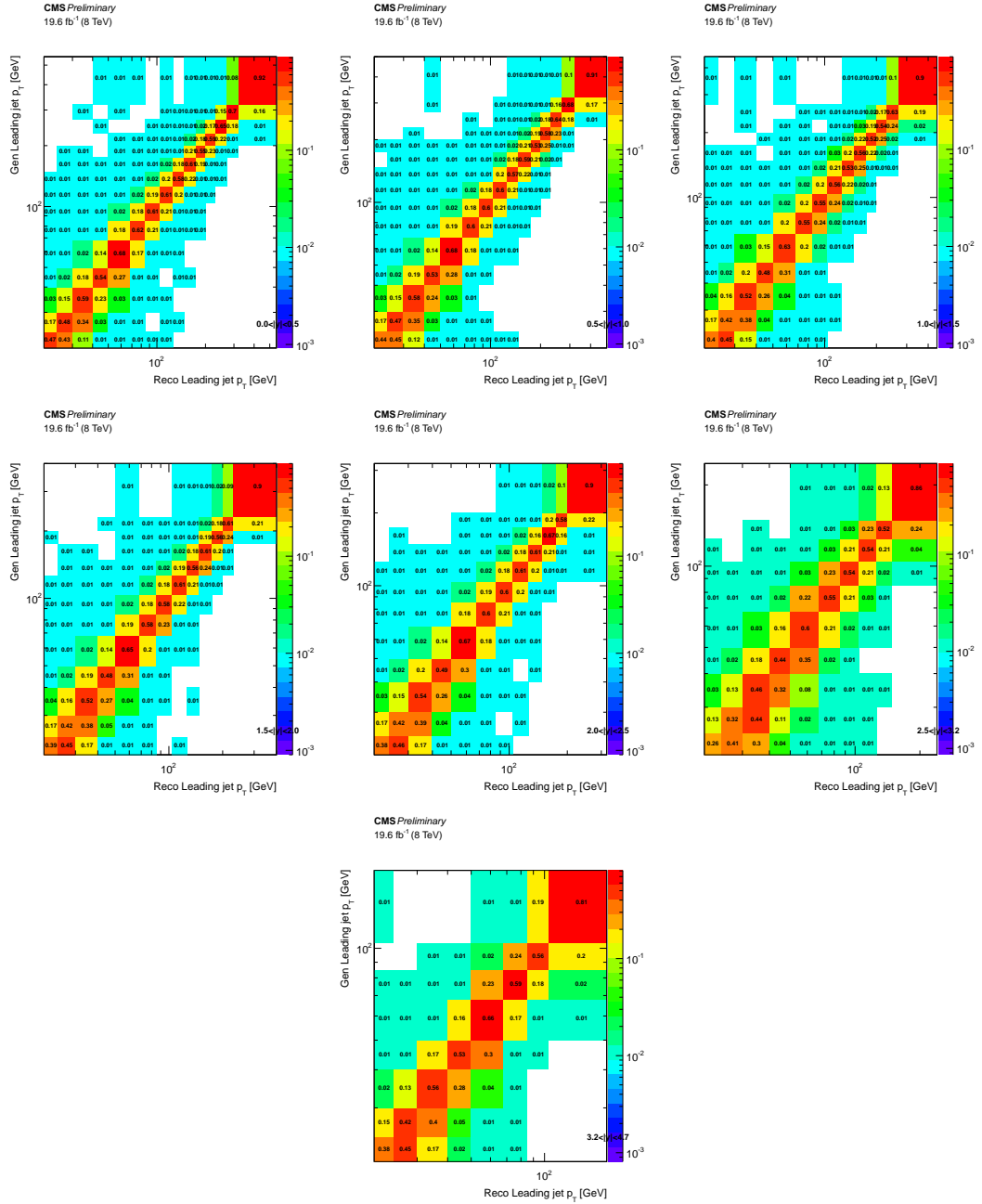


Figure B.4: Response matrices for  $d^2\sigma/dp_T(j_1)dy(j_1)$  in di-electron channel.

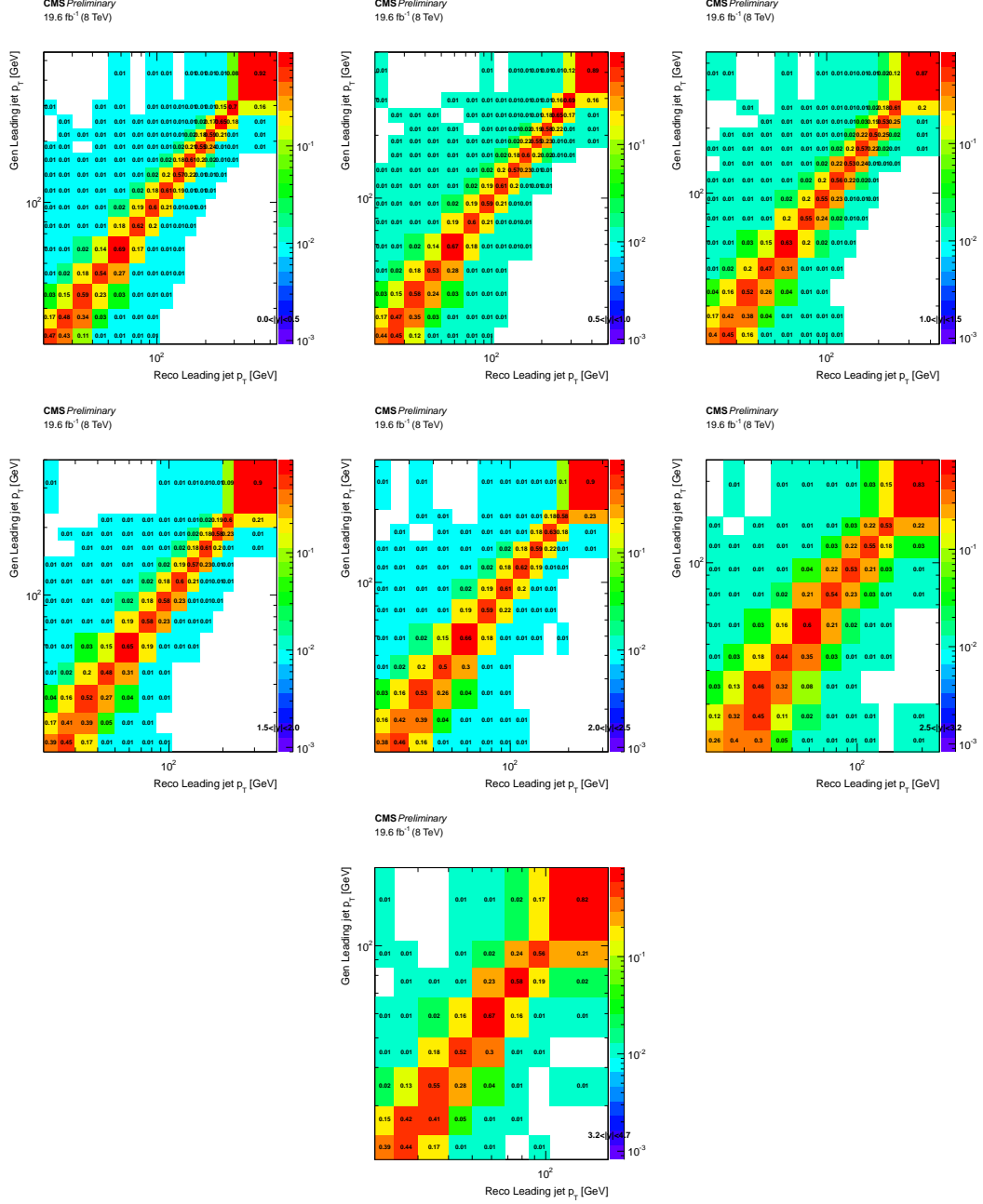


Figure B.5: Response matrices for  $d^2\sigma/dp_T(j_1)dy(j_1)$  in di-muon channel.

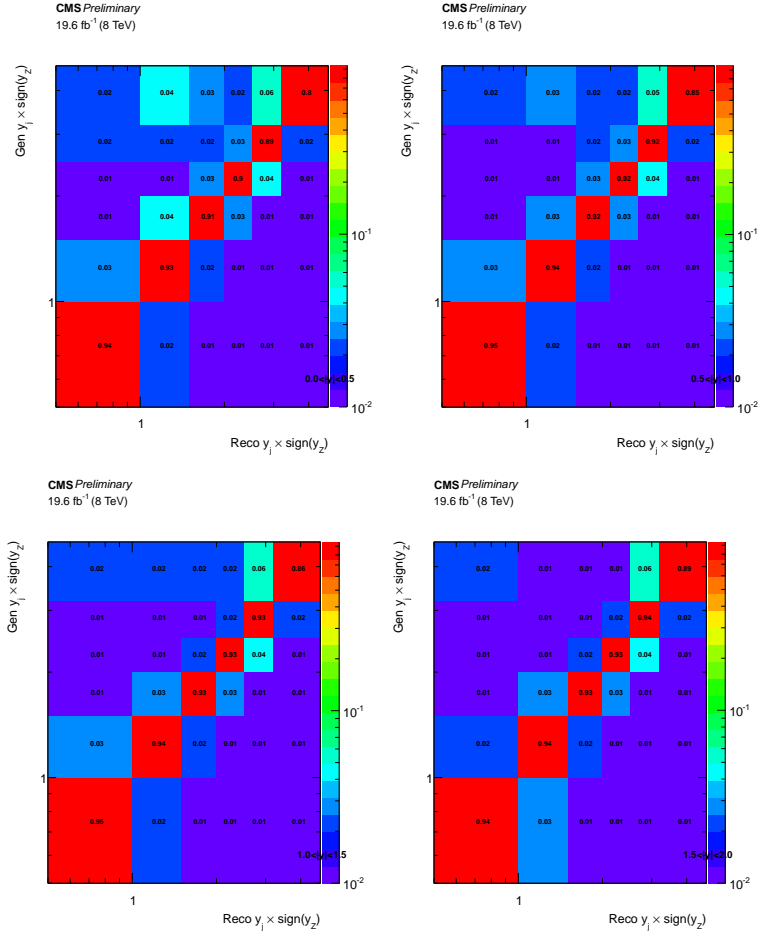


Figure B.6: Response matrices for  $d^2\sigma/dy(Z)dy(j_1)$  in di-electron channel.

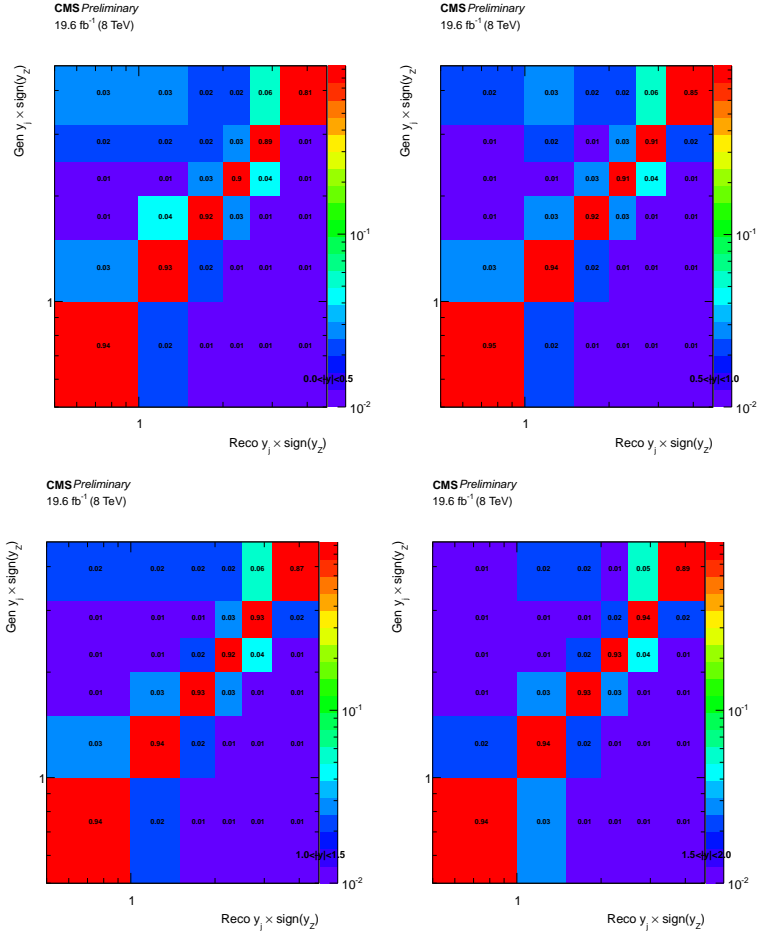


Figure B.7: Response matrices for  $d^2\sigma/dy(Z)dy(j_1)$  in di-muon channel.

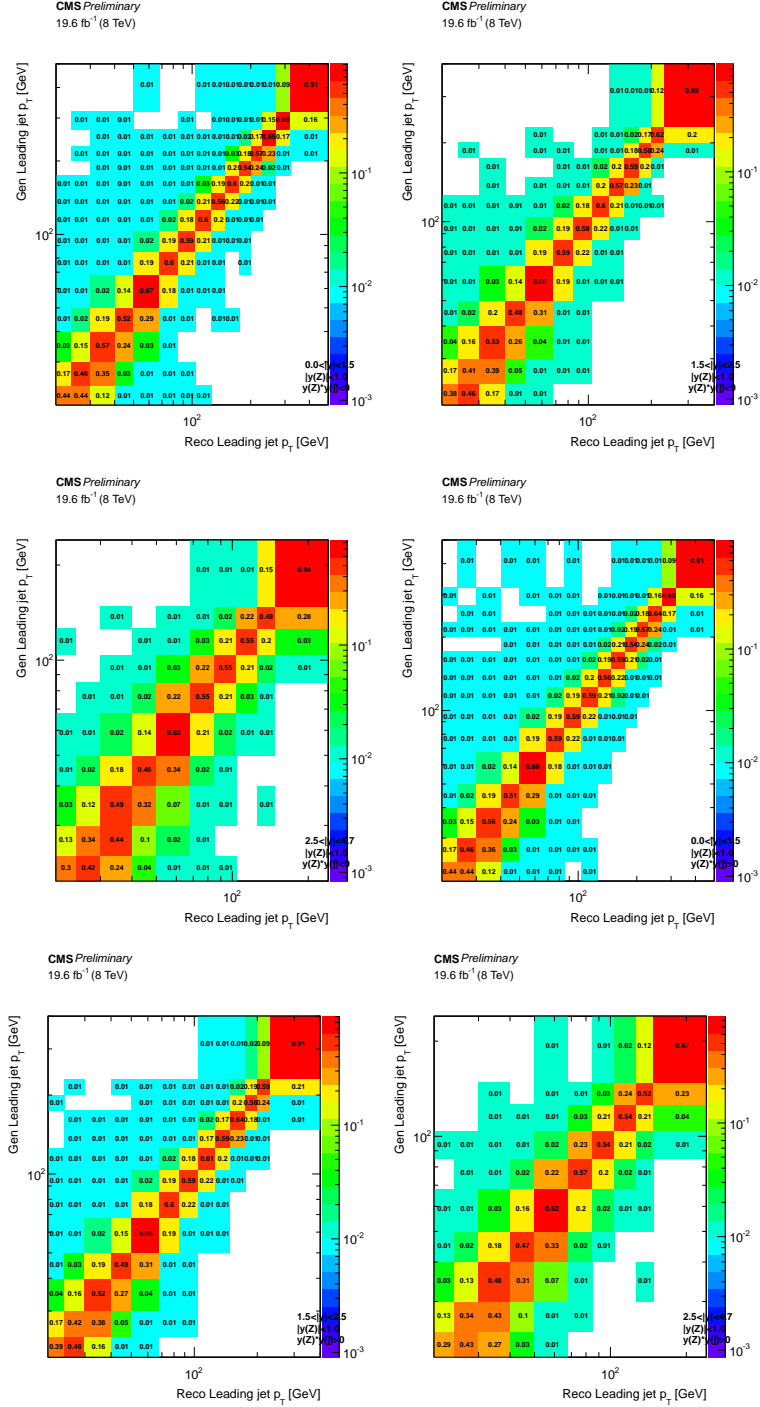


Figure B.8: Response matrices for  $d^3\sigma/dp_T(j_1)dy(j_1)dy(Z)$  in di-electron channel.

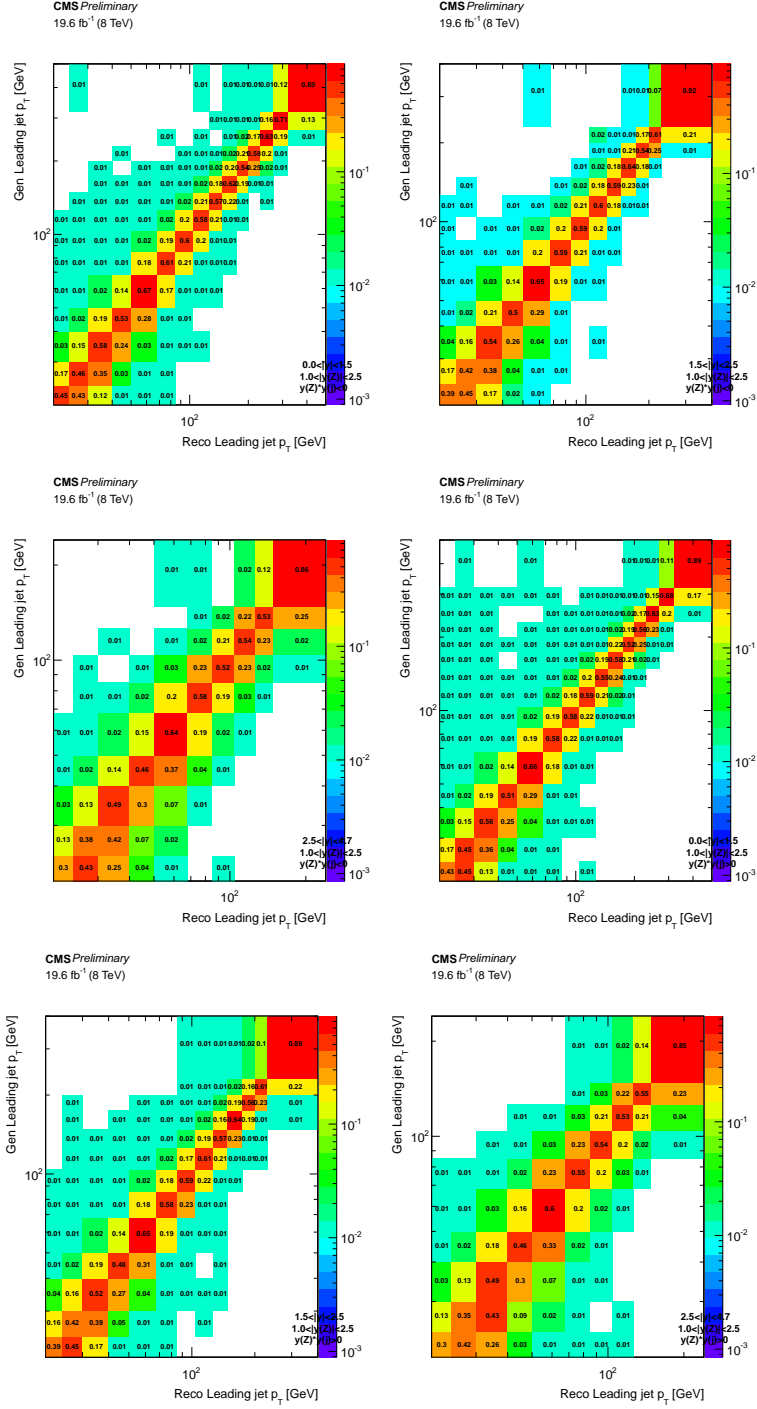


Figure B.9: Response matrices for  $d^3\sigma/dp_T(j_1)dy(j_1)dy(Z)$  in di-electron channel.



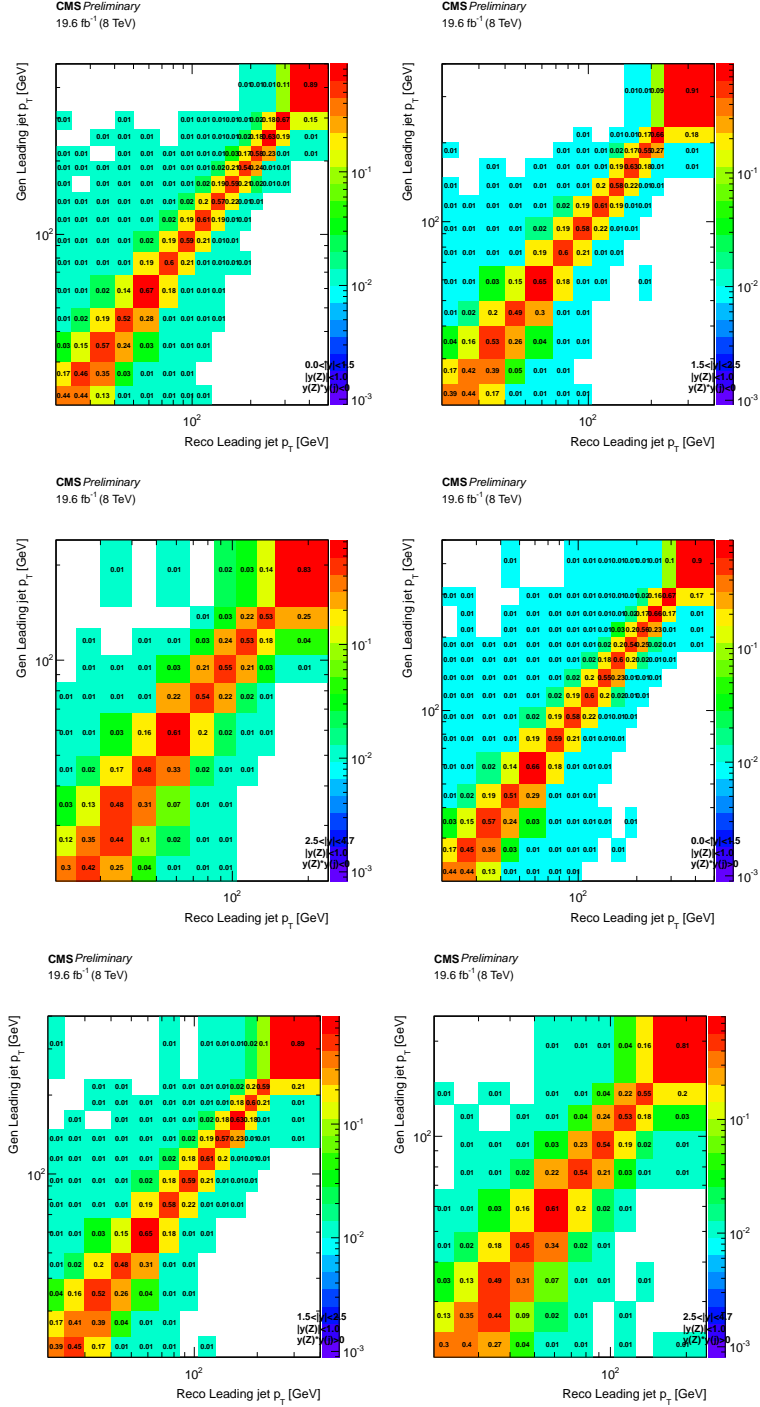


Figure B.10: Response matrices for  $d^3\sigma/dp_T(j_1)dy(j_1)dy(Z)$  in di-muon channel.

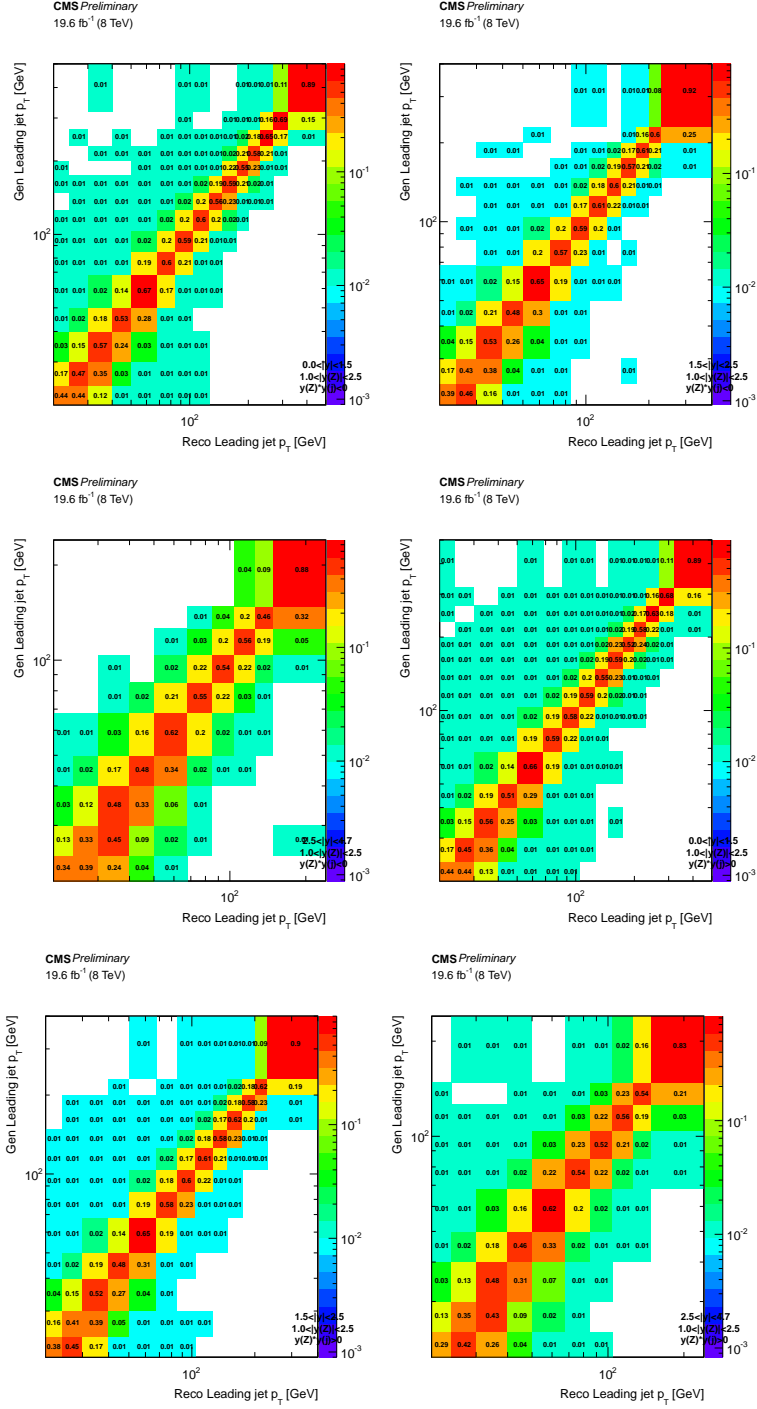


Figure B.11: Response matrices for  $d^3\sigma/dp_T(j_1)dy(j_1)dy(Z)$  in di-muon channel.

## APPENDIX C

### CONTROL OF PU CONTAMINATION IN CENTRAL REGION FOR Z + JET ANALYSIS

The contamination of Pile-Up jets is controlled for the central jets reconstructed in  $|y| < 2.5$ . The figures show the distribution of  $\Delta\phi$  between the jet and the Z boson in all  $y$  ranges and for different  $p_T$  ranges. It is observed that for the central region the PU contamination in the signal region is negligible.

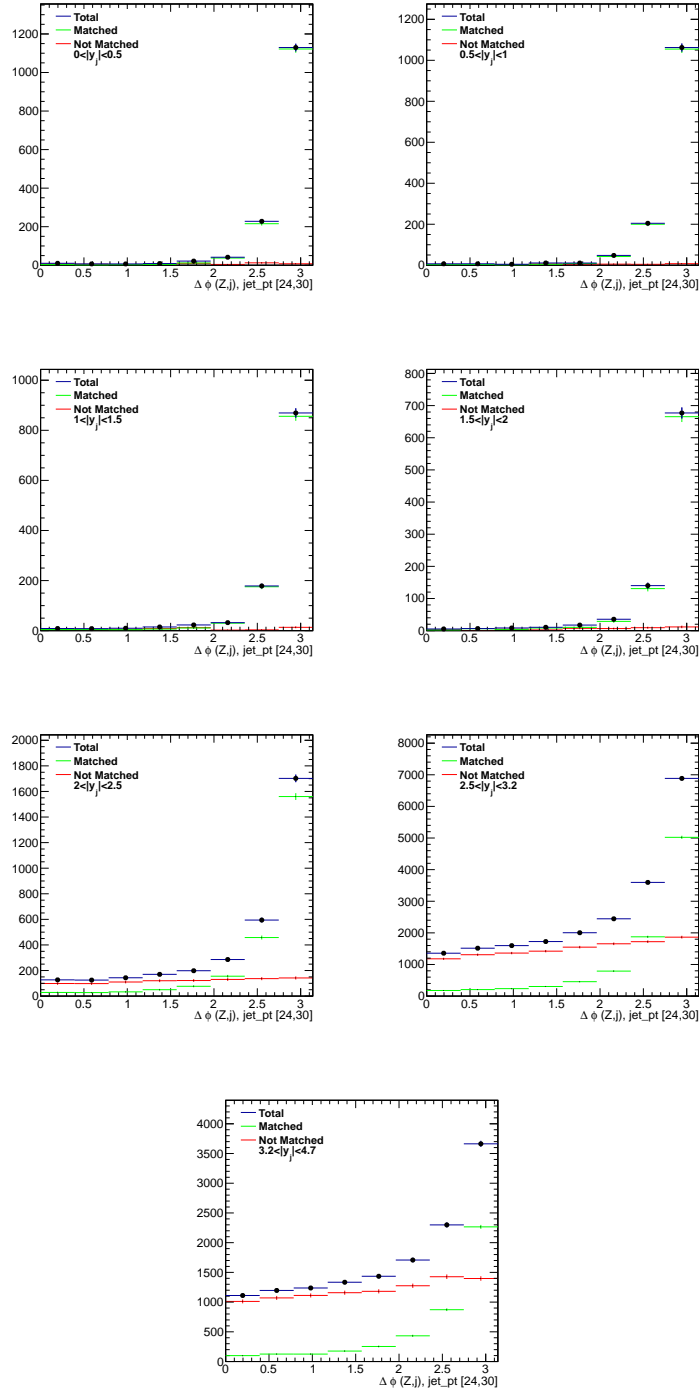


Figure C.1: The azimuthal angle difference distributions between the Z boson and the jet ( $\Delta\phi(Z, j)$ ) for jets with  $p_T[24,30]$  GeV for Z+1j exclusive events. The green (red) lines represent the jets that are matched (not-matched) to a gen jet.

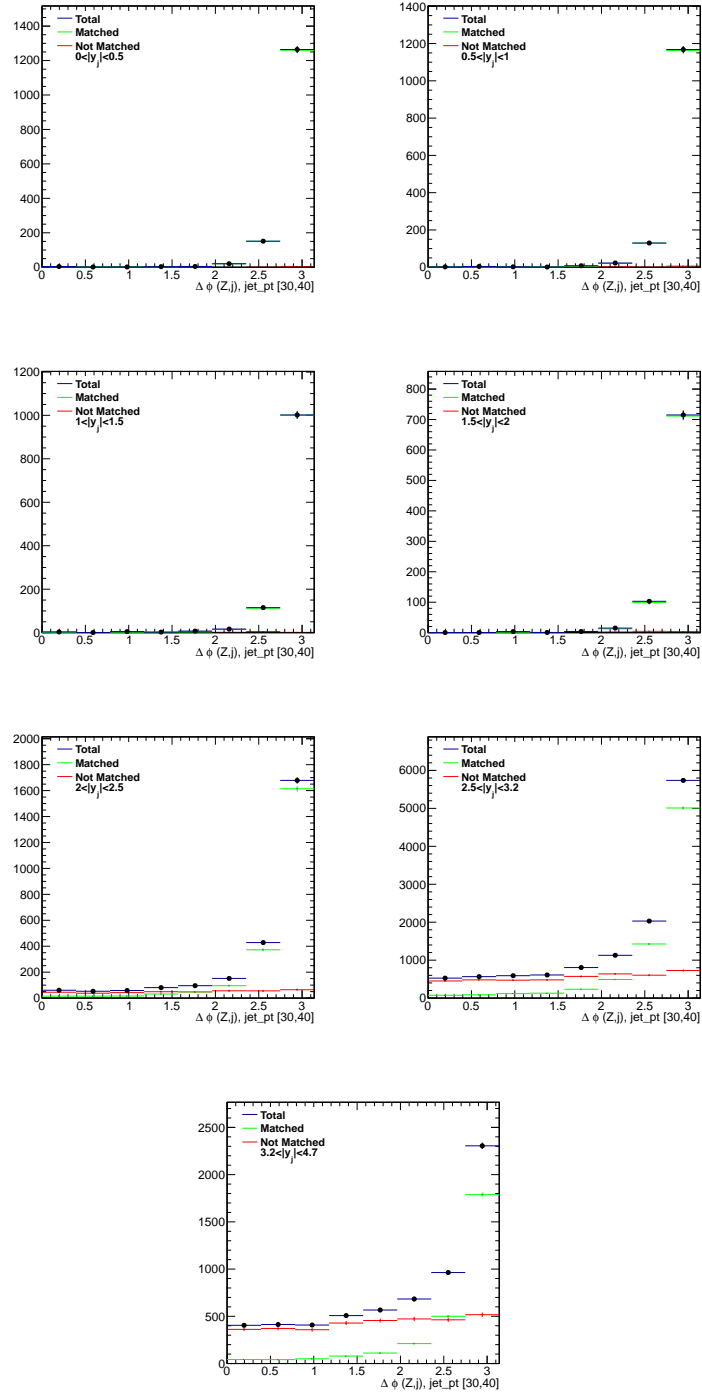


Figure C.2: The azimuthal angle difference distributions between the Z boson and the jet ( $\Delta\phi(Z, j)$ ) for jets with  $p_T[30,40]$  GeV for Z+1j exclusive events. The green (red) lines represent the jets that are matched (not-matched) to a gen jet.

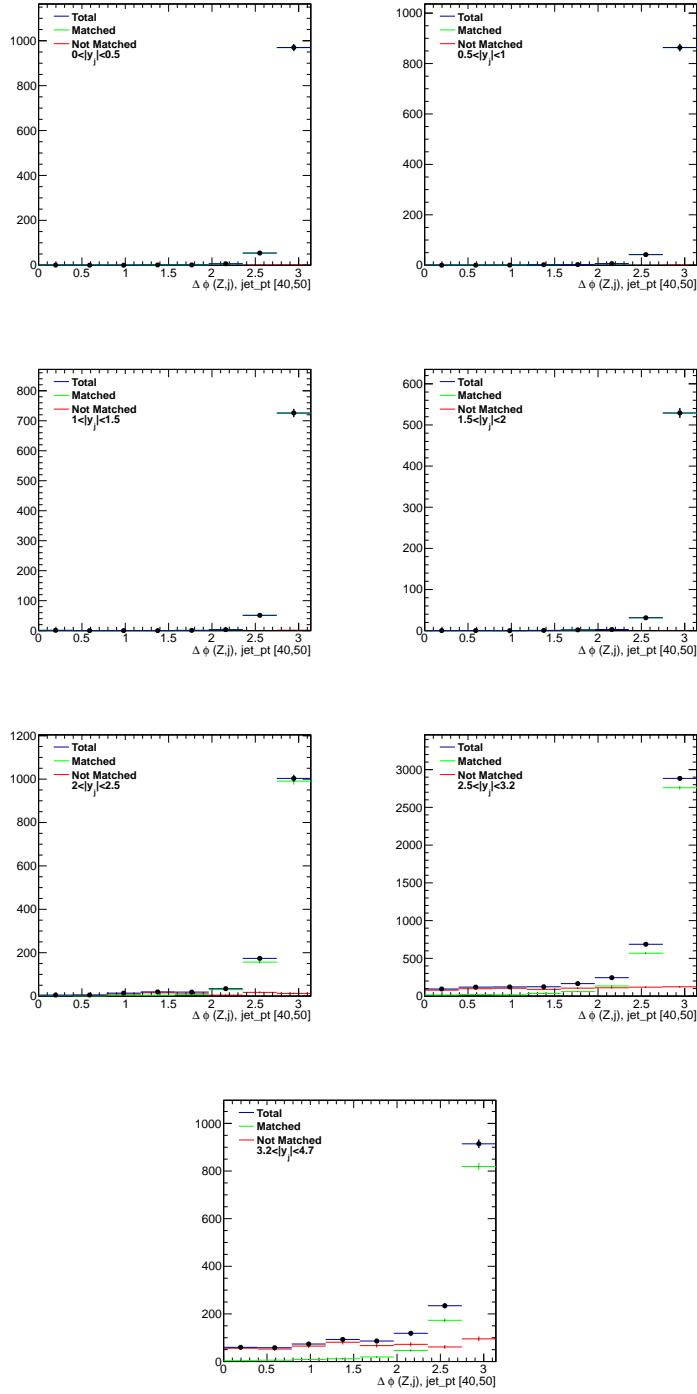


Figure C.3: The azimuthal angle difference distributions between the Z boson and the jet ( $\Delta\phi(Z, j)$ ) for jets with  $p_T[40, 50]$  GeV for Z+1j exclusive events. The green (red) lines represent the jets that are matched (not-matched) to a gen jet.

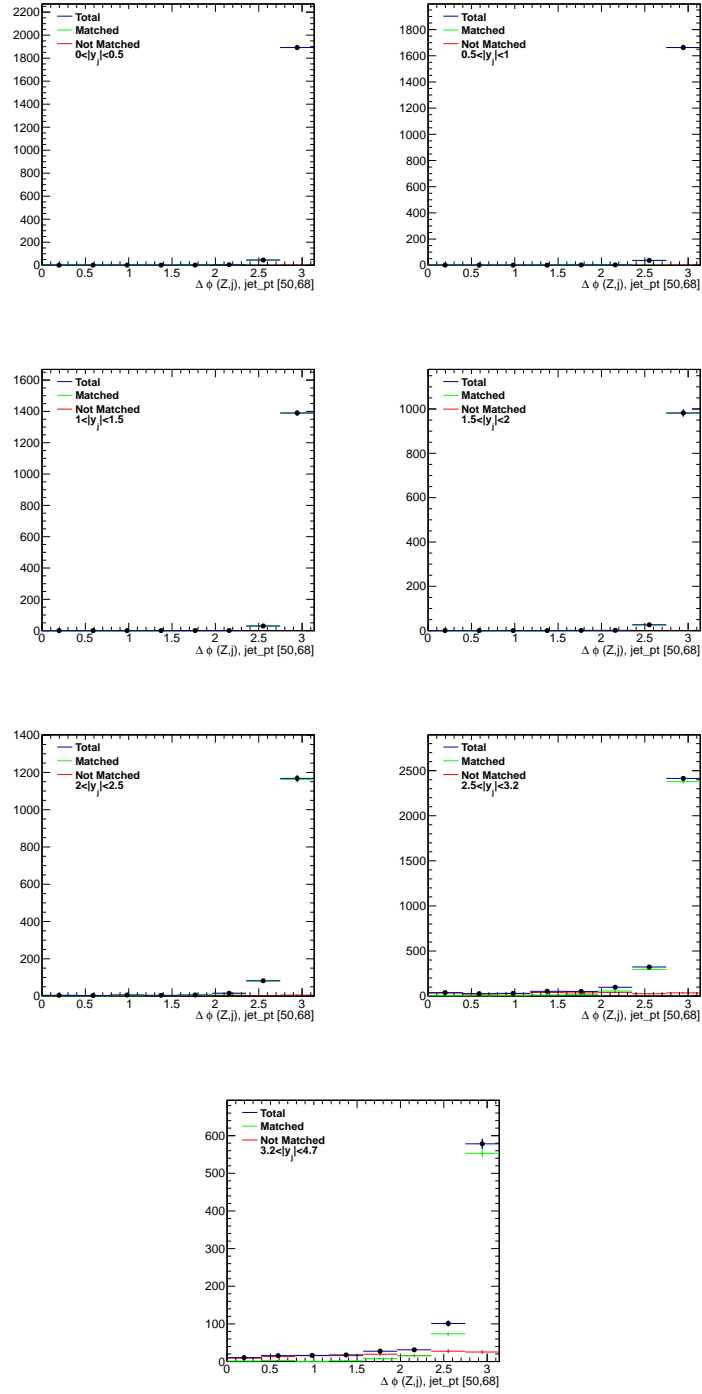


Figure C.4: The azimuthal angle difference distributions between the Z boson and the jet ( $\Delta\phi(Z, j)$ ) for jets with  $p_T[50,68]$  GeV for Z+1j exclusive events. The green (red) lines represent the jets that are matched (not-matched) to a gen jet.





## APPENDIX D

### RESULTS OF Z+JET MEASUREMENTS

In this appendix, the obtained results of Z+jet cross-section measurements are given in the tables for each range, after combination of electron and muon channels, with the breakdown of the systematic uncertainties.

TableD.1: Z rapidity  $\times \text{sign}(y(j_1))$  ( $0 < y(j_1) < 0.5$ )

y(Z) range	$d^2\sigma/dy(Z)dy(j_1)[pb/GeV]$	stat	JES	Lumi	JER	PU	xsec	pu subt	unf	tot
-4.7–3.2	0.0701	2.036	28.6	0.01149	4.547	4.829	0.04205	15.87	2.132	41.27
-3.2–2.5	0.3739	1.125	11.13	0.01397	1.007	3.712	0.08159	4.255	3.03	16.23
-2.5–2	0.7844	0.9859	13	0.03265	0.7152	0.2363	0.1748	0.4412	3.336	16.99
-2–1.5	1.312	0.7025	8.35	0.0394	0.4162	0.4206	0.2037	0.388	0.8789	10.74
-1.5–1	1.973	0.5566	4.734	0.04822	0.1944	0.3108	0.2285	0.3287	1.049	6.606
-1–0.5	2.617	0.4626	4.166	0.05724	0.1888	0.3985	0.2546	0.2631	1.951	6.38
-0.5–0	3.094	0.4346	3.432	0.06126	0.1311	0.3542	0.2699	0.2393	1.719	5.532
0–0.5	3.219	0.4139	3.356	0.06364	0.114	0.374	0.271	0.2402	2.629	6.098
0.5–1	2.917	0.4427	3.832	0.06289	0.1567	0.4604	0.2765	0.253	2.155	6.206
1–1.5	2.322	0.5001	4.108	0.05681	0.2342	0.3253	0.2612	0.3125	2.027	6.386
1.5–2	1.637	0.6261	7.322	0.05292	0.4841	0.3669	0.2438	0.3696	1.132	9.564
2–2.5	0.9937	0.8509	11.75	0.0457	0.7241	0.2821	0.2324	0.4372	1.534	14.93
2.5–3.2	0.4611	1.038	10.32	0.02687	1.042	3	0.1507	4.12	2.541	14.93
3.2–4.7	0.08333	2.04	28.92	0.003129	4.52	4.542	0.01719	16.53	5.009	42.45

TableD.2: Z rapidity  $\times \text{sign}(y(j_1))$  ( $0.5 < y(j_1) < 1$ )

y(Z) range	$d^2\sigma/dy(Z)dy(j_1)[pb/GeV]$	stat	JES	Lumi	JER	PU	xsec	pu subt	unf	tot
-4.7-3.2	0.05996	2.043	26.07	0.01577	3.495	3.939	0.07087	14.27	4.795	37.84
-3.2-2.5	0.2973	1.243	11.8	0.002621	1.081	4.68	0.02173	4.34	0.251	16.78
-2.5-2	0.6094	1.199	14.84	0.02373	0.7901	0.649	0.127	0.4526	4.319	19.6
-2-1.5	1.021	0.8489	9.904	0.03184	0.5966	0.4507	0.1649	0.4031	3.1	13.34
-1.5-1	1.591	0.6404	5.272	0.03688	0.2071	0.249	0.1856	0.3277	0.3697	7.079
-1-0.5	2.247	0.5164	4.482	0.04318	0.18	0.3701	0.208	0.2592	0.8777	6.253
-0.5-0	2.825	0.472	3.695	0.04867	0.1087	0.4895	0.2246	0.2443	1.617	5.743
0-0.5	3.139	0.4402	3.481	0.05766	0.09996	0.4889	0.2553	0.2357	2.291	5.976
0.5-1	3.072	0.4436	3.43	0.05902	0.1763	0.5165	0.2598	0.243	2.812	6.364
1-1.5	2.637	0.4871	3.568	0.05732	0.1728	0.3812	0.2594	0.2925	2.979	6.632
1.5-2	1.974	0.5768	6.111	0.05418	0.3382	0.504	0.2568	0.3359	2.272	8.619
2-2.5	1.247	0.7682	9.972	0.05164	0.6075	0.3625	0.2595	0.3794	0.8972	12.69
2.5-3.2	0.599	0.935	8.976	0.03786	0.9462	2.216	0.2078	3.823	0.6169	12.68
3.2-4.7	0.101	2.068	28.36	0.01687	5.298	3.066	0.1117	16.9	20.19	50.36

TableD.3: Z rapidity  $\times \text{sign}(y(j_1))$  ( $1 < y(j_1) < 1.5$ )

y(Z) range	$d^2\sigma/dy(Z)dy(j_1)[pb/GeV]$	stat	JES	Lumi	JER	PU	xsec	pu subt	unf	tot
-4.7-3.2	0.04844	2.108	23.03	0.01796	2.278	4.935	0.08512	12.58	6.806	34.47
-3.2-2.5	0.2213	1.449	11.72	0.002584	0.7232	4.235	0.009198	4.149	3.106	17.02
-2.5-2	0.4388	1.535	15.46	0.01513	0.8143	0.6406	0.0848	0.4822	6.715	21.67
-2-1.5	0.7353	1.082	11.2	0.02276	0.6058	0.2048	0.1239	0.4107	6.314	16.78
-1.5-1	1.143	0.8567	6.344	0.02672	0.232	0.4741	0.1443	0.3323	1.933	8.841
-1-0.5	1.676	0.6559	5.379	0.03197	0.209	0.6103	0.1655	0.274	0.3396	7.223
-0.5-0	2.215	0.5353	4.136	0.03775	0.1226	0.4363	0.1866	0.2441	1.368	6.065
0-0.5	2.651	0.5222	3.591	0.04512	0.1247	0.6041	0.2146	0.2344	1.845	5.814
0.5-1	2.793	0.4918	3.452	0.04798	0.1193	0.6287	0.2232	0.2391	2.688	6.307
1-1.5	2.59	0.5078	3.512	0.04672	0.1462	0.624	0.218	0.2753	3.103	6.719
1.5-2	2.06	0.6016	5.573	0.05002	0.3287	0.7495	0.2368	0.3087	2.847	8.447
2-2.5	1.406	0.7508	8.532	0.05278	0.4938	0.6552	0.26	0.3501	2.485	11.46
2.5-3.2	0.6988	0.9063	7.788	0.04278	0.9562	1.264	0.2285	3.406	2.111	11.36
3.2-4.7	0.1126	2.043	25.51	0.02951	4.918	1.297	0.1772	15.19	14.75	42.71

TableD.4: Z rapidity  $\times \text{sign}(y(j_1))$  ( $1.5 < y(j_1) < 2$ )

y(Z) range	$d^2\sigma/dy(Z)dy(j_1)[pb/GeV]$	stat	JES	Lumi	JER	PU	xsec	pu subt	unf	tot
-4.7-3.2	0.01804	2.427	23.66	0.01536	2.344	3.627	0.07739	12.1	4.881	34
-3.2-2.5	0.07897	1.552	10.11	0.006497	0.579	4.081	0.03096	3.82	4.03	15.6
-2.5-2	0.1526	1.974	16.11	0.008983	0.5958	1.462	0.04992	0.4663	7.152	22.8
-2-1.5	0.2478	1.46	10.98	0.01734	0.6356	0.4331	0.09572	0.3827	6.596	16.93
-1.5-1	0.3931	1.044	6.447	0.01977	0.1422	0.06233	0.1112	0.3104	3.576	9.975
-1-0.5	0.5837	0.8438	6.005	0.02405	0.1211	0.5096	0.1343	0.2533	2.04	8.492
-0.5-0	0.8258	0.6708	4.532	0.0261	0.1399	0.683	0.1423	0.2361	0.3083	6.27
0-0.5	1.065	0.5916	3.983	0.03008	0.09083	0.5626	0.1588	0.2193	1.303	5.891
0.5-1	1.22	0.6308	3.726	0.0401	0.1345	0.7058	0.1761	0.2223	1.939	6.089
1-1.5	1.207	0.5758	3.21	0.0382	0.1435	0.7149	0.1881	0.2485	2.785	6.251
1.5-2	1.022	0.6024	4.74	0.03621	0.2698	0.8663	0.1812	0.2677	4.032	8.638
2-2.5	0.7598	0.7455	6.717	0.03727	0.4592	0.942	0.1899	0.2996	4.707	11.05
2.5-3.2	0.4262	0.8365	6.455	0.03483	0.8135	0.6745	0.1877	2.946	3.356	10.34
3.2-4.7	0.071	1.803	20.55	0.03006	3.827	0.7053	0.1752	12.6	13.74	35.95

TableD.5: Leading jet  $p_T$  (  $0 < y(j_1) < 0.5$  )

$p_T(j_1)$ range	$d^2\sigma/dp_T(j_1)dy(j_1)[pb/GeV]$	stat	JES	Lumi	JER	PU	xsec	pu subt	unf	tot
30-40	0.6661	0.2665	3.679	0.01281	0.1717	0.4025	0.06639	0	0.9429	5.331
40-50	0.4116	0.3352	3.272	0.02995	0.2387	0.5311	0.1518	0	1.071	5.039
50-68	0.2338	0.3593	3.734	0.05694	0.1768	0.5629	0.2675	0	0.3748	5.34
68-85	0.1197	0.5287	4.046	0.09601	0.1864	0.5876	0.4144	0	0.1607	5.738
85-104	0.06593	0.657	4.498	0.125	0.2929	0.5034	0.545	0	0.8129	6.386
104-126	0.03657	0.7966	4.915	0.1477	0.245	0.3302	0.6387	0	1.064	6.914
126-148	0.02083	1.008	4.314	0.1502	0.2283	0.4591	0.6651	0	0.9169	6.317
148-175	0.01183	1.208	4.062	0.1496	0.1371	0.4704	0.6777	0	0.5467	6.057
175-200	0.006973	1.577	3.957	0.1528	0.05076	0.4055	0.7053	0	1.441	6.494
200-230	0.004104	1.927	4.382	0.1518	0.3249	0.6633	0.7128	0	1.019	7.007
230-270	0.002306	2.315	3.25	0.1575	0.2016	0.2457	0.7417	0	2.723	7.239
270-320	0.001166	3.314	4.956	0.1579	0.2074	0.246	0.7759	0	1.047	8.716
320-550	0.0002486	3.191	3.459	0.2159	0.293	0.4427	1.077	0	1.015	7.329

TableD.6: Leading jet  $p_T$  (  $0.5 < y(j_1) < 1$  )

$p_T(j_1)$ range	$d^2\sigma/dp_T(j_1)dy(j_1)[pb/GeV]$	stat	JES	Lumi	JER	PU	xsec	pu subt	unf	tot
30-40	0.6185	0.2814	4.012	0.01371	0.2527	0.4725	0.06969	0	0.8929	5.693
40-50	0.3817	0.3392	3.25	0.03257	0.249	0.5141	0.1581	0	1.294	5.109
50-68	0.2159	0.3758	3.849	0.05737	0.1955	0.5531	0.2739	0	0.4907	5.483
68-85	0.1109	0.5365	4.283	0.09422	0.3039	0.5124	0.4184	0	0.1395	5.987
85-104	0.06045	0.6922	4.575	0.1249	0.2463	0.4722	0.5243	0	0.1462	6.337
104-126	0.03326	0.8465	4.386	0.1379	0.2582	0.4373	0.6025	0	2.355	7.076
126-148	0.01878	1.097	5.156	0.1469	0.214	0.5643	0.6516	0	1.564	7.497
148-175	0.01074	1.261	4.111	0.144	0.2603	0.2689	0.6575	0	0.8742	6.172
175-200	0.00606	1.676	3.488	0.149	0.3572	0.6285	0.6927	0	0.5165	5.866
200-230	0.00359	2	5.203	0.162	0.09103	0.3394	0.7488	0	1.808	8.069
230-270	0.001977	2.533	3.71	0.1467	0.2249	0.1557	0.7134	0	1.763	7.166
270-320	0.0009966	3.309	3.799	0.1684	0.2021	0.2894	0.8089	0	2.426	8.344
320-500	0.000246	3.637	5.008	0.1911	0.1236	0.5358	0.9887	0	0.9473	8.98

TableD.7: Leading jet  $p_T$  (  $1 < y(j_1) < 1.5$  )

$p_T(j_1)$ range	$d^2\sigma/dp_T(j_1)dy(j_1)[pb/GeV]$	stat	JES	Lumi	JER	PU	xsec	pu subt	unf	tot
30-40	0.5326	0.2866	3.978	0.01427	0.2721	0.3537	0.07474	0	0.8513	5.628
40-50	0.3207	0.3472	3.25	0.0331	0.2806	0.6057	0.1679	0	0.9909	4.991
50-68	0.1776	0.3998	3.458	0.05991	0.2316	0.6221	0.289	0	0.6293	5.127
68-85	0.08919	0.5693	4.119	0.09051	0.444	0.5994	0.4135	0	0.2424	5.845
85-104	0.0483	0.7034	4.321	0.109	0.388	0.5999	0.4888	0	0.9277	6.226
104-126	0.02588	0.9237	3.978	0.1314	0.2995	0.6575	0.5866	0	0.3126	5.872
126-148	0.0145	1.183	4.279	0.1392	0.3983	0.5382	0.6303	0	0.5564	6.34
148-175	0.008074	1.446	5.189	0.1427	0.3195	0.4016	0.656	0	1.783	7.745
175-200	0.004577	1.927	4.413	0.1321	0.2617	0.08023	0.6257	0	2.048	7.528
200-230	0.002593	2.246	3.824	0.1356	0.3515	0.3571	0.6598	0	1.559	6.907
230-270	0.001416	2.906	4.629	0.1718	0.3529	0.3225	0.8082	0	0.8816	7.921
270-450	0.0003243	3.226	4.652	0.2102	0.06251	0.1912	1.012	0	1.069	8.286

TableD.8: Leading jet  $p_T$  ( $1.5 < y(j_1) < 2$ )

$p_T(j_1)$ range	$d^2\sigma/dp_T(j_1)dy(j_1)[pb/GeV]$	stat	JES	Lumi	JER	PU	xsec	pu subt	unf	tot
30-40	0.4145	0.3352	6.074	0.01574	0.4938	0.4141	0.0841	0	0.8962	8.003
40-50	0.2431	0.4082	4.616	0.03594	0.5627	0.6878	0.1828	0	1.33	6.584
50-68	0.1315	0.4762	4.828	0.06036	0.409	0.7234	0.291	0	0.8553	6.669
68-85	0.0643	0.7235	4.544	0.08248	0.4756	0.6832	0.3938	0	1.208	6.597
85-104	0.03415	0.8769	4.777	0.1052	0.4887	0.3762	0.4847	0	1.522	7.008
104-126	0.01782	1.151	4.784	0.1161	0.4396	0.7486	0.5359	0	0.6485	6.874
126-148	0.00989	1.454	3.928	0.1269	0.06255	0.288	0.5914	0	1.536	6.374
148-175	0.005265	1.887	4.468	0.1407	0.8068	0.2955	0.6523	0	1.209	7.134
175-200	0.002907	2.578	4.063	0.146	0.3421	0.3047	0.6773	0	2.533	7.955
200-230	0.001583	3.304	3.874	0.1587	0.4081	1.023	0.7414	0	1.07	7.992
230-400	0.0003584	3.135	5.184	0.1775	0.3126	0.3259	0.8342	0	1.155	8.749

TableD.9: Leading jet  $p_T$  ( $2 < y(j_1) < 2.5$ )

$p_T(j_1)$ range	$d^2\sigma/dp_T(j_1)dy(j_1)[pb/GeV]$	stat	JES	Lumi	JER	PU	xsec	pu subt	unf	tot
30-40	0.3055	0.3909	7.205	0.01651	0.6905	0.2569	0.08877	0	1.037	9.344
40-50	0.17	0.5005	3.7	0.03793	0.7128	0.4248	0.1986	0	1.197	5.599
50-68	0.08799	0.637	3.598	0.06174	0.7324	0.2235	0.3143	0	2.321	6.25
68-85	0.04111	0.8675	4.117	0.0827	0.63	0.2827	0.4047	0	1.516	6.339
85-104	0.02043	1.174	4.318	0.09876	0.4573	0.4127	0.4725	0	1.633	6.685
104-126	0.01063	1.599	4.133	0.1182	0.5089	0.4841	0.5499	0	1.217	6.634
126-148	0.005436	2.026	4.264	0.1173	0.465	0.3527	0.5472	0	2.498	7.684
148-175	0.002763	2.857	3.453	0.1309	0.5243	0.3715	0.6018	0	2.539	7.89
175-200	0.001398	3.875	7.593	0.1592	0.6163	0.7455	0.7337	0	2.857	12.48
200-320	0.0003293	4.06	5.443	0.1797	0.4508	0.7676	0.811	0	3.527	11.08

TableD.10: Leading jet  $p_T$  ( $2.5 < y(j_1) < 3.2$ )

$p_T(j_1)$ range	$d^2\sigma/dp_T(j_1)dy(j_1)[pb/GeV]$	stat	JES	Lumi	JER	PU	xsec	pu subt	unf	tot
30-40	0.1521	0.3514	8.03	0.01713	0.881	1.621	0.0927	3.872	6.296	14.53
40-50	0.08394	0.4616	7.155	0.03492	1.026	1.001	0.1895	1.169	2.279	9.969
50-68	0.04135	0.5868	7.023	0.05692	1.203	0.5192	0.3029	0.8659	1.02	9.332
68-85	0.01812	0.8986	7.608	0.08077	1.085	0.06827	0.4134	1.196	1.748	10.3
85-104	0.008413	1.259	8.415	0.09875	0.9055	0.4415	0.486	0.9041	2.687	11.64
104-126	0.003788	1.714	8.39	0.1198	1.083	0.2966	0.5661	0.6735	2.5	11.66
126-148	0.001688	2.478	10.48	0.1425	1.111	0.4836	0.647	0.5171	1.771	14.07
148-240	0.0003444	3.284	9.747	0.1498	1.638	0.5103	0.6667	0.4186	3.704	14.51

TableD.11: Leading jet  $p_T$  ( $3.2 < y(j_1) < 4.7$ )

$p_T(j_1)$ range	$d^2\sigma/dp_T(j_1)dy(j_1)[pb/GeV]$	stat	JES	Lumi	JER	PU	xsec	pu subt	unf	tot
30-40	0.04319	0.4804	12.47	0.01167	2.991	1.888	0.0642	8.29	12.55	26.03
40-50	0.01935	0.7404	12.44	0.02773	2.82	0.618	0.1486	0.7191	7.131	18.87
50-68	0.007341	1.054	13.37	0.04576	2.449	0.2608	0.2416	4.098	7.796	20.89
68-85	0.002382	1.76	15.18	0.06015	3.375	0.5723	0.3143	3.735	8.373	23.26
85-104	0.0008196	2.861	18.59	0.07119	5.697	0.5662	0.3572	2.719	8.143	27.29
104-180	0.000105	4.753	23.36	0.08344	6.276	1.149	0.3899	2.26	5.632	32.05

TableD.12: Leading jet  $p_T$  ( $0 < y(j_1) < 1.5$ ,  $y(Z) < 1.0$ ,  $y(Z) \times y(j_1) < 0$ )

$p_T$ range	$d^3\sigma/dp_T(j_1)dy(j_1)dy(Z)[pb/GeV]$	stat	JES	Lumi	JER	PU	xsec	pu subt	unf	tot
30-40	0.08043	0.297	4.045	0.01496	0.2661	0.3046	0.07439	0	0.63	5.643
40-50	0.04847	0.3694	3.578	0.03547	0.3098	0.4773	0.1706	0	0.8981	5.284
50-68	0.02688	0.4137	3.95	0.06215	0.1864	0.3954	0.2924	0	0.2023	5.55
68-85	0.01345	0.5936	4.149	0.09782	0.3228	0.4745	0.4386	0	0.5772	5.907
85-104	0.007243	0.7393	4.914	0.1257	0.2989	0.4746	0.5548	0	0.1077	6.724
104-126	0.003899	0.9624	4.598	0.1448	0.2922	0.4003	0.635	0	1.191	6.715
126-148	0.002176	1.236	4.856	0.1645	0.2495	0.3964	0.7284	0	1.87	7.393
148-175	0.001226	1.506	4.2	0.1664	0.08822	0.3243	0.7488	0	0.6423	6.432
175-200	0.0007077	1.941	3.577	0.1659	0.196	0.3372	0.7575	0	1.767	6.647
200-230	0.0004142	2.418	4.561	0.17	0.6735	0.7571	0.7891	0	1.773	7.932
230-270	0.0002295	2.799	3.342	0.1866	0.1226	0.1445	0.8618	0	1.089	6.837
270-320	0.0001171	3.96	3.554	0.2091	0.1075	0.3202	0.9982	0	1.753	8.659
320-500	2.995e-05	4.289	4.932	0.2466	0.06309	0.2162	1.189	0	2.444	10.18

TableD.13: Leading jet  $p_T$  ( $1.5 < y(j_1) < 2.5$ ,  $y(Z) < 1.0$ ,  $y(Z) \times y(j_1) < 0$ )

$p_T$ range	$d^3\sigma/dp_T(j_1)dy(j_1)dy(Z)[pb/GeV]$	stat	JES	Lumi	JER	PU	xsec	pu subt	unf	tot
30-40	0.03758	0.5332	7.812	0.01587	0.8614	0.2346	0.08631	0	2.79	10.76
40-50	0.0206	0.6853	5.495	0.03435	0.8131	0.3684	0.1848	0	1.23	7.611
50-68	0.01023	0.8276	5.001	0.05423	0.606	0.3703	0.2825	0	2.292	7.606
68-85	0.004742	1.202	4.504	0.07292	0.6064	0.6554	0.3649	0	1.348	6.84
85-104	0.002422	1.578	4.627	0.09722	0.6281	0.2149	0.4613	0	1.512	7.222
104-126	0.001263	1.993	5.569	0.09987	0.4259	0.5697	0.4682	0	1.214	8.296
126-148	0.000669	2.693	3.637	0.1126	0.4848	0.3756	0.5342	0	0.5961	7
148-175	0.0003423	3.633	2.493	0.1626	0.4297	0.6571	0.7397	0	1.267	7.651
175-200	0.0001876	4.781	3.803	0.1866	0.9235	0.6999	0.8104	0	3.375	10.77
200-230	0.0001076	6.276	4.771	0.2004	0.9899	0.9098	0.8836	0	4.592	13.97
230-400	2.379e-05	6.301	4.644	0.2882	0.1108	0.2421	1.226	0	2.701	12.46

TableD.14: Leading jet  $p_T$  (  $2.5 < y(j_1) < 4.7$ ,  $y(Z) < 1.0$ ,  $y(Z) \times y(j_1) < 0$ )

$p_T$ range	$d^3\sigma/dp_T(j_1)dy(j_1)dy(Z)[pb/GeV]$	stat	JES	Lumi	JER	PU	xsec	pu subt	unf	tot
30-40	0.006195	0.8158	9.76	0.01464	2.001	2.602	0.07772	4.06	29.75	44.31
40-50	0.003424	1.072	8.389	0.0293	1.607	1.446	0.1561	1.496	14.36	23.21
50-68	0.001614	1.391	7.76	0.04701	1.838	0.5009	0.2482	4.2	8.599	16.82
68-85	0.0006596	2.177	8.54	0.06721	1.303	0.1332	0.339	2.828	6.795	15.46
85-104	0.0003008	2.933	9.089	0.09075	1.961	0.315	0.415	1.581	7.875	17.09
104-126	0.0001406	4.013	9.927	0.1254	1.66	0.5684	0.5229	1.258	1.398	14.66
126-148	5.75e-05	5.868	10.39	0.1637	1.67	0.4836	0.6819	0.947	5.341	18.21
148-240	1.267e-05	6.867	9.13	0.1576	0.7149	0.04689	0.6396	0.5674	3.653	16.86

TableD.15: Leading jet  $p_T$  (  $0 < y(j_1) < 1.5$ ,  $1.0 < y(Z) < 2.5$ ,  $y(Z) \times y(j_1) < 0$ )

$p_T$ range	$d^3\sigma/dp_T(j_1)dy(j_1)dy(Z)[pb/GeV]$	stat	JES	Lumi	JER	PU	xsec	pu subt	unf	tot
30-40	0.0332	0.4237	5.003	0.01297	0.3349	0.4356	0.06977	0	1.056	6.875
40-50	0.01924	0.5296	4.22	0.02682	0.3833	0.7162	0.1443	0	0.267	5.938
50-68	0.0102	0.5972	4.518	0.04175	0.206	0.7162	0.2208	0	0.9147	6.394
68-85	0.005043	0.8655	4.496	0.0571	0.3425	0.5873	0.2917	0	0.3468	6.351
85-104	0.002705	1.062	4.275	0.06897	0.3423	0.6895	0.3429	0	0.9716	6.363
104-126	0.001484	1.405	4.29	0.07998	0.32	0.2864	0.3938	0	3.024	7.692
126-148	0.0008487	1.794	4.414	0.0799	0.307	0.8096	0.4026	0	1.446	7.125
148-175	0.0004719	2.069	3.796	0.09098	0.0782	0.317	0.4525	0	1.667	6.786
175-200	0.0002802	2.714	3.468	0.1051	0.191	0.5786	0.5171	0	1.516	7.068
200-230	0.0001646	3.279	3.779	0.09968	0.2591	0.1987	0.5107	0	1.203	7.736
230-270	9.216e-05	4.316	4.586	0.1178	0.5106	0.6515	0.5784	0	2.363	9.977
270-320	4.64e-05	5.606	4.384	0.09478	0.4159	0.2777	0.5218	0	1.405	11.14
320-500	1.144e-05	5.927	2.816	0.1767	0.4767	0.3055	0.8668	0	0.6719	10.23

TableD.16: Leading jet  $p_T$  (  $1.5 < y(j_1) < 2.5$ ,  $1.0 < y(Z) < 2.5$ ,  $y(Z) \times y(j_1) < 0$ )

$p_T$ range	$d^3\sigma/dp_T(j_1)dy(j_1)dy(Z)[pb/GeV]$	stat	JES	Lumi	JER	PU	xsec	pu subt	unf	tot
30-40	0.01258	0.832	8.536	0.01215	1.051	0.3413	0.06846	0	4.821	13.01
40-50	0.00671	1.117	4.862	0.02472	0.8365	0.2699	0.1375	0	1.65	7.368
50-68	0.003417	1.385	4.422	0.03742	0.612	0.7334	0.199	0	0.8136	6.798
68-85	0.001621	1.921	3.783	0.04127	0.5469	0.3689	0.217	0	2.007	7.027
85-104	0.0008413	2.262	4.683	0.04743	0.2038	0.1742	0.2441	0	0.8488	7.55
104-126	0.0004435	3.277	2.001	0.06454	0.2794	0.5196	0.3197	0	2.071	7.372
126-148	0.0002309	4.451	3.073	0.09255	1.203	1.016	0.4208	0	2.874	9.766
148-175	0.0001302	5.189	5.785	0.1183	0.4899	0.07589	0.5359	0	2.717	12.05
175-200	6.985e-05	6.606	2.59	0.07591	0.2378	0.8918	0.3662	0	4.693	13.33
200-230	3.738e-05	9.099	0.9847	0.06864	0.3548	1.529	0.3525	0	0.4545	14.85
230-400	8.822e-06	9.27	6.881	0.1256	0.4957	1.168	0.5783	0	0.9525	17.44

TableD.17: Leading jet  $p_T$  (  $2.5 < y(j_1) < 4.7, 1.0 < y(Z) < 2.5, y(Z) \times y(j_1) < 0$  )

$p_T$ range	$d^3\sigma/dp_T(j_1)dy(j_1)dy(Z)[pb/GeV]$	stat	JES	Lumi	JER	PU	xsec	pu subt	unf	tot
30-40	0.001999	1.186	9.209	0.009155	1.263	2.83	0.04999	3.52	49.8	71.63
40-50	0.001111	1.68	8.153	0.01583	1.714	1.16	0.08746	2.691	27.05	39.94
50-68	0.0005428	2.031	8.423	0.02072	1.456	0.2518	0.1144	5.235	15.8	25.89
68-85	0.0002368	3.086	8.531	0.03069	0.9958	0.6599	0.1576	3.611	11.59	20.95
85-104	0.0001103	5.144	6.823	0.04761	2.479	0.7656	0.2268	2.075	4.312	14.46
104-126	5.016e-05	5.969	6.232	0.08199	1.222	1.032	0.3569	1.438	3.169	13.93
126-148	2.208e-05	8.85	13.29	0.1231	3.683	1.017	0.4874	1.165	3.43	22.96
148-240	4.807e-06	10.83	10.76	0.02978	1.517	1.541	0.1397	1.14	12.03	28.01

TableD.18: Leading jet  $p_T$  (  $0 < y(j_1) < 1.5, y(Z) < 1.0, y(Z) \times y(j_1) > 0$  )

$p_T$ range	$d^3\sigma/dp_T(j_1)dy(j_1)dy(Z)[pb/GeV]$	stat	JES	Lumi	JER	PU	xsec	pu subt	unf	tot
30-40	0.09305	0.2738	3.622	0.01307	0.1865	0.3923	0.06677	0	0.5718	5.158
40-50	0.05838	0.3296	3.057	0.03251	0.2329	0.3771	0.1596	0	1.003	4.749
50-68	0.03343	0.3664	3.654	0.0651	0.1822	0.5145	0.2971	0	0.6652	5.301
68-85	0.0172	0.5438	4.068	0.114	0.2451	0.4201	0.4791	0	0.3571	5.78
85-104	0.009439	0.6663	4.541	0.1498	0.3163	0.4798	0.6314	0	0.7923	6.44
104-126	0.005148	0.836	4.612	0.1856	0.2637	0.3921	0.7796	0	0.4678	6.512
126-148	0.00291	1.083	4.443	0.1872	0.1787	0.2507	0.8033	0	1.153	6.595
148-175	0.001643	1.286	4.797	0.1738	0.2872	0.3827	0.7715	0	1.051	6.997
175-200	0.0009368	1.679	4.764	0.1748	0.3826	0.3994	0.7979	0	1.327	7.312
200-230	0.0005479	2.004	4.971	0.186	0.2019	0.3368	0.8517	0	1.599	7.773
230-270	0.0002971	2.492	3.83	0.1798	0.2334	0.2453	0.8422	0	0.9456	6.9
270-320	0.0001507	3.398	4.4	0.206	0.1928	0.2601	0.9529	0	2.41	8.888
320-500	3.759e-05	3.53	3.795	0.2261	0.389	0.4906	1.168	0	1.115	7.955

TableD.19: Leading jet  $p_T$  (  $1.5 < y(j_1) < 2.5$ ,  $y(Z) < 1.0$ ,  $y(Z) \times y(j_1) > 0$  )

$p_T$ range	$d^3\sigma/dp_T(j_1)dy(j_1)dy(Z)[pb/GeV]$	stat	JES	Lumi	JER	PU	xsec	pu subt	unf	tot
30-40	0.05748	0.4231	6.669	0.01809	0.5615	0.2314	0.09518	0	0.937	8.694
40-50	0.03264	0.5205	4.56	0.04436	0.5928	0.3957	0.2184	0	1.758	6.719
50-68	0.01704	0.6391	5.056	0.07465	0.5596	0.2656	0.3491	0	1.522	7.171
68-85	0.008005	0.9352	5.07	0.09765	0.5324	0.4761	0.4659	0	1.628	7.371
85-104	0.004034	1.282	4.834	0.1294	0.4977	0.5648	0.5996	0	1.049	7.096
104-126	0.002086	1.651	5.184	0.1489	0.5928	0.2749	0.6876	0	0.9188	7.634
126-148	0.001118	2.12	3.373	0.1606	0.1962	0.2893	0.7415	0	1.144	6.322
148-175	0.0005781	2.694	3.835	0.168	0.7256	0.144	0.7658	0	2.081	7.675
175-200	0.0003197	3.894	6.168	0.1987	0.6677	0.2475	0.9135	0	2.786	11.23
200-230	0.000169	4.971	4.036	0.232	0.2234	1.356	1.053	0	3.226	11.19
230-400	3.649e-05	4.568	6.225	0.2275	0.3059	0.4673	1.04	0	3.233	11.91

TableD.20: Leading jet  $p_T$  (  $2.5 < y(j_1) < 4.7$ ,  $y(Z) < 1.0$ ,  $y(Z) \times y(j_1) > 0$  )

$p_T$ range	$d^3\sigma/dp_T(j_1)dy(j_1)dy(Z)[pb/GeV]$	stat	JES	Lumi	JER	PU	xsec	pu subt	unf	tot
30-40	0.01145	0.6383	8.192	0.01961	1.849	1.778	0.1063	4.642	11.64	20.54
40-50	0.005775	0.8605	8.121	0.04308	1.752	0.8975	0.2313	0.4751	6.501	14.08
50-68	0.002587	1.07	8.429	0.06877	1.706	0.319	0.3644	3.209	5.772	14.25
68-85	0.001042	1.75	9.023	0.09265	1.953	0.1345	0.4769	2.36	5.083	14.33
85-104	0.0004531	2.366	9.81	0.1163	0.9264	0.4407	0.5732	1.404	4.599	14.68
104-126	0.0001916	3.455	10.18	0.15	1.952	0.339	0.708	1.066	5.304	16.5
126-148	8.378e-05	5.063	11.42	0.1737	1.575	0.6534	0.788	0.8845	3.907	17.68
148-240	1.672e-05	6.395	9.461	0.1913	1.737	0.4893	0.8407	0.7752	5.037	17.58

TableD.21: Leading jet  $p_T$  (  $0 < y(j_1) < 1.5$ ,  $1.0 < y(Z) < 2.5$ ,  $y(Z) \times y(j_1) > 0$  )

$p_T$ range	$d^3\sigma/dp_T(j_1)dy(j_1)dy(Z)[pb/GeV]$	stat	JES	Lumi	JER	PU	xsec	pu subt	unf	tot
30-40	0.05261	0.3302	3.626	0.01236	0.1716	0.5347	0.06685	0	0.9191	5.303
40-50	0.03314	0.4062	3.128	0.02753	0.1646	0.7124	0.1439	0	1.047	4.935
50-68	0.01925	0.4404	3.425	0.04949	0.196	0.7401	0.2457	0	0.03854	5.056
68-85	0.01007	0.611	4.407	0.07826	0.3084	0.7714	0.3556	0	0.1552	6.18
85-104	0.005611	0.8201	4.285	0.09699	0.2763	0.5146	0.408	0	0.5068	6.109
104-126	0.003145	0.9297	4.407	0.09826	0.1922	0.6068	0.4511	0	1.873	6.823
126-148	0.001791	1.17	4.564	0.1041	0.4331	0.8061	0.484	0	0.7409	6.67
148-175	0.001024	1.404	4.041	0.1136	0.2786	0.4542	0.5353	0	1.559	6.446
175-200	0.0005907	1.856	3.613	0.11	0.1303	0.3167	0.5313	0	2.151	6.715
200-230	0.0003412	2.233	4.033	0.1062	0.09269	0.2823	0.525	0	0.6263	6.76
230-270	0.0001897	2.872	4.127	0.122	0.4985	0.4283	0.609	0	3.271	8.778
270-320	8.946e-05	3.786	6.535	0.123	0.2177	0.5879	0.6331	0	3.055	11.36
320-500	2.088e-05	4.476	4.09	0.1525	0.2549	0.5247	0.7882	0	1.781	9.492



TableD.22: Leading jet  $p_T$  (  $1.5 < y(j_1) < 2.5, 1.0 < y(Z) < 2.5, y(Z) \times y(j_1) > 0$ )

$p_T$ range	$d^3\sigma/dp_T(j_1)dy(j_1)dy(Z)[pb/GeV]$	stat	JES	Lumi	JER	PU	xsec	pu subt	unf	tot
30-40	0.04155	0.45	5.552	0.01516	0.2695	0.7518	0.08134	0	0.8264	7.41
40-50	0.02556	0.5485	3.933	0.03355	0.5112	0.8879	0.1742	0	1.892	6.234
50-68	0.01449	0.6127	4.308	0.05645	0.4323	0.6839	0.2818	0	1.797	6.54
68-85	0.007336	0.8859	4.783	0.0802	0.4809	0.5222	0.3819	0	1.444	6.96
85-104	0.003938	1.12	4.796	0.09173	0.4366	0.3726	0.425	0	0.8687	6.876
104-126	0.002077	1.457	4.598	0.1053	0.4256	0.74	0.482	0	1.367	7.064
126-148	0.001151	1.874	4.891	0.1018	0.024	0.4725	0.4787	0	0.6829	7.315
148-175	0.0005999	2.387	5.021	0.1041	0.7957	0.2895	0.4951	0	2.147	8.439
175-200	0.000314	3.14	5.149	0.1029	0.379	0.4352	0.5031	0	2.456	9.274
200-230	0.0001648	4.32	4.133	0.102	0.7572	0.8761	0.5096	0	2.577	10.08
230-400	3.198e-05	4.387	6.084	0.1164	0.3755	0.0504	0.588	0	0.5851	10.75

TableD.23: Leading jet  $p_T$  (  $2.5 < y(j_1) < 4.7, 1.0 < y(Z) < 2.5, y(Z) \times y(j_1) > 0$ )

$p_T$ range	$d^3\sigma/dp_T(j_1)dy(j_1)dy(Z)[pb/GeV]$	stat	JES	Lumi	JER	PU	xsec	pu subt	unf	tot
30-40	0.01124	0.5777	6.494	0.01789	1.39	0.4105	0.09935	4.925	3.068	11.34
40-50	0.005583	0.7968	6.241	0.04045	1.255	0.07924	0.2243	0.2962	3.91	9.968
50-68	0.002518	0.9817	7.589	0.06774	1.576	0.05794	0.3628	2.438	3.982	11.82
68-85	0.001019	1.51	9.339	0.09182	1.563	0.4762	0.4727	1.952	3.197	13.21
85-104	0.0004414	2.366	11.12	0.09766	1.305	0.4574	0.5031	1.233	3.525	15.52
104-126	0.0001845	3.304	11.12	0.09722	1.761	0.2516	0.499	0.9721	6.004	17.4
126-148	7.675e-05	4.604	12.19	0.1041	1.22	0.3799	0.5148	0.7123	5.013	18.51
148-240	1.402e-05	6.58	10.23	0.1284	4.029	0.3252	0.6311	0.7679	5.498	19.26



## APPENDIX E

### SHERPA 2.0.0 DATACARD USED TO GENERATE Z + JET EVENTS

The parameters used to generate SHERPA 2.0.0 Z+jet samples are given below:

(run)

% general setting

EVENTS 130000; ERROR=0.1;

RANDOM\_SEED=1170 ;

EVENT\_OUTPUT=HepMC\_GenEvent[evtfifo]

% scales, tags for scale variations

SP\_NLOCT 1; FSF:=1.; RSF:=1.; QSF:=1.;

SCALES METSF\*FSF\*MU\_F2RSF\*MU\_R2QSF\*MU\_Q2;

% tags for process setup

NJET:=4; LJET:=2,3,4; QCUT:=20;

% me generator settings

ME\_SIGNAL\_GENERATOR Comix Amegic LOOPGEN;

EVENT\_GENERATION\_MODE=Weighted;

LOOPGEN:=BlackHat;

```

MASSIVE[15] 1;

MASSIVE_PS 4 5;

% collider setup

BEAM_1 2212; BEAM_ENERGY_1 = 4000.;

BEAM_2 2212; BEAM_ENERGY_2 = 4000.;

(run)

PDF_LIBRARY = LHAPDFSherpa

PDF_SET = CT10.LHgrid

PDF_SET_VERSION = 0

PDF_GRID_PATH = PDFsets

(processes)

Process 93 93 -> 90 90 93NJET;

Order_EW 2; CKKW sqr(QCUT/E_CMS);

NLO_QCD_Mode MC@NLO LJET;

ME_Generator Amegic LJET;

Loop_Generator LOOPGEN LJET;

Enhance_Factor 16 3,4,5,6;

RS_Enhance_Factor 10 3;

RS_Enhance_Factor 20 4;

Integration_Error 0.02 4;

Integration_Error 0.02 5;

Integration_Error 0.05 6;

```

Integration\_Error 0.08 7;

Integration\_Error 0.10 8;

Scales LOOSE\_METSF\*SF\* $\mu_{F2RSF}$ \* $\mu_{R2QSF}$ \* $\mu_{Q2}$  7,8;

End process;

(processes)

(selector)

Mass 11 -11 66 116

Mass 13 -13 66 116

(selector)



# CURRICULUM VITAE

## PERSONAL INFORMATION

**Surname, Name:** Bilin, Buğra

**Nationality:** Cypriot

**Date and Place of Birth:** 28.10.1986, Nicosia

**Marital Status:** Married

**Languages:** Turkish (Native), English (Fluent), German (Advanced),  
Greek (Intermediate), French (Beginner)

**Phone:** 0041 76 6668490

## EDUCATION

Degree	Institution	Year of Graduation
Ph.D.	METU	2017
M.Sc.	METU	2011
B.Sc.	METU	2009
High School	TMK Nicosia	2003

## PROFESSIONAL EXPERIENCE

Year	Place	Enrollment
2010-present	CERN & METU	Researcher as student at CMS

## CONTRIBUTIONS TO THE CMS EXPERIMENT

Calibration of Forward Calorimeter with Z+Jet Events

SMP NLO+PS Generation and Validation Studies

HCAL : L1 simulation update/maintenance

HCAL, HF calibration studies using  $Z \rightarrow ee$  events

TOP PAG DQM/PVT contact person

Central DAQ, shift-leader shifts

Z + jet cross section measurements with 8 TeV data

Underlying Event measurements with  $t\bar{t}$  events at 13 TeV

## PUBLICATIONS

### CMS Publications with major contribution

**CMS Coll.**, "Measurements of the differential production cross sections for a Z boson in association with jets in pp collisions at  $\sqrt{s} = 8$  TeV", JHEP 04 (2017) 022

**CMS Coll.**, "Search for resonances and quantum black holes using dijet mass spectra in proton-proton collisions at  $\sqrt{s}=8$  TeV", Phys. Rev. D 91 (2015) 052009

(Full list of papers: [http://inspirehep.net/search?ln=en&p=find+au+bilin&of=hb&action\\_search=Search](http://inspirehep.net/search?ln=en&p=find+au+bilin&of=hb&action_search=Search))

### International Conference Publications

**B. Bilin for CMS Coll.**, "Top quark event modelling and generators in the CMS experiment at the LHC", at the 24th International Workshop on Deep-Inelastic Scattering and Related Subjects-DIS 2016, 11-15 April 2016, Hamburg, Germany

**B. Bilin for CMS Coll.**, "Differential Z + jet cross section measurements at 8 TeV", at the 37th International Conference on High Energy Physics-ICHEP 2014, 2-9 July 2014, Valencia, Spain

**B. Bilin for CMS Coll.**, "V+jets production at the CMS", at the International Conference on New Frontiers in Physics- ICNFP 2013, 28 August - 5 September 2013,



### **CMS Public Notes with major contribution**

**CMS Coll.**, "Underlying event measurement with  $t\bar{t} + X$  events with p-p collision data at  $\sqrt{s} = 13$  TeV", CMS-PAS-TOP-15-017

**CMS Coll.**, "First look at top-quark selections with 13 TeV data", CMS-DP-2015-019

**CMS Coll.**, "Measurement of the double differential cross section of Z bosons produced in association with jets in pp collisions at  $\sqrt{s} = 8$  TeV", CMS-PAS-SMP-14-009

**CMS Coll.**, "Measurement of the differential production cross section of Z bosons in association with jets in pp collisions at  $\sqrt{s} = 8$  TeV", CMS-PAS-SMP-13-007

### **CMS Internal Notes**

**CMS AN-2016/055**, "Search for a Heavy Higgs in  $H \rightarrow t\bar{t}$  channel at 13 TeV using CMS data", with 3 others

**CMS AN-2015/335**, "Additional studies for comparisons of Theory Predictions for the  $t\bar{t}$  Process with Data from pp Collisions at  $\sqrt{s} = 8$  TeV", with 10 others

**CMS AN-2015/247**, "Differential cross section of the production of a W boson in association with jets at  $\sqrt{s} = 13$  TeV", with 13 others

**CMS AN-2015/231**, "Underlying Event measurement with  $t\bar{t}$  events in mu + jets channel with p-p collision data at  $\sqrt{s} = 13$  TeV", with 2 others

**CMS AN-2015/219**, "Differential cross section measurements for the production of a Z boson in association with jets in proton-proton collisions at  $\sqrt{s} = 13$  TeV", with 13 others

**CMS AN-2015/149**, "Comparisons of Theory Predictions for the  $t\bar{t}$  Process with Data from pp Collisions at  $\sqrt{s} = 8$  TeV", with 10 others

**CMS AN-2014/193**, "Search for a heavy charged MSSM Higgs production with  $gb \rightarrow tH^\pm \rightarrow (h W^\pm)(bW^\mp)$  at  $\sqrt{s} = 8$  TeV", with 4 others

**CMS AN-2014/115**, "Study of double ( $d^2\sigma/dPT^j dY^j$ ) and triple

$(d^3\sigma/dPT^j dY^j dY^Z)$  differential cross sections of Z + jets in pp collisions at  $\sqrt{s} = 8$  TeV", with 5 others

**CMS AN-2013/224**, "Study of differential cross section of jets associated to Z boson in pp collisions at  $\sqrt{s} = 8$  TeV", with 5 others

**CMS AN-2012/455**, "Search for Narrow Resonances using the Dijet Mass Spectrum in pp Collisions at  $\sqrt{s}=8$  TeV with full 2012 dataset", with 14 others

**CMS AN-2012/146**, "Searches for Microscopic Black Holes Production in pp Collisions at  $\sqrt{s} = 8$  TeV with the CMS Detector", with 7 others

**CMS AN-2011/356**, "Measurement of the Forward-Backward Asymmetry of  $l^+l^-$  Pairs in CMS at  $\sqrt{s}=7$  TeV", with 17 others

**CMS DN-2011/009**, "Forward Jet Energy Correction with Z + jet Events", with 4 others

**CMS AN-2011/256**, "Searches for Microscopic Black Holes Production in pp Collisions at  $\sqrt{s} = 7$  TeV with the CMS Detector", with 6 others

## INTERNATIONAL CONFERENCE PRESENTATIONS

**B. Bilin for the CMS Coll.**, "W,Z + jets", plenary talk given at the Workshop on Jet Vetoes and Multiplicity Observables - JetVM 2016, 14-16 September 2016, IPPP Durham, Durham (United Kingdom)

**B. Bilin for the CMS Coll.**, "Top quark event modelling and generators in CMS", parallel talk given at the Workshop on Deep-Inelastic Scattering and Related Subjects - DIS 2016, 11-15 April 2016, DESY, Hamburg (Germany)

**B. Bilin for the CMS Coll.**, "Underlying event measurement with  $t\bar{t} + X$  events with p-p collision data at  $\sqrt{s} = 13$  TeV with the CMS experiment", poster presented at the Students' Poster Session at the 2016 March LHCC meeting - Posters@LHCC 2016, 28 March 2016, CERN, Geneva (Switzerland)

**B. Bilin for the CMS Coll.**, "Measurement of the Differential Z + jet Production Cross Section in pp Collisions at  $\sqrt{s} = 8$  TeV with the CMS Experiment", poster presented at the Students' Poster Session at the 2015 March LHCC meeting - Posters@LHCC 2015, 4 March 2015, CERN, Geneva (Switzerland)

**B. Bilin for the CMS Coll.**, "Differential Z + jet cross section measurements at 8

TeV", poster presented at the 37th International Conference on High Energy Physics - ICHEP 2014, 2-9 July 2014, Valencia (Spain)

**B. Bilin for the CMS Coll.**, "V + jets production at the CMS", parallel talk given at 2nd International Conference on New Frontiers in Physics - ICNFP2013, 27 August - 7 September 2013, Orthodox Academy of Creta, Kolymbari (Greece)

**B. Bilin for the CMS Coll.**, "Electroweak Physics at the CMS", student talk given at the Recent Developments in High Energy Physics Workshop - HEP-WS-2013@METU NCC, 28 May- 1 June 2013, METU NCC, Morphou (Cyprus)

**I. V. Akin, B. Bilin, H. Gamsizkan, M. O. Sahin, S. Sekmen, M. Serin, U. E. Surat, E. Yazgan, M. T. Zeyrek**, "Selected Contributions to the CMS Experiment at the LHC from Past and Present Members of the METU High Energy Physics Group" poster presented at CERN: Accelerating Science Exhibition, 2 April - 8 July 2012, METU, Ankara (Turkey)

## **SCHOOLS ATTENDED**

**The CERN European School of High- Energy Physics**, Anjou, France, June 2012

**The Winter School of High Energy Physics**, Uludağ University, Bursa, TURKEY, February 2012

**The School of Trigger and Data Aquisition**, TAEK, Ankara, TURKEY, February 2010

**The School of Computer Applications on Accelerator and Particle Physics**, Çukurova University, Adana, TURKEY, January 2009

## **COMPUTER LITERACY**

C, C++ programming languages

Linux, shell scripting, python

Comphep, Madgraph, Pythia, Sherpa event generators

ROOT analysis framework, CMS Software (CMSSW)

Internet Tools, L<sup>A</sup>T<sub>E</sub>X, MS Office Programs (Excel, Word, Powerpoint, etc.)

## **OUTREACH ACTIVITIES**

Official CERN guideship for visits to CMS experiment in Turkish, English, and German languages

## **AWARDS**

Dean's High Honor List, February 2004, June 2009, METU, Ankara, TURKEY